Multi-spectral lifetime imaging: methods and applications

Multi-spectrale levensduur beeldvorming: methoden en toepassingen

(met een samenvatting in het Nederlands)

Proefschrift

ter verkrijging van de graad van doctor aan de Universiteit Utrecht op gezag van de rector magnificus, prof.dr. G.J. van der Zwaan, ingevolge het besluit van het college voor promoties in het openbaar te verdedigen op woensdag 20 maart 2013 des ochtends te 10.30 uur

Door

Farzad Fereidouni

geboren op 27 augustus 1979 te Urmia, Iran

Promotor: Prof.dr. H.C. Gerritsen

Co-promotor: Dr. G.A. Blab

Table of Contents

Chapter 1: Introduction 7

Lifetime and Spectral microscopy 8

Lifetime analysis & measurement methods 9

Spectral unmixing techniques 13

Spectrally resolved lifetime imaging 14

Outline of this thesis 16

References 18

Chapter 2: A modified phasor approach for analyzing time-gated fluorescence lifetime images 21

Abstract 22

Introduction 23

Measuring lifetime 24

Theory 25

Methods and materials 31

Simulations 31

Imaging experiments 32

Sample preparation 33

Spectral un-mixing 33

Results and discussions 33

Numerical Simulation 33

Experiments 35

Conclusion 38

references 40

Chapter 3: Spectral phasor analysis allows rapid and reliable unmixing of fluorescence microscopy spectral images 43

Abstract 44

Introduction 45

Methods and materials 46

Instrument details 46

Spectral phasor analysis 46

Sample details 49

Results 49
Spectral phasor analysis of dye solutions 49
Spectral phasor based unmixing of labeled cells 51
Unmixing of autofluorescence in grass blade 52
Compatibility of spectral phasor analysis with other (hyper-) spectral imaging systems 54
Discussion 56
References 59
Chapter 4: Phasor analysis of multiphoton spectral images distinguishes autofluorescence components of in vivo human skin 61
Abstract 62
Introduction 63
Methods 64
Spectral phasor analysis 64
Instrumentation 65
Imaging conditions and processing 66
Results 66
Discussion 73
References 74
Chapter 5 : High Speed Multispectral Fluorescence Lifetime Imaging 77
Abstract 78
Introduction 79
Materials and Methods 80
Instrument details 80
Data analysis 82
Sample details 85
RESULTS 85
Error analysis 85
Lifetime accuracy and count rate 88
Analysis of recoded image of cells 89
Discussion and conclusions 92
References 94

Chapter 6: Blind unmixing of spectrally resolved lifetime images 97
Abstract 98
Introduction 99
Temporal and spectral phasor analyses 100
Materials and Methods 103
Theory 103
Instrumental details 108
Sample details 109
RESULTS 109
Unmixing of two components 109
Unmixing of two components in labeled cells 114
Unmixing of three components in labeled cells 115
Conclusion and discussion 116
References 119
Chapter 7: Quantitative FRET estimation by spectrally resolved lifetime imaging 121
Introduction 122
Materials and Methods 123
Theory 123
Bi-exponential behaviour 127
Instrumental details 129
Sample details 129
RESULTS 129
Fret efficiency estimation 129
Conclusion and Discussion 132
References 135
Summary 137
Samenvatting 140
Acknowledgment 143
CV 145

1

Introduction

LIFETIME AND SPECTRAL MICROSCOPY

Upon excitation of a molecule to the excited state S_1 a chain of photo physical processes takes place such as internal conversion or vibrational and rotational relaxation, fluorescence, intersystem crossing and phosphorescence [1]. Fig. 1 shows a schematic view of processes that may take place after excitation. Fluorescence and phosphorescence result in emission of a photon but in other deactivation processes the excited molecule loses its energy without light emission. Fluorescence is the relaxation of an excited molecule to its ground state, S_0, by releasing a photon. The photon energy is inversely proportional to its wavelength λ and there is always a Stokes shift in wavelength; the emitted light wavelength is longer than wavelength of the excitation light. The relaxation from S_1 can occur to any vibrational states of S_0 which generates a range of Stokes shifts and a relatively broad emission spectrum. Details of the spectrum can be used to identify the fluorophores. The excited fluorophore stays in the S_1 state for a certain characteristic time, ranging from picoseconds to hundreds of nanoseconds, and then relaxes to the ground state. This fluorescence lifetime is characteristic for a fluorescent molecule and can help to identify the fluorophore. Both the emission spectrum and the fluorescence lifetime may be affected by the local environment. In fluorescence microscopy the fluorescence signal can be used to, for instance, study morphology and localization of molecules such as proteins inside the cell. This is a non-invasive and sensitive method that is used routinely in many laboratories. The spectroscopic properties like the emission spectrum and fluorescence lifetime can be also used in imaging. These properties may provide information about the molecular environment and interactions between molecules on the nanometer ranges.

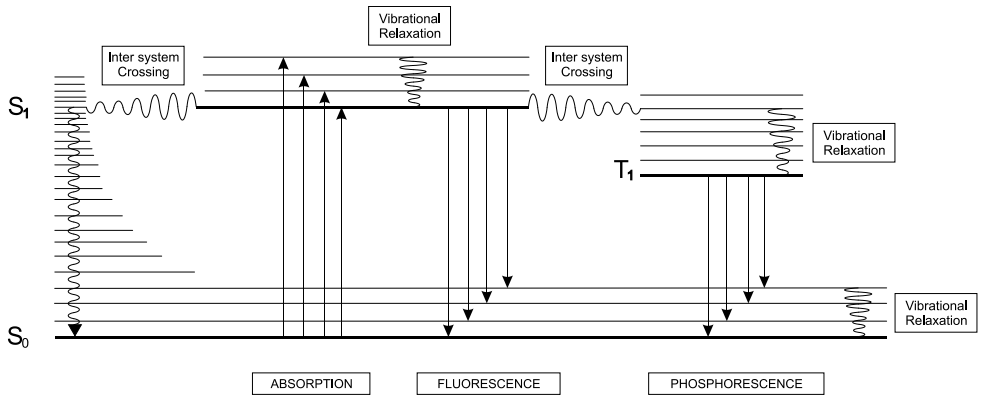

Fig. 1 Jablonski diagram and illustration of the deactivation phenomenon.S_1 and S_0 are the ground and the excited singlet state respectively. T_1 is the triplet states where phosphorescence can occur from.

In microscopy, imaging of the fluorescence is possible in both wide field [2,3] and scanning mode [4-6]. Besides intensity mapping, spatial mapping of spectra and lifetime is employed to provide contrast between different fluorescent molecules or different states that may be affected by environmental properties and molecular interactions. Lifetime and spectral

imaging are complementary techniques that offer a noninvasive solution for e.g. monitoring of metabolic processes, identification of biochemical compounds and their interactions in biological tissues. The decay kinetics and the emission spectrum of the excited chromospheres can be spatially mapped using a standard microscope equipped with time correlated single photon counting (TCSPC), time gated detection [4] or high-frequency modulated detectors for lifetime imaging and spectrographs for spectral imaging.

Emission spectra of the excited molecules are used to study the colocaliztion of different molecules via unmixing algorithms [7,8], to assess pH [9], Intermolecular energy transfer [10] and metabolic studies via monitoring free and bound NADH [3,11].

Lifetime imaging adds another dimension to fluorescence imaging and it can be employed to assess environmental parameters like pH [12], viscosity[13], and oxygen saturation[14], distinguish bound and unbound NADH [15] or, similar to spectral imaging, to identify and quantify the autofluorescent components in tissues [16,17]. Importantly, lifetime imaging can be used to study the interaction between two molecules labeled with two matched fluorophores via Förster Resonance Energy Transfer (FRET) [18]. This has become a major tool to study and image molecular interactions in optical microscopy.

Most of these measurements can be performed in both time and spectral domain and sometimes the contrast in one of the methods is higher. In general collecting more information by using both dimensions is favorable in terms of sensitivity; this is important because often signal levels are low in fluorescence microscopy. Moreover, in biological applications long acquisition times may be problematic. This motivated the development of new instruments that perform time resolved spectral imaging. Although first spectral lifetime detection systems have been developed long time ago [19] their full potential has by far not been realized. Spectrally resolved fluorescence lifetime imaging systems have been developed using both time domain and frequency domain approaches. See for instance the review paper by Hanley et al.[20]. Such systems provide two dimensional data for each pixel in the image and analyzing such data sets to e.g. obtain more reliable information is a major challenge. Fast and reliable methods are urgently needed to complement the hardware development and release the full potential of spectrally resolved fluorescence lifetime imaging.

LIFETIME ANALYSIS & MEASUREMENT METHODS

Compared to spectral imaging, lifetime imaging requires more complicated setups that include fast electronics and the analysis is more complex as well. Two major methods are used to measure the lifetime of an excited state of a molecule. In frequency domain systems the fluorescent molecules are excited by modulated light. The fluorescence signal

is modulated at the same frequency but phase shifted (phase shift ϕ) and demodulated (modulation depth *M*) with respect to the excitation light. The lifetime can be estimated both from the change in the modulation depth and from the phase shift, resulting in the modulation lifetime τ_M and phase lifetime τ_ϕ respectively. A difference between these quantities is indicative of a multi exponential fluorescence decay that may be the result of heterogeneities in the sample, the presence of two different fluorescence molecules with different lifetimes or the presence of molecules with multiple decay components. Resolving of more than one lifetime can be accomplished by recording images at multiple modulation frequencies.

In the time domain, the fluorescence decay curves can be recorded directly by employing pulsed excitation in combination with time gated or time correlated detection systems. In both cases the recorded decay curves are convoluted with the instrument response. This is the measured pulse shape of the excitation laser and includes the shape of the excitation pulse and the response of the electronics. The measured fluorescence intensity d_0 in the i^{th} time channel with time t_i, is given by:

$$d_0(t_i) = \sum_{q=1}^{Q} \frac{\alpha_q}{\tau_q} \int_0^{t_i} IRF(t') e^{-(t_i - t')/\tau_q} dt' \qquad (1)$$

Where τ_q is the lifetime of the q^{th} species, and α_q is the fractional contribution and the summation runs from 1 to *Q* , the total number of species. The integral is the convolution integral and *IRF* is the instrument response function. The goal of the analyses algorithm is to extract the pure decay curve from the measured decay and to estimate the lifetime(s). The latter is usually accomplished by fitting single or multi exponential functions. A variety of methods have been developed to solve this problem. A good comparison of different methods is presented in [21]. Briefly, the most widely used technique is the least square iterative re-convolution which is based on the minimization of the weighted sum of the residuals. In this technique theoretical exponential decay curves are convoluted with the instrument response function, which is measured separately, and the best fit is found by iterative calculation of the residuals for different inputs until a minimum is found. For a set of observations $d(t_i)$ of the fluorescence signal in time bin *i*, the lifetime estimation is carried out by minimization of:

$$\chi^2 = \sum_i \left[d_i(t_i) - d_{0i}(t_i, a, \tau) \right]^2 \qquad (2)$$

Besides experimental difficulties, including the wavelength dependent instrument response function, mathematical treatment of the iterative de-convolution problem is not straight forward and it is a slow process which makes it impractical for a pixel by pixel

analysis. This becomes even more important when lifetime and spectral imaging are combined which results in much larger data sets.

Non fitting methods are attractive because they offer a very fast solution to lifetime estimation. One of the major and straightforward techniques in this category is the rapid lifetime determination (RLD) method [22]. RLD calculates the lifetimes and their amplitudes directly by dividing the decay curve into two parts of equal width Δt. The analysis is performed by integrating the decay curve in equal time intervals δt:

$$D_0 = \sum_{i=1}^{K/2} I_i \delta t \quad D_1 = \sum_{i=K/2}^{K} I_i \delta t \tag{3}$$

I_i is the recorded signal in the i-th channel and K is the number of channels. The lifetime can be estimated using:

$$\tau = \Delta t / \ln(D_0 / D_1) \tag{4}$$

For multi exponential decays this equation provides the average lifetime. This method can be extended to analyze bi-exponential decays [22]. One major drawback of this method is that it cannot take into account the instrument response effect and for this reason the early part of the measured decay curves should be ignored in the analyses. This means that part of the signal is discarded and the accuracy for estimating short lifetimes goes down.

One of the interesting features of the convolution theorem is that the integral of the convolution is the product of the factors that make up the integral. There are a few techniques which work in transformed space that exploit this property to recover the pure decay curve from the measured curve. Laplace [23] and Fourier transformation [24] along with Laguerre gauss expansion [25] have been used to estimate the lifetime in transformed space. These approaches are faster than the deconvolution based methods but they suffer from truncation and sampling problems. Moreover, application of methods like Laguerre gauss expansion is mathematically complicated. In Fourier methods the lifetime τ of a single exponential decay curve is given by:

$$\tau = \frac{1}{n\omega} \frac{A_n}{B_n} \tag{5}$$

Where:

$$A_n = \frac{\sum_t d(t)\sin(n\omega t)}{\sum_t IRF(t)\sin(n\omega t)} = \frac{\omega\tau}{1+\omega^2\tau^2}, \quad B_n = \frac{\sum_t d(t)\cos(n\omega t)}{\sum_t IRF(t)\cos(n\omega t)} = \frac{1}{1+n\omega^2\tau^2} \quad (6)$$

$$\omega = \frac{2\pi}{T}$$

and *n* is the harmonic number and *T* is the total time range of detection. Bi-exponential and higher exponential decays can be analyzed by including higher harmonics in the analyses using the Weber method. This technique offers an analytical solution for estimation of lifetimes of double exponential decays [26]:

$$\begin{aligned} M_0 &= h_1^2 B_1 - h_2^2 B_2 \qquad M_1 = h_1 A_1 - h_2 A_2 \\ M_2 &= -B_1 + B_2 \qquad M_3 = A_1 / h_1 + A_2 / h_2 \end{aligned} \quad (7)$$

$$\theta_1 = (M_3 M_0 - M_2 M_1)/(M_2 M_0 - M_1) \quad (8)$$

$$\theta_2 = (M_3 M_1 - M_2)/(M_2 M_0 - M_1)$$

$$\tau_{1,2} = \left[\theta_1/2 \pm \left(\theta_1^2/4 - \theta_2\right)^{1/2}\right]/\omega \quad (9)$$

with *h* the harmonic number and *A* and *B* as defined by Eq. 1.6. In this description the decay is recorded with an infinite number of time bins and unlimited time period. One of the important issues in real life analyses is to consider the cut off and finite sampling which limits the usefulness of the transformation based methods. This has been considered in [14] where the Laplace transformation is adapted to truncated decay curves. This problem will be considered in more detail in chapter 2.

The phasor approach is a powerful Fourier transformation based method to analyze fluorescence lifetime images [27]. Here, the measured decay is Fourier transformed and the imaginary and real parts of the transformation are used as coordinates in a 2D plot. The effect of the instrument response function can be accounted for either by calibration using the phasor of a known sample or by measuring the instrument response separately. The results of Eq. 1.6 can be mapped in an *AB* or phasor plot which is shown if Fig. 2 for different lifetimes recorded at f=80MHz frequency.

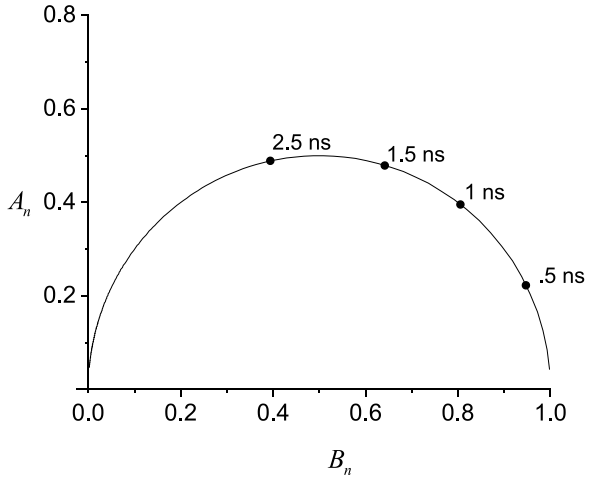

Fig. 2 phasor plot showing phasors corresponding to lifetimes of 0.5, 1, 1.5 and 2ns measured at 80 MHz.

The average lifetimes can be estimated easily using Eq. 1.6. This is a more efficient method than the RLD method because the whole decay curve is considered and there is no loss of photons.

One of the major characteristics of the phasor approach is the reciprocity with the original data set; every pixel in the lifetime image is correlated with a pixel in the phasor plot. By selecting a region of interest in the phasor plot and remapping it onto the original image, a basic segmentation can be achieved. This property has been used, for instance, to discriminate different species in metabolic activities [28]. More details about this techniques and the error analysis is presented in chapter 2.

SPECTRAL UNMIXING TECHNIQUES

Spectral imaging can be achieved by adding a spectrograph equipped with a grating or prism to the microscope or simply by employing a set of band-pass filters. This method has been implemented in wide-field and confocal microscopes and one of the basic and more important applications of spectral imaging is to unmix fluorescent components. In spectral unmixing the total spectrum is decomposed into the constituent spectra and their fractions. It may be used, for instance, to study the distribution of proteins in cells Unmixing allows quantification of the fractional intensities from each component and may also provide spectroscopic information.

Numerous unmixing algorithms have been developed to address different problems. The unmixing methods need a model to describe how different components are superimposed at the pixel level and contribute to the total spectrum. In most cases linear superposition is considered of fluorophores that are not subject to (interaction) effects such as solvatochromic shifts. The intensity *y* of a pixel with index *j* in wavelength channel n is related to the “concentration” x of fluorophore number k by:

$$y_{nj} = \sum_k a_{nk} x_{kj} \quad (10)$$

The spectral measurement provides *y* and the challenge of unmixing is to extract the concentration *x* and spectra *a*. The linear unmixing [29] technique is a standard and straightforward technique which relies on separate reference measurements. In many applications the measurement of reference spectra is not trivial especially when we are dealing with samples which contain endogenous (autofluorescent) fluorophores. Numerous methods have been developed to overcome this problem and avoid the use of reference measurements by extracting the required information from the image itself. This usually requires the use of constraints to perform the unmixing. Non-negative Matrix Factorization (NMF) [8] is a global analysis method which employs a minimum number of constrains; it assumes spectra and fractional intensities to be positive quantities. In addition, this method needs a rough estimation of the spectra of the pure components. In practice, the final unmixing result is affected by the initial estimation of the spectra. The unmixing of up to 4 components is reported, but since it relies on minimization of a cost function it is not a fast algorithm. Parallel factor analysis PARAFAC [30] is a method which employs excitation and emission spectrum to blindly unmix the principal components. The use of multiple excitation wavelengths can be problematic; comparatively long acquisition times are required and photo bleaching may be a bottle neck. Principal Component Analyses (PCA) [31] is another technique which is employed by setting up a perpendicular coordinates called principal components and maximization of the variances of data points along each of a perpendicular coordinates. The method is mathematically complicated and it has been used for instance for decomposition of Flavin autofluorescence components [32] .

SPECTRALLY RESOLVED LIFETIME IMAGING

Spectrally resolved lifetime imaging systems have been developed that employ frequency [33] and time domain [34] based lifetime detection. The time domain approaches are generally based on TCSPC. In this method it is assumed that the detection of multiple photons in different spectral channels at every excitation is unlikely and basically only one photon can be detected from each spectral channel. Bird *et al.* [34] used a multi-anode PMT with 16 channels and a concave diffraction grating for dispersing and focusing of the emission signal on the PMT channels. In this confocal scanning microscope, a time resolution of 295 ps and spectral resolution of 10 nm with a spectral detection window from 380 – 680 nm is achieved. A line scanning system is reported to decrease the acquisition time [35] for hyper spectral lifetime imaging. By using a gated intensifier which is triggered by the excitation pulse, series of time gated images are recorded at different delays after excitation and a time resolution of 100 ps are achieved. The spectrum is recorded by dispersing the fluorescence signal on an electron multiplying CCD (EMCCD) camera resulting in 32 spectral channels with 27nm spectral channel width. Simple setups were also used to perform multi-spectral lifetime imaging. Knemeyer et al. [36] used a

dichroic beam splitter to divide the emission light on two avalanche photo diodes and they used fractional intensities to determine the maximum emission wavelength. The same approach was used in [37] to determine the emission maximum in a setup with two beam splitters used to guide the light into three fibers with different lengths. This was to make sure that the decays of different spectral channels are recorded in a successive way without overlap. A single PMT is used as a detector to collect the entire signal.

The application of these systems results in an improved accuracy with which quantities are estimated. In addition, more information can be extracted from the images. In frequency domain lifetime imaging systems images, two different modulation frequencies need to be used to extract the lifetimes of a two component mixture; this complicates the image acquisition and results in longer acquisition times. Hanley et al.[38] used frequency domain spectral lifetime imaging and employed a phasor approach to unmix two components and their lifetimes using only a single modulation frequency for the excitation light. The spectral information removes the need for the extra recording at other harmonics. In a more recent publication [39] it is shown that the unmixing process becomes more accurate when spectral and lifetime information is combined. It is possible to unmix the signals from Rhodamine and fluorescein even when the fractional intensity of the Rhodamine is below 2%. It is also shown that the estimation of FRET efficiencies becomes more accurate. In some cases the presence of extra donor molecules which don't interact with acceptor molecules affect the FRET efficiency estimation. By employing the full information from lifetime and spectra the real FRET efficiency can be found. The quantitative analysis of FRET is challenging. The possibility of monitoring the donor and acceptor simultaneously enhances the estimation sensitivity. More information is acquired by recording the whole spectrum and collecting more photons. A spectrally resolved frequency domain lifetime imaging system is used to study FRET [40] in a multi-fluorophore system. Here, it turned out to be possible to discriminate between situations where all or some of the fluorophores are interacting. In another application the employment of a spectrally resolved lifetime imaging system is used to estimate the FRET efficiencies in a system where there are interacting and non-interacting donor molecules [41]. By tuning the laser wavelength and avoiding direct acceptor excitation an analytical solution for the decay kinetic of the donor molecule is found. Assuming a bi-exponential decay behavior for the donor it was proved that the FRET estimation accuracy goes up when the information from all spectral channels is used.

Although the power of spectrally resolved lifetime imaging systems has been convincingly demonstrated, the development of optimized analysis tools is still in its infancy. It is limited to lifetime estimation in individual spectral channels or at best a global fitting procedure to extract the FRET efficiency. Spectrally resolved lifetime imaging is much more than a method to simultaneously measure lifetimes and spectra. This method provides two dimensional data sets for each pixel and the capability of measuring lifetimes at different

spectral channels and spectra at different time channels. Inclusion of the whole data set in the analyses can provide new and more detailed information and improve sensitivity.

OUTLINE OF THIS THESIS

The aim of this PhD project is to further develop multispectral life time imaging hardware and analyses methods. The hardware system, Lambda-Tau, generates a considerable amount of data at high speed. To fully exploit the power of this new hardware, fast and reliable data analyses methods are required. Here, a phasor approach is used in all analyses; this provides a fast, visual solution for analyzing the recorded data. After successful demonstration of the phasor approach for time gated lifetime images, and showing that the time gated phasor analyses is compatible with a broad range of gate configurations, we used a similar approach to create the spectral phasor method which found immediate application in our group.

Chapter 2 describes the theoretical framework of a generalized phasor approach for the analyses of time resolved data. It takes into account finite sampling and truncation of decay curves. An analytical expression for the phasor reference semicircle is presented which is compatible with different gate configurations and widths of the measurement windows. A global solution is provided to extract two lifetimes and fractional intensities in a binary mixture. This method is applied to analyze images recorded with a time gated detection system with 4 time gates (LIMO). An error analysis is performed to evaluate the required number of photons in a global analysis for estimation of two lifetimes in the image. The generalized phasor approach is exemplified in a FRET experiment.

Chapter 3 describes a novel technique for spectral unmixing based on a phasor approach. The spectral phasor approach is a fast, reliable and simple method to represent the hyper spectral images in a 2D plot and provides a solution for semi-blind unmixing. We show that for a 3 component system all different mixtures fall inside a triangle with vertices made up by the spectral phasors of the pure components. In this chapter we successfully demonstrate the unmixing of images of fluorescently labeled cells and of autofluorescent grass blades. We show compatibility of the spectral phasor method with different spectral imaging systems; the spectral phasor approach can be employed even in systems with low numbers of spectral channels.

In chapter 4 spectral phasor analysis is used to analyze two photon excited autofluorescence and second harmonic generation images of in vivo human skin. Different structures, including Stratum Corneum, epidermal cells, melanized cells and dermis, can be discerned by applying spectral phasor analyses.

In chapter 5 the hardware development of the Lambda-Tau system is described. The hardware is based on a Field-Programmable Gate Array (FPGA), is capable of operating at high photon count rates and provides good time resolution. This chapter also contains an error analysis to investigate the performance of time domain lifetime imaging and spectral

detection using different time gate and spectral channel configurations. Good performance of the electronics was demonstrated at count rates as high as 12 MHz per spectral detection channel.

Chapter 6 is focused on the application of spectrally resolved lifetime imaging for blind unmixing. Time domain and spectral phasors are used for unmixing of the fluorescent components. Fractional intensities, spectra and decay curves of components are extracted without any prior knowledge.

Chapter 7 provides a prospect to analyze the FRET samples using the information from all spectral channels. A model is provided based on phasor approach to simplify the behavior of ingrowth in acceptor channel. We test the method with fluorescently labeled DNA and we demonstrate the possibility of extraction FRET efficiency in presence of non-interacting and interacting donor molecules.

REFERENCES

1. B. Valeur, *Molecular fluorescence: principles and applications* (Wiley-Vch, 2012).

2. J. Lakowicz, "Principles of Fluorescence spectroscopy. 1999," Kluwer Academic/Plenum Publisher, New York, Kap **9,**.

3. L. Van Geest and K. W. J. Stoop, "FLIM on a wide field fluorescence microscope," International Journal of Peptide Research and Therapeutics **10,** 501-510 (2003).

4. H. Gerritsen, M. Asselbergs, A. Agronskaia, and W. Van Sark, "Fluorescence lifetime imaging in scanning microscopes: acquisition speed, photon economy and lifetime resolution," J. Microsc. **206,** 218-224 (2002).

5. M. Dickinson, G. Bearman, S. Tille, R. Lansford, and S. Fraser, "Multi-spectral imaging and linear unmixing add a whole new dimension to laser scanning fluorescence microscopy," BioTechniques **31,** 1272-1279 (2001).

6. J. A. Palero and H. S. De Bruijn, "Spectrally resolved multiphoton imaging of in vivo and excised mouse skin tissues," Biophys. J. **93,** 992 (2007).

7. F. Fereidouni, A. N. Bader, and H. C. Gerritsen, "Spectral phasor analysis allows rapid and reliable unmixing of fluorescence microscopy spectral images," Optics Express **20,** 12729-12741 (2012).

8. R. A. Neher, M. Mitkovski, F. Kirchhoff, E. Neher, F. J. Theis, and A. Zeug, "Blind source separation techniques for the decomposition of multiply labeled fluorescence images," Biophys. J. **96,** 3791-3800 (2009).

9. M. R. Hight, D. D. Nolting, E. T. McKinley, A. D. Lander, S. K. Wyatt, M. Gonyea, P. Zhao, and H. C. Manning, "Multispectral fluorescence imaging to assess pH in biological specimens," J. Biomed. Opt. **16,** (2011).

10. Y. Chen, J. P. Mauldin, R. N. Day, and A. Periasamy, "Characterization of spectral FRET imaging microscopy for monitoring nuclear protein interactions," J. Microsc. **228,** 139-152 (2007).

11. J. A. Palero, A. N. Bader, H. S. de Bruijn, A. P. van den Heuvel, H. J. C. M. Sterenborg, and H. C. Gerritsen, "In vivo monitoring of protein-bound and free NADH during ischemia by nonlinear spectral imaging microscopy," Biomedical optics express **2,** 1030-1039 (2011).

12. R. Sanders, A. Draaijer, H. C. Gerritsen, P. M. Houpt, and Y. K. Levine, "Quantitative pH imaging in cells using confocal fluorescence lifetime imaging microscopy," Anal. Biochem. **227,** 302-308 (1995).

13. M. K. Kuimova, G. Yahioglu, J. A. Levitt, and K. Suhling, "Molecular rotor measures viscosity of live cells via fluorescence lifetime imaging," J. Am. Chem. Soc. **130,** 6672-6673 (2008).

14. H. C. Gerritsen, R. Sanders, A. Draaijer, C. Ince, and Y. Levine, "Fluorescence lifetime imaging of oxygen in living cells," J. Fluoresc. **7,** 11-15 (1997).

15. J. R. Lakowicz, H. Szmacinski, K. Nowaczyk, and M. L. Johnson, "Fluorescence lifetime imaging of free and protein-bound NADH," Proceedings of the National Academy of Sciences **89,** 1271-1275 (1992).

16. F. Fereidouni, A. Esposito, G. Blab, and H. Gerritsen, "A modified phasor approach for analyzing time-gated fluorescence lifetime images," J. Microsc. **244,** 248-258 (2011).

17. A. Esposito, H. C. Gerritsen, and F. S. Wouters, "Fluorescence lifetime heterogeneity resolution in the frequency domain by lifetime moments analysis," Biophys. J. **89,** 4286 (2005).

18. H. Wallrabe and A. Periasamy, "Imaging protein molecules using FRET and FLIM microscopy," Curr. Opin. Biotechnol. **16,** 19-27 (2005).

19. Q. S. Hanley, D. J. Arndt-Jovin, and T. M. Jovin, "Spectrally resolved fluorescence lifetime imaging microscopy," Appl. Spectrosc. **56,** 155-166 (2002).

20. Q. S. Hanley, "Spectrally resolved fluorescent lifetime imaging," Journal of The Royal Society Interface **6,** S83-S92 (2009).

21. D. O'connor, W. Ware, and J. Andre, "Deconvolution of fluorescence decay curves. A critical comparison of techniques," J. Phys. Chem. **83,** 1333-1343 (1979).

22. K. K. Sharman, A. Periasamy, H. Ashworth, J. Demas, and N. Snow, "Error analysis of the rapid lifetime determination method for double-exponential decays and new windowing schemes," Anal. Chem. **71,** 947-952 (1999).

23. A. Gafni, R. L. Modlin, and L. Brand, "Analysis of fluorescence decay curves by means of the Laplace transformation," Biophys. J. **15,** 263-280 (1975).

24. U. P. Wild, A. R. Holzwarth, and H. P. Good, "Measurement and analysis of fluorescence decay curves," Rev. Sci. Instrum. **48,** 1621-1627 (1977).

25. J. A. Jo, Q. Fang, T. Papaioannou, and L. Marcu, "Fast model-free deconvolution of fluorescence decay for analysis of biological systems," J. Biomed. Opt. **9,** 743-752 (2004).

26. S. Schlachter, A. Elder, A. Esposito, G. Kaminski, J. Frank, L. Van Geest, and C. Kaminski, "mhFLIM: resolution of heterogeneous fluorescence decays in widefield lifetime microscopy," Optics express **17,** 1557-1570 (2009).

27. M. A. Digman, V. R. Caiolfa, M. Zamai, and E. Gratton, "The phasor approach to fluorescence lifetime imaging analysis," Biophys. J. **94,** L14-L16 (2008).

28. C. Stringari, A. Cinquin, O. Cinquin, M. A. Digman, P. J. Donovan, and E. Gratton, "Phasor approach to fluorescence lifetime microscopy distinguishes different metabolic states of germ cells in a live tissue," Proceedings of the National Academy of Sciences **108,** 13582-13587 (2011).

29. T. Zimmermann, "Spectral imaging and linear unmixing in light microscopy," Microscopy Techniques 1308-1310 (2005).

30. H. Shirakawa and S. Miyazaki, "Blind spectral decomposition of single-cell fluorescence by parallel factor analysis," Biophys. J. **86,** 1739-1752 (2004).

31. I. Jolliffe, *Principal component analysis* (Wiley Online Library, 2005).

32. D. Chorvat Jr, J. Kirchnerova, M. Cagalinec, J. Smolka, A. Mateasik, and A. Chorvatova, "Spectral unmixing of flavin autofluorescence components in cardiac myocytes," Biophys. J. **89,** L55 (2005).

33. Q. S. Hanley, D. J. Arndt-Jovin, and T. M. Jovin, "Spectrally resolved fluorescence lifetime imaging microscopy," Appl. Spectrosc. **56,** 155-166 (2002).

34. D. K. Bird, K. W. Eliceiri, C. H. Fan, and J. G. White, "Simultaneous two-photon spectral and lifetime fluorescence microscopy," Appl. Opt. **43,** 5173-5182 (2004).

35. P. D. Beule, D. M. Owen, H. B. Manning, C. B. Talbot, J. Requejo-Isidro, C. Dunsby, J. Mcginty, R. K. P. Benninger, D. S. Elson, and I. Munro, "Rapid hyperspectral fluorescence lifetime imaging," Microsc. Res. Tech. **70,** 481-484 (2007).

36. J. P. Knemeyer, N. Marmé, and J. D. Hoheisel, "Spectrally resolved fluorescence lifetime imaging microscopy (SFLIM)—an appropriate method for imaging single molecules in living cells," Analytical and bioanalytical chemistry **387,** 37-40 (2007).

37. S. Shrestha, B. E. Applegate, J. Park, X. Xiao, P. Pande, and J. A. Jo, "High-speed multispectral fluorescence lifetime imaging implementation for< i> in vivo</i> applications," Opt. Lett. **35,** 2558-2560 (2010).

38. Q. Hanley and A. Clayton, "AB-plot assisted determination of fluorophore mixtures in a fluorescence lifetime microscope using spectra or quenchers," J. Microsc. **218,** 62-67 (2005).

39. Y. C. CHEN and R. Clegg, "Spectral resolution in conjunction with polar plots improves the accuracy and reliability of FLIM measurements and estimates of FRET efficiency," J. Microsc. **244,** 21-37 (2011).

40. T. S. Forde and Q. S. Hanley, "Spectrally resolved frequency domain analysis of multi-fluorophore systems undergoing energy transfer," Appl. Spectrosc. **60,** 1442-1452 (2006).

41. D. Strat, F. Dolp, B. von Einem, C. Steinmetz, C. A. F. von Arnim, and A. Rueck, "Spectrally resolved fluorescence lifetime imaging microscopy: Förster resonant energy transfer global analysis with a one- and two-exponential donor model," J. Biomed. Opt. **16,** 026002-026002-19 (2011).

2

A modified phasor approach for analyzing time-gated fluorescence lifetime images

Published in: Journal of Microscopy .244(3), 248–258 (2011).

ABSTRACT

Fluorescence lifetime imaging is a versatile tool that permits mapping the biochemical environment in the cell. Among various fluorescence lifetime imaging techniques, time correlated single photon counting (TCSPC) and time gating methods have been demonstrated to be very efficient and robust for the imaging of biological specimens.

Recently, the phasor representation of lifetime images became popular because it provides an intuitive graphical view of the fluorescence lifetime content of the images and, when used for global analysis, significantly improves the overall S/N of lifetime analysis. Compared to TCSPC, time gating methods can provide higher count rates (~10 MHz) but at the cost of truncating and under sampling the decay curve due to the limited number of gates commonly used. These limitations also complicate the implementation of the phasor analysis for time-gated data. In this work, we propose and validate a theoretical framework that overcomes these problems. This modified approach is tested on both simulated lifetime images and on cells. We demonstrate that this method is able to retrieve two lifetimes from time gating data that cannot be resolved using standard (non-global) fitting techniques. The new approach increases the information that can be obtained from typical measurements and simplifies the analysis of fluorescence lifetime imaging data.

INTRODUCTION

Lifetime imaging has become an important tool in life sciences. The lifetime of the excited state of fluorophores ranges from picoseconds to micro seconds and provides valuable information on the state of the fluorescent molecules and their immediate molecular environment including temperature, pH, viscosity, ionic concentration and oxygen saturation [1-3]. Lifetime imaging can be employed to probe the local environment of the fluorescent molecules [4], to discriminate different molecules (fluorophores) [5, 6] and to detect molecular interactions at the nanometer scale [7, 8]. The latter is accomplished by monitoring the lifetime reduction of the donor dye molecules caused by Förster Resonance Energy Transfer (FRET) to spectrally-matched acceptor molecules [9]. FRET can not only be used to image molecular interactions but also to measure distances on the nanometer scale [10-12].

In many cases the measured fluorescence decay curve is modeled as a mono-exponential function. Often, however, multiple molecular species at different concentrations or fluorophores exhibiting bi-exponential decays are present in the specimen. Therefore, resolving lifetimes and concentrations of each species in the same volume requires multi-exponential fitting of the experimental fluorescence decays.

High signal-to-noise (S/N) ratios are required for the reliable analysis of multi-exponential decays. The dependence of the relative error and separability of lifetimes on the number of detected photons has been extensively studied [13-15]; for instance, it was found that separating two lifetime components that differ by a factor of two requires at least 1000 detected photons per pixel [16]. The collection of thousands of photons per pixel with biological samples is challenging because of photo bleaching, imaging speed and saturation of the detection system.

As an alternative to a per pixel analysis, global analysis methods can be employed to improve the accuracy of data analyses [17]. In global approaches, it is assumed that the fluorescence lifetimes in the whole image are spatially-invariant and only the relative concentrations of the fluorescent species (amplitudes of the individual components) varying at each pixel location. It was shown that the accuracy of the analyses improves because the signal of a large number of pixels is used to resolve multi-exponential decays [18].

The phasor approach (also referred to as AB-plot) has been employed for the global analysis of frequency domain lifetime data [6, 19]. This method simplifies the analysis of lifetime images and offers a graphical approach to analyse lifetime distributions and fractional concentrations of fluorophores. Briefly, phase and modulation values of each pixel are converted to real and imaginary parts and the result are presented in a two dimensional plot. Here, the y-axis is the imaginary axis and x is the real axis. The phasor approach can also be employed for analysing time domain data [20]. In this case, the

imaginary and real parts of the Fourier transformation (FT) of the fluorescence decay curves of each pixel are mapped as points in the phasor plot. Again, each point in this two dimensional histogram corresponds to the pixels of the lifetime image.

Implementing the phasor method for the analysis of fluorescence lifetime images recorded using Time Gating is potentially interesting. Photon counting based Time Gating electronics have a low dead-time and can therefore in general handle higher count rates than TCSPC methods. As a result, Time Gating is well suited for rapid image acquisition [21, 22]. However, in Time Gating the gates are usually comparatively long and only a limited number of gates are employed [23]. Moreover, fluorescence is in general acquired in a limited time range; as a result part of the decay is not recorded. Importantly, due to the limited number of gates the sampling of the decay curve is not compatible with the standard implementation of the phasor method. This renders the original phasor method not adequate for the analysis of time gated lifetime images.

In this paper we present a modification of the phasor analysis method that takes into account the sampling limitations in time gated detection and make it compatible with time gated data. This modified approach is tested on both simulated lifetime images and on 3T3 2.2 cells transfected with glycosylphosphatidylinositol fused to green fluorescent protein (GPI-GFP) and incubated with cholera toxin sub-unit B labeled with Alexa-594 (CTB-Alexa). In addition we measured FRET efficiencies in cells transfected with EGFR-GFP and mcherry. We demonstrate that this method can be applied to retrieve two lifetimes from time gating data that cannot be resolved using standard (non-global) fitting techniques.

MEASURING LIFETIME

Here, we will restrict ourselves to the single photon counting based lifetime detection methods often used in laser scanning microscopes. Complete decay curves can be recorded using time-correlated single photon counting (TCSPC) systems. Due to the large number of narrow time channels, typically 128-1024, TCSPC affords the recording of complete fluorescence decay curves with high time resolution. TCSPC imaging generally requires comparatively long acquisition times; operating TCSPC systems at high count rates, results in pulse pile-up which distorts the recorded decay curve [1].

In Time Gating, the fluorescence emission is detected in two or more time gates. In optimized schemes the gates open sequentially after excitation of the sample with a laser pulse [21]. Time gated data can be recorded at high count rates (~ 10 MHz); in practice the maximum count rate is limited by the detector. The high maximum count rate in Time Gating is due to the low dead time of the detection electronics (<1 ns). The dead time of TCSPC electronics is usually on the order of 100–350 ns which results in pulse pile-up and loss of signal at high count rates [22].

The measured decay curve is the convolution of the fluorescence decay function with the instrument response function (IRF). In TCSPC this is taken into account in the analyses by

data fitting algorithms. In Time Gating the effect of the IRF is usually ignored by applying an offset between the laser pulse and the opening of the first gate. In this way the later part of the signal is measured where the instrument response function has dropped to zero. This also offers the possibility to suppress background signals like Raman scattering or auto fluorescence which improves the signal to background ratio of the images.

In spite of the relatively long gate durations (usually > 500 ps) and the limited number of time channels (2 to 8) the lifetime of the single exponential decays can be accurately determined with proper gate settings [24]. Moreover, even multi-exponential decays can be detected when the number of gates is large enough [14].

THEORY

Application of the phasor approach to analyse time domain data requires Fourier transformation from time zero to infinity. In practice the narrow time bins and long acquired time range make implementation of the phasor approach to analyse TCSPC data straight-forward. However, in time gating techniques the decay is under sampled and the recorded time range is more limited. Therefore, a revised phasor analyses is required to analyse time gated data. The standard phasor analyses method has been described in detail previously [20]. Briefly, $d(t)$ the fluorescence response of a multi-exponential decay to pulsed laser excitation can be described by a sum of Q exponentials:

$$d(t) = \sum_{q=1}^{Q} a_q e^{(-t/\tau_q)} \quad , \quad \text{for } t < 0 \quad d(t) = 0 \qquad (1)$$

Where τ_q is the lifetime of the q-th species, and a_q is the pre-exponential coefficient. The Fourier transformation of *d(t)* at frequency ω is given by:

$$D(\omega) = \frac{\int_0^\infty d(t) e^{j\omega t} dt}{\int_0^\infty d(t) dt} = \sum_{q=1}^{Q} \frac{\alpha_q}{1 - j\omega\tau_q} \qquad (2)$$

The normalization integral in the denominator allows rewriting the pre-exponential coefficient a_q into α_q, the fractional contribution of the q-th exponential to the average fluorescence intensity.

$$\alpha_q = \frac{\int_0^\infty a_q e^{\frac{-t}{\tau_q}} dt}{\int_0^\infty d(t)dt} = \frac{a_q \tau_q}{\sum_{q'=1}^{Q} a_{q'} \tau_{q'}} \quad (3)$$

For each pixel in an image with index *i,* Eq. (2) can be rewritten as:

$$D_i(\omega) = \sum_{q=1}^{Q} \alpha_{i,q} R(\tau_q, \omega) \quad (4)$$

Where $R(\tau, \omega)$ is defined as:

$$R(\tau, \omega) = \frac{\int_0^\infty e^{-t/\tau} e^{j\omega t} dt}{\int_0^\infty e^{-t/\tau} dt} = \frac{1}{1 - j\omega\tau} \quad (5)$$

For a bi-exponential decay α_i is in the range 0 to 1 which simplifies Eq. 4 to:

$$D_i(\omega) = (1 - \alpha_i) R_1(\omega) + \alpha_i R_2(\omega) \quad (6)$$

Where $R_1 = R(\tau_1, \omega)$ and $R_2 = R(\tau_2, \omega)$

A linear relationship exists between the imaginary and real components of *D* that can be written as [20]:

$$\text{Im } D_i(\omega) = u + v \,\text{Re}\, D_i(\omega) \quad (7)$$

With

$$u = \frac{\text{Im}(R_2^* R_1)}{\text{Re}(R_2 - R_1)} \quad \text{and} \quad v = \frac{\text{Im}(R_2 - R_1)}{\text{Re}(R_2 - R_1)} \quad (8)$$

For single exponential decays with lifetimes in the range 0 - ∞ plotting the imaginary versus the real part of $R(\tau, \omega)$ for $0 < \omega\tau < \infty$ results in a semicircle. Mixtures of two single exponential decays fall on a straight line given by Eq. (7) which intersects the semicircle at two points corresponding to the two fluorescence lifetimes:

$$\tau_{1,2} = \frac{1 \pm \sqrt{1 - 4u(u+v)}}{2\omega u} \quad (9)$$

For measurements with a discrete number of time bins of equal width, like time gating and TCSPC, Eq. (5) can be rewritten as:

$$R'(\tau,n\omega)=\frac{\int_0^T\left(\int_{t-\frac{T}{2K}}^{t+\frac{T}{2K}}e^{-\frac{t'}{\tau}}dt'\right)e^{jn\omega t}\times\sum_{m=-\infty}^{\infty}\delta\left(t-\left(m+\frac{1}{2}\right)\frac{T}{K}\right)dt}{\int_0^T\left(\int_{t-\frac{T}{2K}}^{t+\frac{T}{2K}}e^{-\frac{t'}{\tau}}dt'\right)\times\sum_{m=-\infty}^{\infty}\delta\left(t-\left(m+\frac{1}{2}\right)\frac{T}{K}\right)dt}$$

$$=\frac{\sum_{m=0}^{K-1}\left(e^{-\frac{mT}{\tau K}}\left(1-e^{-\frac{1}{\tau}\frac{T}{K}}\right)\tau\right)e^{jn\omega\left(m+\frac{1}{2}\right)\frac{T}{K}}}{\tau\left(1-e^{-\frac{T}{\tau}}\right)}=\frac{\sinh\left(\frac{T}{2K\tau}\right)}{\sinh\left(\frac{1-jn\omega\tau}{\frac{2K\tau}{T}}\right)} \tag{10}$$

With K is the number of time bins, m the bin index, *n* the harmonic number, $\omega=2\pi/T$ and *T* the total time range of detection. The original continuous decay is described by $e^{-\frac{t}{\tau}}$; here, it is replaced by:

$$\left(\int_{t-\frac{T}{2K}}^{t+\frac{T}{2K}}e^{-\frac{t'}{\tau}}dt'\right)\times\sum_{m=-\infty}^{\infty}\delta\left(t-\frac{(m+1/2)}{\tau}\frac{T}{K}\right)$$

to take into account the width of the detection bins. Where δ is the Dirac delta function. We note that in Eq. 10 although the summation runs from m=-∞ to +∞, the integration from 0 to T effectively restricts the summation to *m=0* to *K-1*. The summation from –∞ to +∞ is mathematically more convenient because of its compatibility with the Fourier Transform. Now we can rewrite Eq. 10 into:

$$R(\tau,n\omega)=\frac{\int_{-\infty}^{\infty}\left(e^{\frac{T}{2K\tau}}-e^{-\frac{T}{2K\tau}}\right)\tau e^{-\frac{t}{\tau}}\Pi_{0,T}(t)\times\sum_{m=-\infty}^{\infty}\delta\left(t-\left(m+\frac{1}{2}\right)\frac{T}{K}\right)e^{jn\omega t}dt}{\tau\left(1-e^{-\frac{T}{\tau}}\right)}$$

$$=\frac{\tau}{1-jn\omega\tau}\left(e^{\frac{T}{2K\tau}}-e^{-\frac{T}{2K\tau}}\right)\otimes\sum_{m=-\infty}^{\infty}\delta\left(n\omega-2\pi\frac{mK}{T}\right)(-1)^m\frac{K}{T}$$

$$=\sum_{m=-\infty}^{\infty}\frac{\tau}{1-j\left(n\omega-2\pi\frac{mK}{T}\right)\tau}(-1)^m\frac{K}{T}\left(e^{\frac{T}{2K\tau}}-e^{-\frac{T}{2K\tau}}\right)$$

(11)

Where $\otimes$ denotes the convolution operator and $\Pi_{0,T}(t)$ the boxcar function which is equal to 1 for 0<t<T and 0 otherwise. For $\tau > T/K$ Eq. 11 can be approximated by:

$$R(\tau,n\omega)=\sum_{m=-\infty}^{\infty}\frac{1}{1-j\left(n\omega-2\pi\frac{mK}{T}\right)\tau}(-1)^m \qquad (12)$$

Compared to Eq. 5, which is obtained without truncation and discrete sampling, this equation repeats every $2\pi K/T$. The periodicity is due to the discrete sampling of the decay curve. Examples of the Fourier transformation of decay curves for different numbers of gates and lifetime $\tau/T=1/2$ are shown in Fig.1. The 'fast' ripples in the curves are the result of truncation effects and the periodicity is the consequence of the discrete sampling of the decay curve. As K increases the period increases and the curves get closer to the continuous Fourier transform at the harmonics. It is straightforward to show that if $K\to\infty$ then the $R'(\tau,n\omega)$ at the harmonics converges to $1/(1-jn\omega\tau)$. Truncation does not alter the Fourier transform at the harmonics. It is, however, affected by sampling. The reference semicircle is generated by plotting the Imaginary part of $R(\tau)$ versus the real part which can be done by using Eq. (5). For low number of gates and discrete measurements we need to use the modified equation which is given by Eq.10. Fig.2 shows the modified reference semicircle at the first harmonic $(\omega=2\pi/T)$ for different gate numbers and the same total window for a lifetime range from $\tau/T=0.01$ to $\tau/T=5$. Interestingly, even for a low number of gates the deviation of the modified semicircle at long lifetimes (small values of R) from the standard semicircle is small. By increasing the number of gates the modified semicircle gets closer to the standard semicircle in particular for shorter lifetimes. We can rewrite D for discrete time measurements at the nth harmonic, D' as:

$$D'_n = \frac{\sum_{m=0}^{K-1}\sum_{q=1}^{Q}\left(a_q e^{-\frac{m}{\tau}\frac{T}{K}}\left(1-e^{-\frac{1}{\tau_q}\frac{T}{K}}\right)\tau_q\right)e^{jn\omega\left(m+\frac{1}{2}\right)\frac{T}{K}}}{\sum_{q=1}^{Q}a_q\tau_q\left(1-e^{-\frac{T}{\tau}}\right)} =$$

$$= \sum_{q=1}^{Q}\alpha_q \frac{\sinh\left(\frac{T}{2K\tau_q}\right)}{\sinh\left(\frac{1-jn\omega\tau_q}{\frac{2K\tau_q}{T}}\right)} = \sum_{q=1}^{Q}\alpha_q R'(\tau_q, n\omega) \qquad (13)$$

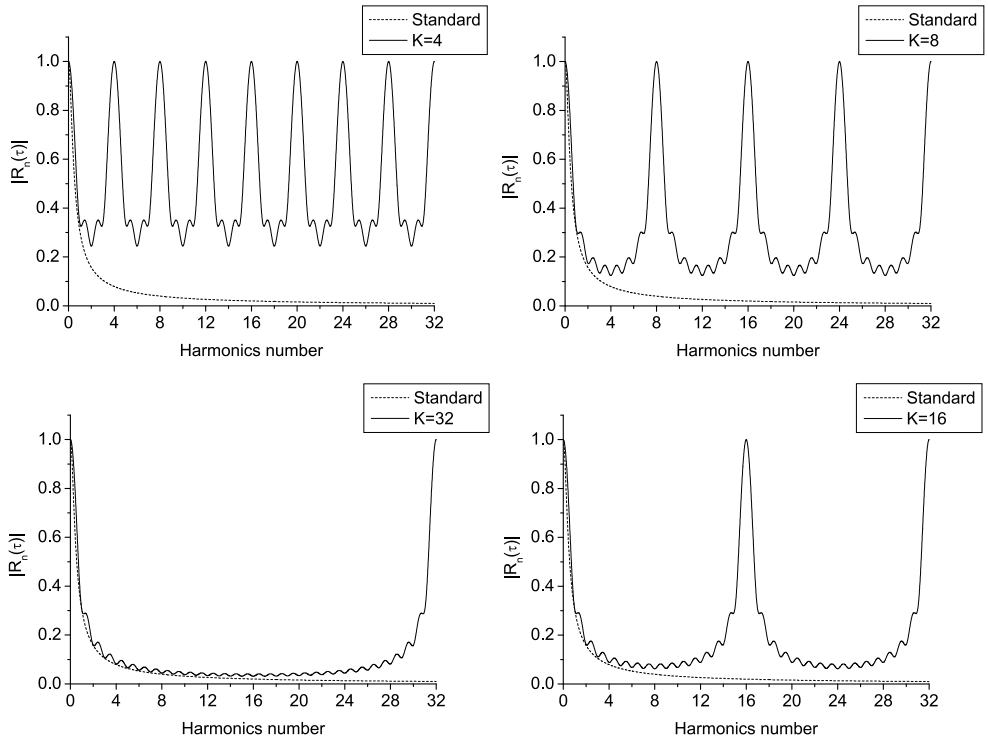

Fig. 1 The Fourier transform of decay curves recorded with different gate numbers (K=4, 8, 16 and 32), the same total time window width T and a lifetime of $\tau / T = 1/2$.

with: $$\alpha_q = \frac{a_q\tau_q\left(1-e^{-\frac{T}{\tau_q}}\right)}{\sum_{q'=1}^{Q} a_q\tau_q\left(1-e^{-\frac{T}{\tau_{q'}}}\right)} \qquad (14)$$

Eq. 13 shows that in the case of a bi-exponential decay, Eqs. (6) and (7) are still applicable and there is a linear relationship between imaginary and real parts of the Fourier transformation of the decay curve. This line will connect all noiseless mixtures of two components defined by Eq. (13) and the intersections with the adapted semicircle correspond to the two lifetimes which now can be evaluated by:

$$\tau_{1,2} = \frac{T/2K}{Arc\coth\left(\pm\frac{\sqrt{1-2u^2-4uv\cos\left(\frac{\pi}{K}\right)-2u^2\cos\left(\frac{2\pi}{K}\right)}\pm 1}{2u\sin\left(\frac{\pi}{K}\right)}\right)} \qquad (15)$$

This approach is illustrated in Fig.3 for a bi-exponential decay curve with two lifetimes with $\tau_1/T = 0.2$ (R_1), $\tau_2/T = 0.4$ (R_2) and fractional intensity $\alpha = 0.5$. Here, the adapted semicircle for a system with 4 gates is employed.

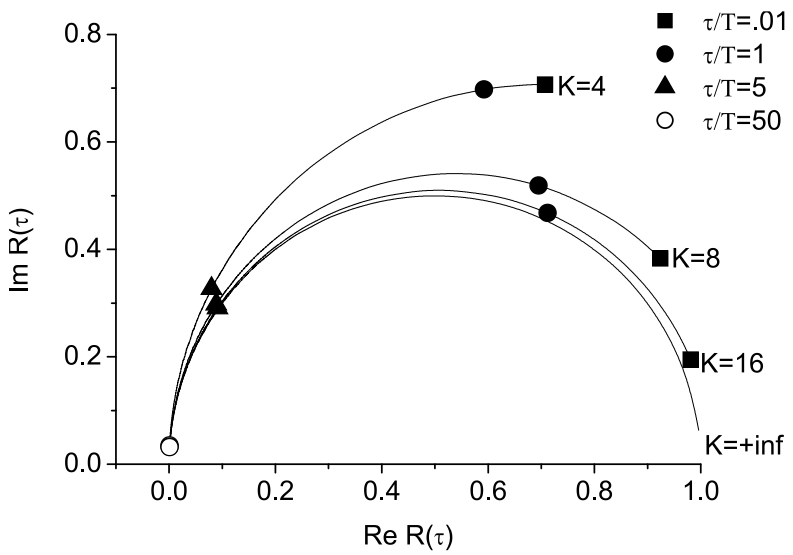

Fig.2 (a) Plot of the modified semi-circle $\mathrm{Im}\,R(\tau)$ vs. $\mathrm{Re}\,R(\tau)$. The curve shows all possible single component lifetimes from $\tau/T = .01$ to $\tau/T = 50$ at $\omega = 2\pi/T$

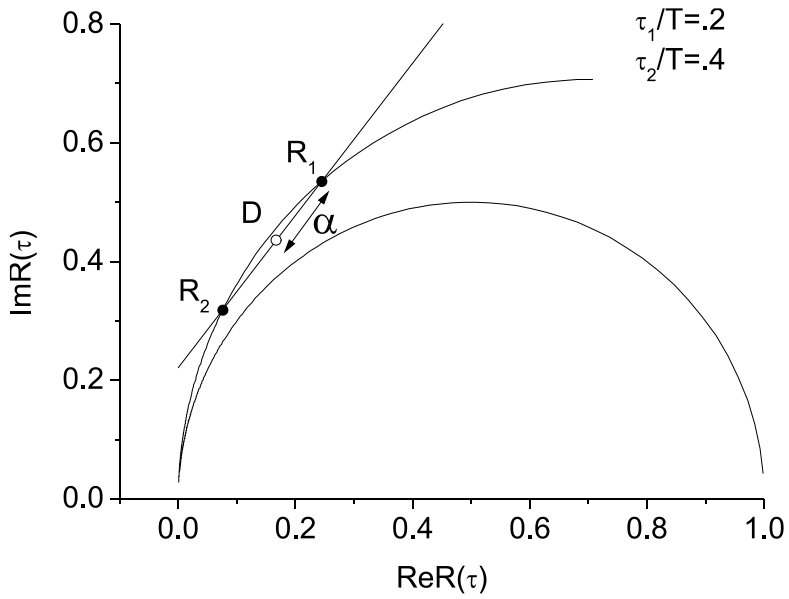

Fig.3 The standard and modified semicircle for a system with 4 gates. The phasor of a bi-exponential decay curve with lifetimes $\tau_1 / T = 0.2$, $\tau_2 / T = 0.4$ and fractional intensity $\alpha = 0.5$ (open circle) is shown. R_1 and R_2 correspond to lifetimes of $\tau_1 / T = 0.2$ and $\tau_2 / T = 0.4$ filled circles.

METHODS AND MATERIALS

Simulations

Simulations were programmed in Compaq visual FORTRAN using the IMSL math library. Exponential decay curves were generated for a pre-set total photon count and binned to simulate truncation and sampling by time gating. Next, Poisson noise was added to each time gate. This procedure was repeated for different numbers of gates (K = 4, 8 and 16) using the same fixed total gate width. Phasor diagrams of the simulated images were calculated using Eq.16. 1000 images were simulated with size 100x100 pixels and two fixed lifetimes τ_1 and τ_2. α, the fraction of the short lifetime fluorescence, was varied between 0 and 1 from the upper left to the lower right of the image.

The $\sum_{q=1}^{Q}\left(a_q e^{-\frac{m}{\tau}\frac{T}{K}}\left(1-e^{-\frac{1}{\tau_q}\frac{T}{K}}\right)\tau_q \right)$ term in Eq. 13 was replaced by $N_{i,m}$, the simulated number of counts in the ith pixel and mth gate. Next, the Fourier transformation of the ith pixel and nth harmonic was carried out using:

$$D_{i,n} = \frac{\sum_{m=0}^{K-1} N_{i,m} e^{jn\omega(m+1/2)T}}{\sum_{m=0}^{K-1} N_{i,m}} \quad (16)$$

Applying this equation to all image points yields the data points for a phasor plot. A straight line was fitted through the clouds of points in the phasor diagrams and the intersection of the line with the (adapted) reference curves was calculated using Eq.15. Here, the orthogonal least square method [25] was employed to fit the line. This provided significantly better results than the ordinary least square method; it is more accurate in the case that both dependent and independent variables contain errors.

To investigate the accuracy of the modified phasor approach for separating two lifetimes in simulated images we employed the index of separability *S* [15]. This index is defined for a system with two lifetimes τ_1 and τ_2 as:

$$S = \frac{|\tau_2 - \tau_1|}{\sqrt{\mathrm{var}(\tau_2) + \mathrm{var}(\tau_1)}} \quad (17)$$

Where *var* is the variance of the estimated lifetime. A higher value of *S* indicates better separability of the two lifetimes. When S<1 the two components are considered to be non-separable. In general an *S* value of 2 is required for separability.

Imaging experiments

A 473 nm solid state diode laser (Becker & Hickl, BDL-473-SMC) with a pulse repetition rate of 50 MHz was coupled into a confocal microscope (Nikon C1, Japan). Imaging of solutions of Rhodamine-B and Fluorescein was performed using a 10x objective (NA = 0.3 Nikon, Japan); images of cells transfected with GPI-GFP and CTB-Alexa-594 were acquired with a 60x water immersion objective (NA = 1.2, Nikon, Japan). Fluorescence was detected by a fibre coupled PMT with a GaAsP photocathode (H7422P-40, Hamamatsu Japan). In the FRET measurements donor emission was selected by a 515/30 nm band pass filter. The output of the PMT was fed into a 4 channel time-gating module (LIMO, Nikon Europe BV, Netherlands)[21]. The time gates were all set to a width of 2ns and the opening of the first gate was delayed 0.5 ns with respect to the excitation pulse. The instrument response function was accounted for by reference measurements on a solution of Fluorescein. TCSPC measurements on this solution yielded mono-exponential decay with a lifetime of 3.98 ns. The phasor of Fluorescein falls on the adapted semicircle and serves as a reference for the other measurements. The reference measurement was repeated using the LIMO system to calibrate the time gated measurements. All experiments were carried out at room temperature.

Sample preparation

COS-cells were transfected with EGFR-eGFP and mCherry and 3T3 2.2 cells were transfected with GPI-GFP using FugeneHD (Roche, Mannheim, Germany). 3T3 2.2 cells were further incubated with CTB-AlexaFluor-594 (Invitrogen, Breda, The Netherlands). Both samples were subsequently fixed using formaldehyde (Polysciences, Eppelheim, Germany), embedded in Mowiol (Polysciences) and stored at -20°C until further use.

Spectral un-mixing

As a comparison to the lifetime un-mixing results, spectral un-mixing experiments were performed based on measurements recorded in two different detection channels. GPI-GFP fluorescence was detected with the 515/30 nm band pass filter and the CTB-Alexa emission using a 660nm long pass filter. The results of spectral un-mixing are not corrected for bleed through of GPI-GFP in the CTB-Alexa channel and CTB-Alexa in the GFP channel. Correcting bleed through did not significantly improve the spectral un-mixing results. The Manders overlap coefficient [26] was used for a quantitative comparison of the results obtained by lifetime un-mixing and by spectral un-mixing. The value of this coefficient ranges from 0 to 1, with 1 indicating perfect overlap and zero indicating no overlapping of the two images.

RESULTS AND DISCUSSIONS

Numerical Simulation

For different combinations of two normalized lifetimes, τ_1/T and τ_2/T, ranging from 0.1 to 1 and different gate numbers (K=4, 8, 16) the index of separability was calculated as a function of the average number of counts. Fig.4 shows the required number of counts per pixel to obtain an index of separability of 2. This corresponds to the lowest number of counts required to separate the two lifetimes. The smallest difference between the two lifetimes considered here amounts to .05. As expected, the number of photons needed to separate two closely spaced lifetimes is higher than for two less closely spaced lifetimes. As the two lifetime values get closer, the number of required photons for separability increases rapidly. For example, a system with K=4, T=10 ns and lifetimes of $\tau_1 = 3$ ns and $\tau_2 = 3.6$ ns requires 5000 counts per pixel for an S of 2. This number decreases to less than 500 counts for lifetimes of $\tau_1 = 3$ ns and $\tau_2 = 4.6$ ns.

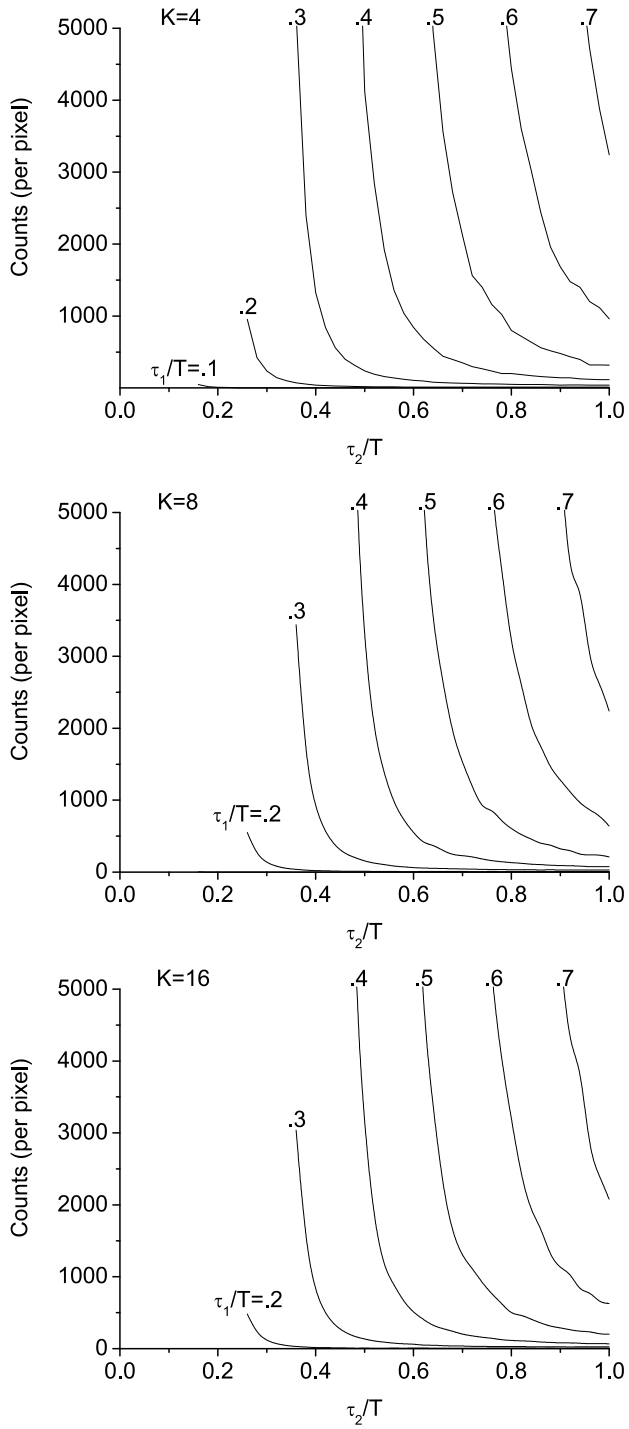

Fig.4 The number of counts per pixel required for separating (S=2) the components of a bi-exponential decay as a function of the second normalized lifetime τ_2 / T . Curves are shown for different normalized lifetimes τ_1 / T and numbers of gates K =4, 8, 16

This amount decreases further when the number of gates increases. Keeping the condition constant and changing the number of gates from 4 to 16 results in a decrease of the required photons to 200 counts per pixel for $\tau_1 = 3$ ns and $\tau_2 = 4.6$ ns. .Under the same conditions a pixel by pixel analyses would require 2.5×10^6 counts per pixel to separate the two lifetimes. This calculation is done based on the estimations described by [15]. Also at longer fluorescence lifetime values, separability of two component mixtures is not achieved. This is due to the truncation of the decay curves that, even at equal number of detected photons, causes a detrimental loss of information and makes the un-mixing algorithms not usable in practical conditions.

Experiments

Images of a binary mixture of Rhodamine-B and Fluorescein in buffer were recorded and analysed using the adapted phasor approach. The concentrations of $8.6 \times 10^{-6} M$ for Fluorescein and $4.8 \times 10^{-5} M$ for Rhodamine-B yielded average intensity ratios of about 1:1 at an excitation wavelength of 473nm.

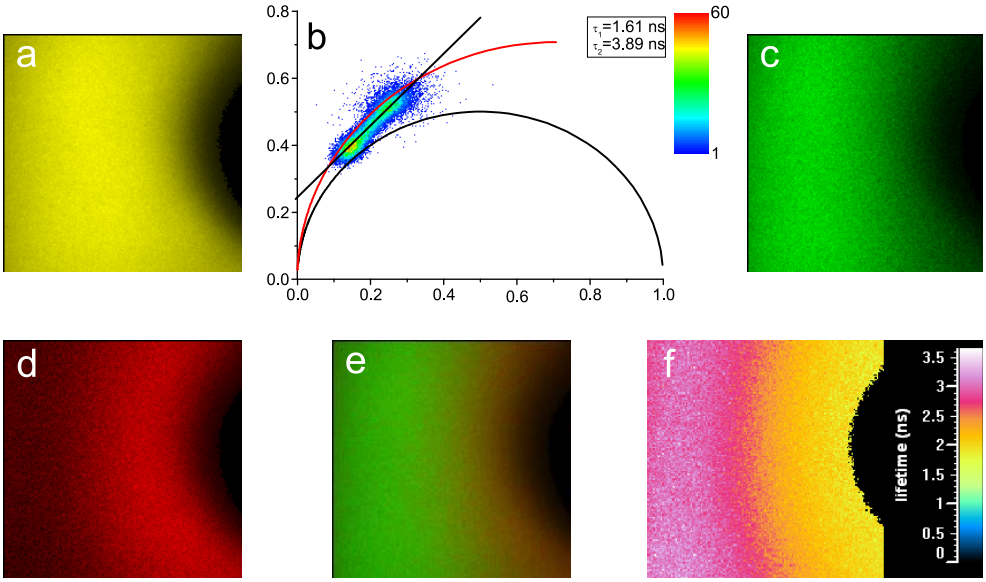

Fig.5 (a) The intensity image of a binary mixture of Rhodamine and Fluorescein.(b) The phasor diagram of the lifetime image of a. The color bar shows the density of points in the phasor cloud. Fractional intensities of Fluorescein (c) and Rhodamine (d) as obtained from the phasor analyses. (e) Overlay of the two distributions. (f) Average lifetime image.

Fig.5 (a) shows the intensity image and (b) the phasor diagram at the first harmonic (125MHz) which corresponds to a total width of the detection window of 8 ns. The straight line is obtained by orthogonal linear regression of points in the phasor plot and it intersects the phasor curve at lifetimes of 1.61 ns and 3.89 ns. These lifetimes are in agreement with reference average lifetimes of pure Rhodamine (1.7 ns) and Fluorescein (3.88 ns) measured

independently by TCSPC. The comparatively short lifetime of Rhodamine is explained by a small amount of scattered light detected in the first gate. The shape of the distribution of points in the phasor plot confirms a gradient distribution of the species. The left side of the plot is dominated by Fluorescein and the right side mainly consists of Rhodamine-B. The fractional intensities of Fluorescein and Rhodamine-B and their overlay are shown in Fig.5(c), 5(d) and 5(e) respectively.

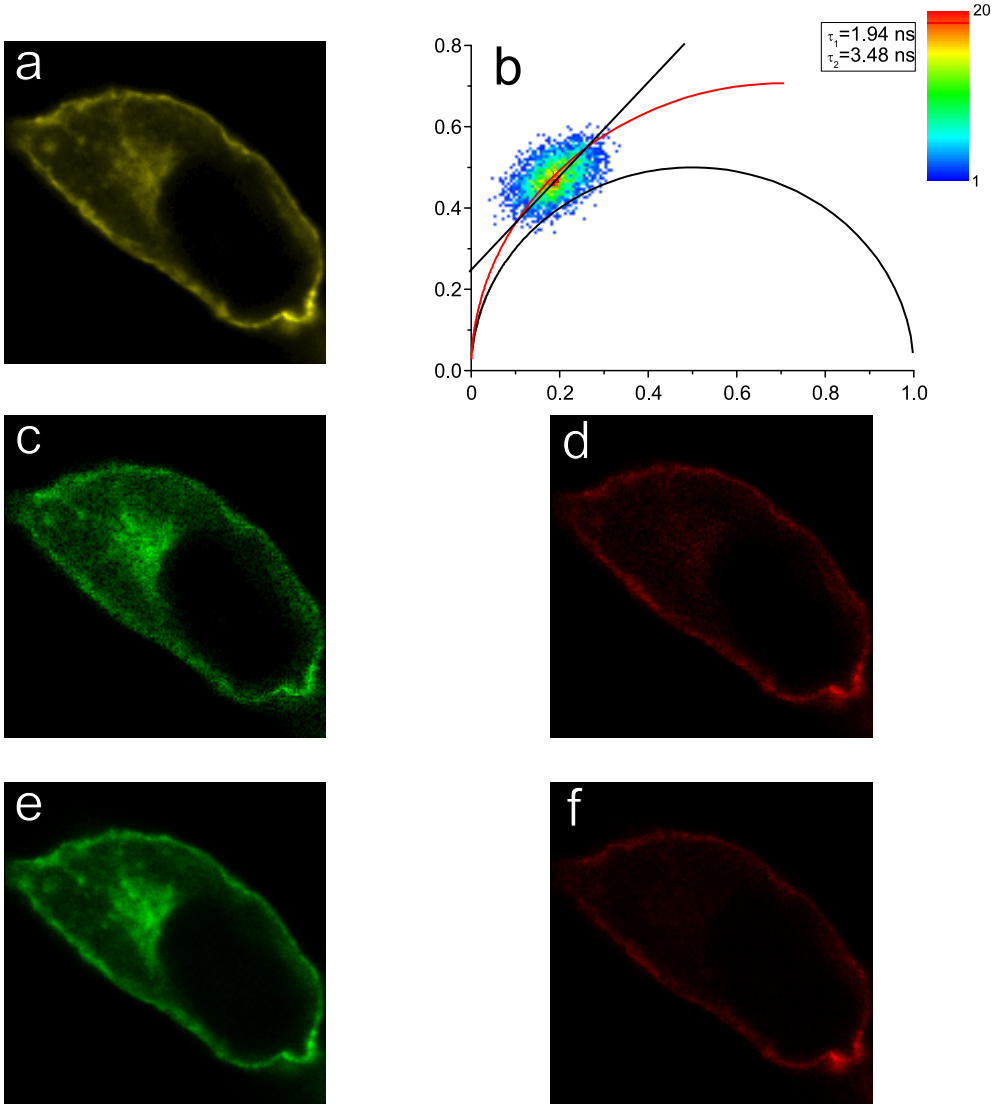

Fig. 6 (a) Intensity image of a cell stained with GPI-GFP and CTB-Alexa 594. (b) Phasor diagram. The color bar shows the density of points in the phasor cloud. Fractional intensities of GPI-GFP (c) and CTB-Alexa (d) as derived from the phasor plot. Spectrally unmixed images of GPI-GFP (515-30nm) (e) and CTB-Alexa 594 (660nm LP) (f).

The fractional intensities were calculated from the positions on the line in the phasor plot connecting the two reference lifetimes. Fig.5(f) shows the average lifetime image; a clear

gradient in the lifetime is observed that qualitatively matches the intensity distributions. The intensity image (54x54 µm2) of a single cell labelled with GPI-GFP and CTB-Alexa 594 is shown in Fig.6a Fig.6(b) shows the phasor plot which reveals fluorescence lifetimes of 1.94 ns for GPI-GFP and 3.48 ns for CTB-Alexa 594. Reference measurements on samples tagged exclusively with GPI-GFP or CTB-Alexa exhibited average lifetimes of 2.10 ns and 3.51 ns, respectively.

The small discrepancy in the short lifetime is again due to the detection of a small amount of scattered light in the first gate. The two components were separated using the phasor analyses results; the fractional intensities of CTB-Alexa and GPI-GFP are depicted in 6(c) and 6(d) respectively. GPI-GFP is mainly present at the plasma membrane and the Golgi apparatus while the CTB-Alexa 594 is predominantly localized at the plasma membrane. As a comparison, also spectral un-mixing results are shown in Fig.6(e) and 6(f) for GPI-GFP and CTB –Alexa respectively.

The results from the lifetime measurements correspond well to the spectral un-mixing results, especially considering the overlap of the two dyes at the plasma membrane. Quantitative comparison of the lifetime and spectral separation of GPI-GFP and CTB-Alexa 594 using the Manders overlap coefficient yielded coefficients of 0.94 and 0.92 respectively. FRET experiments on COS-1 cells expressing EGFR-GFP (donor) and mCherry (acceptor) were carried out by recording fluorescence lifetime images of the donor. Fig.7(a) shows the fluorescence intensity image of the COS-1 cells measured through a 515/30 nm band pass filter and using a 60x water immersion objective.

Fig.7(b) shows the (average) lifetime image and Fig.7(c) the phasor diagram of the lifetime image. Pixels that don't exhibit FRET show up in the phasor plot near the phasor of the unquenched donor (τ_{donor}). Pixels without any donor fluorescence, including pixel where the donor is fully quenched by FRET, are located around the phasor of the autofluorescence background Phasors of quenched donor lifetimes ($\tau_{donor\text{-}acceptor}$) corresponding with other FRET efficiencies $E = 1 - \tau_{donor-acceptor} / \tau_{donor}$ [27]) lie on a curved trajectory connecting the unquenched and quenched positions, see Fig.7(c). Independent time gated measurements were carried out to measure the unquenched donor (2.10 ns) and autofluorescence (2.99 ns) average lifetimes. Next, their phasors were mapped into the phasor plot. The phasor representation can be used for the visual segmentation of FRET images [28]. Selection of pixels on this trajectory can be employed to, for instance, identify regions in the image with 'high' or 'low' FRET efficiencies. The presence of FRET is clearly visible in the phasor plot of Fig. 7 (c); the centre of gravity of the phasor points is clearly shifted to shorter lifetimes with respect to the unquenched donor coordinate.

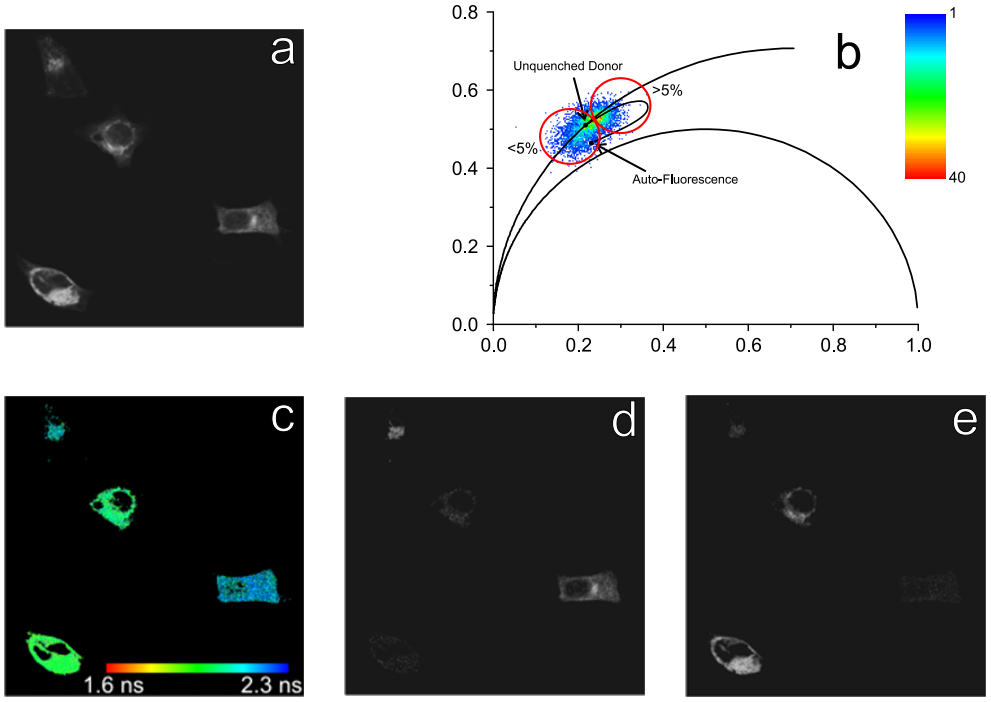

Fig.7 Intensity image of cells expressing GPI-GFP and mCherry. (b) Phasor diagram. The color bar shows the density of points in the phasor cloud. Segmented intensity images for FRET efficiencies <5% (c) Average lifetime image of the cells. (d) and >5% (e).

To discriminate regions in the image with 'low' and 'high' FRET efficiencies, two regions in the phasor plot were selected as indicated by the circles in fig 7 (c). The circle includes about 95% of the pixels when placed in the middle of the cloud and by placing it in the selected regions the higher (>5% efficiency) and lower (<5% efficiency) FRET regions are selected. At the positions indicated in Fig.7 (c) each circle includes ~49% of all pixels. Figs. 7(d), 7(e) show the corresponding, phasor segmented, 'low' and 'high' FRET images respectively.

CONCLUSION

Computationally efficient and robust data analysis methods are crucial for fluorescence lifetime imaging microscopy. In this paper we demonstrated that, after modification the phasor representation and its use for global analysis is also applicable to time gated fluorescence lifetime images. This method provides a fast and intuitive representation of time gated datasets without the need for time consuming nonlinear fitting procedures. In addition the phasor analyses can be also employed as a global approach to extract the lifetimes of two components in a mixture, to estimate fractional contributions of two fluorescent dyes in cells and for the detection of FRET.

Typically, fluorescence lifetime imaging based on time gating provides faster image acquisition rates than TCSPC, and requires similar data analyses. Furthermore Time gating usually does not permit detection of multi-exponential fluorescence decays because of the low number of gates typically used. The combination of phasor analysis with time gating, however, provides high imaging speeds in combination with fast data analysis and quantitative estimation of multi-exponential decays. Regardless of the method used for recording the fluorescence decays, the phasor approach assumes that the fluorophores exhibit mono-exponential decays. When a specimen contains mixtures of fluorophores with multi-exponential decays the estimation of lifetimes and fractional intensities is not straightforward; independent measurements of the two dyes are required to extract the phasors of each component.

We used the separability index to investigate the effect of gate widths on the accuracy of the estimated lifetimes. Longer gate widths reduce the accuracy compared to TCSPC, a finding that is in agreement with previous Figure of merit calculations of lifetime data [24]. However, the average number of counts required to separate two lifetimes in the adapted phasor analyses is considerably lower than in conventional pixel by pixel analysis.

The global nature of phasor analysis permits estimating global parameters (here the two fluorescence lifetime components) with an accuracy determined by the total number of counts in the whole image. Local parameters, (here the fractional contribution of individual fluorophores), can be estimated with an accuracy determined by the number of counts per pixel. By effectively reducing the number of fit parameters, phasor analysis achieves superior accuracies compared to non-global approach at equal photon counts.

Finally, we note that multi-dimensional TCSPC systems are commercially available. The memory constrains of these acquisition boards may force investigators to reduce the number of time bins to those typically used in time gating. Moreover, the huge multi-dimensional lifetime images also call for fast and efficient data analysis methods. Here, the modified phasor approach may be of great value. Therefore, the theoretical framework we developed here may find broader usage than in time gating alone.

An ImageJ plugin for Time gated phasor analyses is available from the author's web site: http://www.Spechron.com/

REFERENCES

1. J. Lakowicz, "Principles of Fluorescence spectroscopy. 1999," Kluwer Academic/Plenum Publisher, New York, Kap **9,**.

2. R. Sanders, A. Draaijer, H. C. Gerritsen, P. M. Houpt, and Y. K. Levine, "Quantitative pH imaging in cells using confocal fluorescence lifetime imaging microscopy," Anal. Biochem. **227,** 302-308 (1995).

3. A. Agronskaia, L. Tertoolen, and H. Gerritsen, "Fast fluorescence lifetime imaging of calcium in living cells," J. Biomed. Opt. **9,** 1230 (2004).

4. M. A. M. J. Van Zandvoort, C. J. De Grauw, H. C. Gerritsen, J. L. V. Broers, M. G. A. Oude Egbrink, F. C. S. Ramaekers, and D. W. Slaaf, "Discrimination of DNA and RNA in cells by a vital fluorescent probe: Lifetime imaging of SYTO13 in healthy and apoptotic cells," Cytometry **47,** 226-235 (2002).

5. G. J. Kremers, E. B. Van Munster, J. Goedhart, and T. W. J. Gadella Jr, "Quantitative lifetime unmixing of multiexponentially decaying fluorophores using single-frequency fluorescence lifetime imaging microscopy," Biophys. J. **95,** 378-389 (2008).

6. A. Clayton, Q. Hanley, and P. Verveer, "Graphical representation and multicomponent analysis of single-frequency fluorescence lifetime imaging microscopy data," J. Microsc. **213,** 1-5 (2004).

7. P. Lu, Z. Yu, R. Alfano, and J. Gersten, "Picosecond studies of energy transfer of donor and acceptor dye molecules in solution," Physical Review A **26,** 3610-3621 (1982).

8. R. Grailhe, F. Merola, J. Ridard, S. Couvignou, C. Le Poupon, J. P. Changeux, and H. Laguitton-Pasquier, "Monitoring protein interactions in the living cell through the fluorescence decays of the cyan fluorescent protein," ChemPhysChem **7,** 1442-1454 (2006).

9. R. Clegg, "Fluorescence Resonance Energy Transfer, Fluorescence Imaging Spectroscopy and Microscopy, vol. 137," John Wiley & Sons, New York **155,** 156 (1996).

10. C. G. dos Remedios and P. D. J. Moens, "Fluorescence Resonance Energy Transfer Spectroscopy Is a Reliable" Ruler" for Measuring Structural Changes in Proteins Dispelling the Problem of the Unknown Orientation Factor," J. Struct. Biol. **115,** 175-185 (1995).

11. A. Hillisch, M. Lorenz, and S. Diekmann, "Recent advances in FRET: distance determination in protein-DNA complexes," Curr. Opin. Struct. Biol. **11,** 201-207 (2001).

12. L. Stryer, "Fluorescence energy transfer as a spectroscopic ruler," Annu. Rev. Biochem. **47,** 819-846 (1978).

13. Ž. Bajzer, T. M. Therneau, J. C. Sharp, and F. G. Prendergast, "Maximum likelihood method for the analysis of time-resolved fluorescence decay curves," European Biophysics Journal **20,** 247-262 (1991).

14. H. Gerritsen, M. Asselbergs, A. Agronskaia, and W. Van Sark, "Fluorescence lifetime imaging in scanning microscopes: acquisition speed, photon economy and lifetime resolution," J. Microsc. **206,** 218-224 (2002).

15. M. Köllner and J. Wolfrum, "How many photons are necessary for fluorescence-lifetime measurements?" Chemical Physics Letters **200,** 199-204 (1992).

16. E. Gratton, S. Breusegem, J. Sutin, Q. Ruan, and N. Barry, "Fluorescence lifetime imaging for the two-photon microscope: time-domain and frequency-domain methods," J. Biomed. Opt. **8,** 381 (2003).

17. P. J. Verveer, A. Squire, and P. I. H. Bastiaens, "Global analysis of fluorescence lifetime imaging microscopy data," Biophys. J. **78,** 2127-2137 (2000).

18. S. Pelet, M. Previte, L. Laiho, and P. So, "A fast global fitting algorithm for fluorescence lifetime imaging microscopy based on image segmentation," Biophys. J. **87,** 2807-2817 (2004).

19. P. J. Verveer and P. I. H. Bastiaens, "Evaluation of global analysis algorithms for single frequency fluorescence lifetime imaging microscopy data," J. Microsc. **209,** 1-7 (2003).

20. H. E. Grecco, P. Roda-Navarro, and P. J. Verveer, "Global analysis of time correlated single photon counting FRET-FLIM data," Optics Express **17,** 6493-6508 (2009).

21. C. De Grauw and H. Gerritsen, "Multiple time-gate module for fluorescence lifetime imaging," Appl. Spectrosc. **55,** 670-678 (2001).

22. T. W. J. Gadella, *FRET and FLIM techniques* (Elsevier Science Ltd, 2008).

23. E. Buurman, R. Sanders, A. Draaijer, H. Gerritsen, J. Van Veen, P. Houpt, and Y. Levine, "Fluorescence lifetime imaging using a confocal laser scanning microscope," Scanning **14,** 155-159 (1992).

24. H. C. Gerritsen, M. Asselbergs, A. Agronskaia, and W. Van Sark, "Fluorescence lifetime imaging in scanning microscopes: acquisition speed, photon economy and lifetime resolution," J. Microsc. **206,** 218-224 (2002).

25. E. W. Weisstein, "Least Squares Fitting--Perpendicular Offsets,".

26. E. Manders, F. Verbeek, and I. Aten, "Measurement of co-localization of objects in dual-colour confocal images," J. Microsc. **169,** 375-375 (1993).

27. M. A. Digman, V. R. Caiolfa, M. Zamai, and E. Gratton, "The phasor approach to fluorescence lifetime imaging analysis," Biophys. J. **94,** L14-L16 (2008).

28. F. S. Wouters and A. Esposito, "Quantitative analysis of fluorescence lifetime imaging made easy," (2008).

3

Spectral phasor analysis allows rapid and reliable unmixing of fluorescence microscopy spectral images

Published in: Optics Express . 20(12), 12729–12741 (2012).

ABSTRACT

A new global analysis algorithm to analyse (hyper-) spectral images is presented. It is based on the phasor representation that has been demonstrated to be very powerful for the analysis of lifetime imaging data. In spectral phasor analysis the fluorescence spectrum of each pixel in the image is Fourier transformed. Next, the real and imaginary components of the first harmonic of the transform are employed as X and Y coordinates in a scatter (spectral phasor) plot. Importantly, the spectral phasor representation allows for rapid (real time) semi-blind spectral unmixing of up to three components in the image. This is demonstrated on slides with fixed cells containing three fluorescent labels. In addition the method is used to analyse auto-fluorescence of cells in a fresh grass blade. It is shown that the spectral phasor approach is compatible with spectral imaging data recorded with a low number of spectral channels.

INTRODUCTION

Fluorescence microscopy is commonly used to study (co)localization of multiple components in biological specimen [1]. These components can be distinguished by their spectroscopic properties, and simultaneously imaged by for instance (hyper) spectral imaging (SI) [2, 3], fluorescence lifetime imaging (FLIM) [4-7], or combinations of these techniques. Fluorescence lifetime imaging is typically employed to image molecular interactions on a nanometre scale by means of monitoring Förster Resonance Energy Transfer (FRET) [8], spectral imaging is the preferred way to study colocalization of multiple fluorophores on a pixel scale. Moreover, identification of endogenous fluorophores in complex biological samples can be performed by spectral imaging [9, 10] and spectral imaging of environment sensitive probes can be used to probe e.g. polarity, pH and Calcium concentration at a subcellular level. The major disadvantage of spectral imaging is that it requires complex analysis algorithms. Emission spectra are often broad and extend into multiple spectral channels. For spectral unmixing, the individual contributions of the fluorescent components to the total signal should be extracted from the data [2, 3]. Linear unmixing can be employed where the recorded spectra are mathematically unmixed using a number of fixed reference spectra of pure components [3]. The reference spectra are usually based on literature data or obtained in separate reference measurements. The use of such reference spectra can easily introduce artefacts because of changes in the spectra caused by solvatochromic shifts or other environmental effects. To correct for these effects, extensive calibration efforts are required.

Therefore, there is great interest in analysis routines that simplify analysis of spectral imaging data. An interesting recent development is the nonnegative matrix factorization algorithm for spectral imaging [11]. In the current work, we investigate the possibility to use phasor analysis for spectral imaging data. Phasor based image analysis has been shown to be very valuable for frequency domain [5, 12-14] and time domain [15] lifetime imaging data. The advantage of these approaches is that they are based on global analysis of the image data and that no (or limited) reference information is required. The spectral phasor analysis method presented here, is based on representing the spectra by phasors (polar representation). The spectra of individual pixels are Fourier transformed and the real and imaginary parts of the first harmonic are employed as coordinates in a phasor scatter plot. In this paper we show that the phasor representation of spectral data affords rapid and reliable unmixing of individual components in the image. To demonstrate the power of this approach, we unmix spectral images of cells stained with three fluorescent probes without the use of reference spectra. In addition, we unmix unknown auto fluorescent components in a grass blade. In the latter case, three autofluorescent components are identified and unmixed without prior knowledge of the autofluorescence composition.

METHODS AND MATERIALS

Instrument details

The nonlinear spectral imaging microscope that is used to record the images is described in a previous paper [9, 10]. Briefly, the excitation light source consists of a mode-locked Titanium: Sapphire (Ti:Sa) laser (Tsunami, Spectra-Physics, Sunnyvale, CA) that tuned to 760 nm. The laser light is scanned in the XY direction using a galvanometer mirror scanner (040EF, LSK, Stallikon, Switzerland). In addition, the microscope is equipped with a Z-piezo objective translation stage (Mad City Labs, Madison, WI, USA) for adjusting the focus position. The laser light is focused on the sample by a microscope objective and the fluorescence emission is collected by the same objective lens. The results reported here are acquired using an infinity-corrected water-immersion objective (CFI Fluor 40xW, NA = 0.8, Nikon, Japan) with a long working distance (2 mm). The emission passes through a dichroic mirror (680 nm short pass) and is filtered by a multiphoton emission filter (FF01-680/SP-25, Semrock, Rochester, NY, USA). The spectrograph consists of a fused silica equilateral dispersive prism (Linos, Göttingen, Germany), a focusing lens (f=90 mm) and an EMCCD camera (Cascade 128+ EMCCD, Photometrics, Tucson, AZ, USA). A low level camera readout script and a customized driver are used for speed optimized camera performance. The images presented here are recorded at room temperature using a pixel dwell time of 128 μs. All raw images have a size of 70x70 μm (unless stated otherwise), 224×224 pixels and contain 128 wavelength channels for each pixel. A background spectrum for each pixel is simultaneously recorded with the emission spectra. The acquisition time for one image amounts to about 6.5 seconds.

Spectral phasor analysis

Spectral phasor analysis bears many similarities with fluorescence lifetime phasor analysis which is a well-known global analysis method for the analysis of fluorescence lifetime images [15]. In spectral phasor analyses, the fluorescence emission spectra of each and every pixel in the image are reduced to a “phasor” that is made up out of two numbers: the real and imaginary parts (amplitude and phase respectively) of the first harmonic of the Fourier transform of the fluorescence spectra. These two numbers are used as coordinates in a scatter plot, the phasor plot. Often, the phasor plots contain clouds of points that correspond to pixels with similar emission spectra. Selected regions in the phasor plot can be remapped to the original fluorescence image, thus providing segmentation based on pixels with similar spectral properties. Fig. 1(a) illustrates how (Gaussian) reference spectra are mapped onto the phasor plot. The grid in the Fig. covers emission maxima over the spectral range 370 – 650 nm, in 10 nm steps and the spectral widths vary from 500 – 4000 cm^{-1} in steps of 500 cm^{-1}. For a fixed spectral width, the positions of the emission maxima lie on an arc; for clarity the wavelengths of the emission maxima are indicated by their colour.One of the advantages of the phasor representation is that it allows for fast, vector based mathematical operations. It enables rapid spectral unmixing, without the need for accurate reference spectra or elaborate fitting procedures.The spectral images can be

represented as a three dimensional data set (X, Y, λ). In our setup, 128 wavelength channels are employed, but the analysis can also be performed on images with a much lower number of spectral channels, see Section 3.4. For each pixel (j) in a spectral image, the measured spectrum is considered to be a linear combination of the spectra of the fluorophores present in the detection volume. This assumption is valid only when the fluorophores are not subject to (interaction) effects such as solvatochromic shifts. The intensity y of a pixel with index j in wavelength channel n is related to the "concentration" X of fluorophore number k by:

$$y_{nj} = \sum_{n} a_{nk} x_{kj}. \qquad (1)$$

where a_{nk} is the fractional contribution to the intensity of spectrum *k* at wavelength channel *n*. For three components Eq. (1) reduces to:

$$y_{nj} = a_{n1} x_{1j} + a_{n2} x_{2j} + a_{n3} x_{3j}. \qquad (2)$$

This is a linear set of equations, where each spectrum (a_{n1}, a_{n2} and a_{n3}) is normalized to one. When the spectra of the individual dyes are known, this linear system can be solved and concentrations of the individual components are obtained. This method, generally referred to as linear unmixing, allows for spectral unmixing of images and yields concentration maps of individual components [2].The number of components that can be unmixed is in principle unlimited but in practice restricted by the signal-to-noise ratio. Alternatively, unmixing can be achieved by fitting the spectrum with e.g. multiple Gaussian functions that resemble the spectra of the fluorescent components. After multiple iterations, the contributions of the individual components are obtained [16]. Spectral phasor analysis enables straight-forward unmixing of a mixture of three spectra. Consider the Fourier transformation of the spectrum *Yj*:

$$Y_j = \frac{A_1 x_{1j} + A_2 x_{2j} + A_3 x_{3j}}{x_{1j} + x_{2j} + x_{3j}} = \alpha_1 A_1 + \alpha_2 A_2 + \alpha_3 A_3. \qquad (3)$$

With A_k the discrete Fourier transform of a_k at the first harmonic (the phasors of the spectra):

$$A_k = \sum_{n=1}^{N} a_{nk} e^{-i\frac{2\pi}{N}n}. \qquad (4)$$

here *N* is the number of spectral channels and α_k the fractional intensity of component *k* which is defined as:

$$\alpha_k = \frac{x_k}{x_1 + x_2 + x_3}, \qquad (5)$$

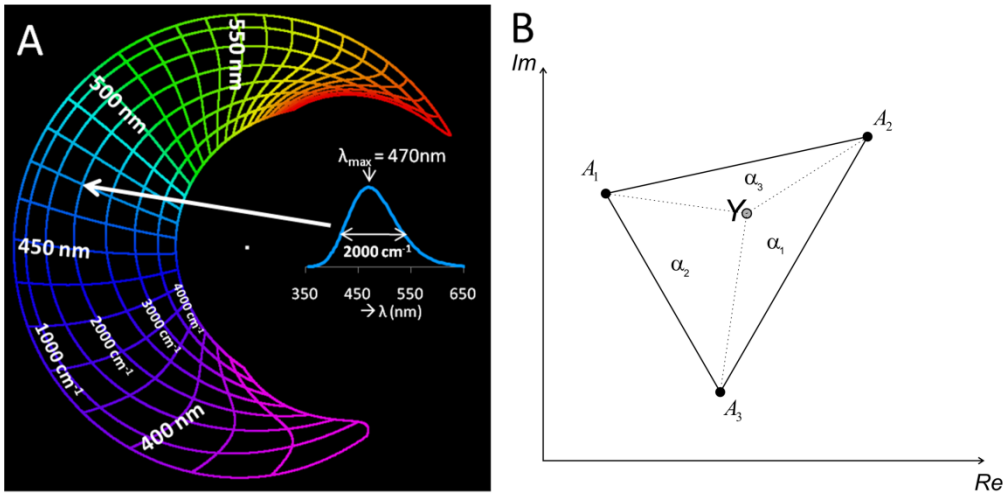

Fig.1 (A) Reference spectral phasor plot showing the positions of Gaussian spectra. The grid covers emission maxima from 370 – 650 nm (the wavelength determines the position on the semicircle, as indicated by its colour) and spectral widths from 500 – 4000 cm^{-1} (with increasing spectral width, the position in the phasor plot is shifted towards the centre of the circle). As an example, a spectrum and its position in the phasor are shown. (B) The relative intensities α_1, α_2 and α_3 of components A_1, A_2 and A_3 in a pixel can be derived from the phasor.

We note that normalization requires that $\alpha_1+\alpha_2+\alpha_3=1$. Therefore α_3 can be replaced by 1 - (α_1 + α_2) resulting in:

$$Y_j = \alpha_1 A_1 + \alpha_2 A_2 + (1-(\alpha_1+\alpha_2))A_3. \qquad (6)$$

The real and imaginary parts of *Yj* can be written as:

$$\begin{aligned} \mathrm{Re}\,Y_j &= \alpha_1 \mathrm{Re}\,A_1 + \alpha_2 \mathrm{Re}\,A_2 + (1-(\alpha_1+\alpha_2))\mathrm{Re}\,A_3, \\ \mathrm{Im}\,Y_j &= \alpha_1 \mathrm{Im}\,A_1 + \alpha_2 \mathrm{Im}\,A_2 + (1-(\alpha_1+\alpha_2))\mathrm{Im}\,A_3, \end{aligned} \qquad (7)$$

Solving α_1 and α_2 results in:

$$\alpha_1 = \frac{\mathrm{Re}\,A_2\,\mathrm{Im}\,Y - \mathrm{Re}\,Y\,\mathrm{Im}\,A_2 + \mathrm{Re}\,A_3\,\mathrm{Im}\,A_2 - \mathrm{Re}\,A_2\,\mathrm{Im}\,A_3 + \mathrm{Re}\,Y\,\mathrm{Im}\,A_3 - \mathrm{Re}\,A_3\,\mathrm{Im}\,Y}{\mathrm{Re}\,A_2\,\mathrm{Im}\,A_1 - \mathrm{Re}\,A_1\,\mathrm{Im}\,A_2 - \mathrm{Re}\,A_3\,\mathrm{Im}\,A_2 - \mathrm{Re}\,A_2\,\mathrm{Im}\,A_3 + \mathrm{Re}\,A_1\,\mathrm{Im}\,A_3 - \mathrm{Re}\,A_3\,\mathrm{Im}\,A_1},$$

$$\alpha_2 = \frac{\mathrm{Re}\,A_3\,\mathrm{Im}\,Y - \mathrm{Re}\,Y\,\mathrm{Im}\,A_3 + \mathrm{Re}\,A_1\,\mathrm{Im}\,A_3 - \mathrm{Re}\,A_3\,\mathrm{Im}\,A_1 + \mathrm{Re}\,Y\,\mathrm{Im}\,A_1 - \mathrm{Re}\,A_1\,\mathrm{Im}\,Y}{\mathrm{Re}\,A_2\,\mathrm{Im}\,A_1 - \mathrm{Re}\,A_1\,\mathrm{Im}\,A_2 - \mathrm{Re}\,A_3\,\mathrm{Im}\,A_2 - \mathrm{Re}\,A_2\,\mathrm{Im}\,A_3 + \mathrm{Re}\,A_1\,\mathrm{Im}\,A_3 - \mathrm{Re}\,A_3\,\mathrm{Im}\,A_1}. \qquad (8)$$

with α_3 = 1-(α_1 + α_2).

Plotting the phasors (imaginary versus real part) of A_k for k=1, 2, 3, results in a triangle in the phasor plot with vertices at A_1, A_2 and A_3 (Fig.1(b)). The phasor of a spectrum consisting of a linear combination of three pure components falls inside this triangle and the fractional intensities of the components are given by Eq. 8. Closer examination of Eq. 8 shows that α_1, the fractional intensity of component A_1, is equal to the area of the triangle

formed by the phasor position in the phasor plot (indicated by Y in Fig.1(b)) and the two reference points A_2 and A_3 divided by the area of the reference triangle (A_1, A_2, A_3). To illustrate this consider two extreme cases: (1) when the measured point coincides with A_1, α_1 occupies the whole reference triangle and is therefore equal to one, and (2) when the measured point lies on the line connecting A_2 and A_3, α_1 will be zero. The fractional intensities of the other components are obtained in a similar way. We note that images of the unmixed intensities of individual components k are obtained by multiplying the α_k image with the (mixed) total intensity image.

Sample details

10 µM aqueous solutions were prepared from the fluorescent dyes Coumarin 120 (Sigma-Aldrich A9891), Rose Bengal (Sigma-Aldrich R3877) and Fluorescein (Sigma-Aldrich F6377). FluoCells prepared slide #2 (Invitrogen F-14781) contains bovine pulmonary artery endothelial cells (BPAEC). Texas Red-X phalloidin is labelling the F-actin, anti—bovine α-tubulin mouse monoclonal antibody in conjunction with BODIPY FL goat anti—mouse IgG antibody is labelling microtubules, and DAPI is labelling the nucleus. FluoCells prepared slide #6 (Invitrogen F-35925) contains fixed, permeabilized, and labelled muntjac skin fibroblast cells. Mitochondria are labelled with mouse anti–OxPhos Complex V inhibitor protein antibody and visualized using orange-fluorescent Alexa Fluor 555 goat anti–mouse IgG antibody. F-actin is labelled with green-fluorescent Alexa Fluor 488 phalloidin, and the nucleus is stained with TO-PRO-3 iodide. The grass blade sample was freshly picked near the laboratory and put in water to match the refractive index of the objective.

RESULTS

Spectral phasor analysis of dye solutions

To demonstrate and explain the capability of spectral phasor analysis for segmenting fluorescence images, spectral images of three aqueous fluorescent dye solutions (Coumarin 120, Rose Bengal and Fluorescein are recorded and analysed, see Figs.2(a-c). The colour of the pixels in the phasor plot corresponds to the colour of fluorescence emission in that pixel as perceived by eye (real colour visualization [16]). For reference purposes a semicircle of theoretical Gaussian emission spectra with maxima ranging from λ_{em} = 370 to 650 nm and width $\Delta\lambda$ = 250 cm^{-1} is shown in the phasor plot. For images of solutions containing only a single dye, the positions of the phasors in the phasor plot are well localized; see the clouds of points in Figs.2 (a-c). Examples of single-pixel spectra (coloured curves) from arbitrarily chosen pixels, as well as spectra averaged over the whole image (white curves), are shown in the phasor plots. In typical imaging experiments, tens to hundreds of dye molecules are present in the focus of the microscope which results in noisy single pixel emission spectra. For the images used in Figs.2(a-c), we estimate that several hundred photons are detected per spectrum per pixel. For this signal level, the signal-to-noise ratio (S/N) at the emission maximum is approximately three. The size of the phasor cloud in Figs.2(a-c) is determined by photon statistics and amounts to

approximately 10-20 nm by 500-1000 cm^{-1}, which suggests that this signal level is sufficient to segment two components with a either a difference in emission maximum of >20 nm or a difference in spectral width of >1000 cm^{-1}. The size of the phasor cloud is reduced when spectral images are binned. The effect of binning 3x3 pixels (N=9) is shown for Fluorescein in Fig.2 (d).

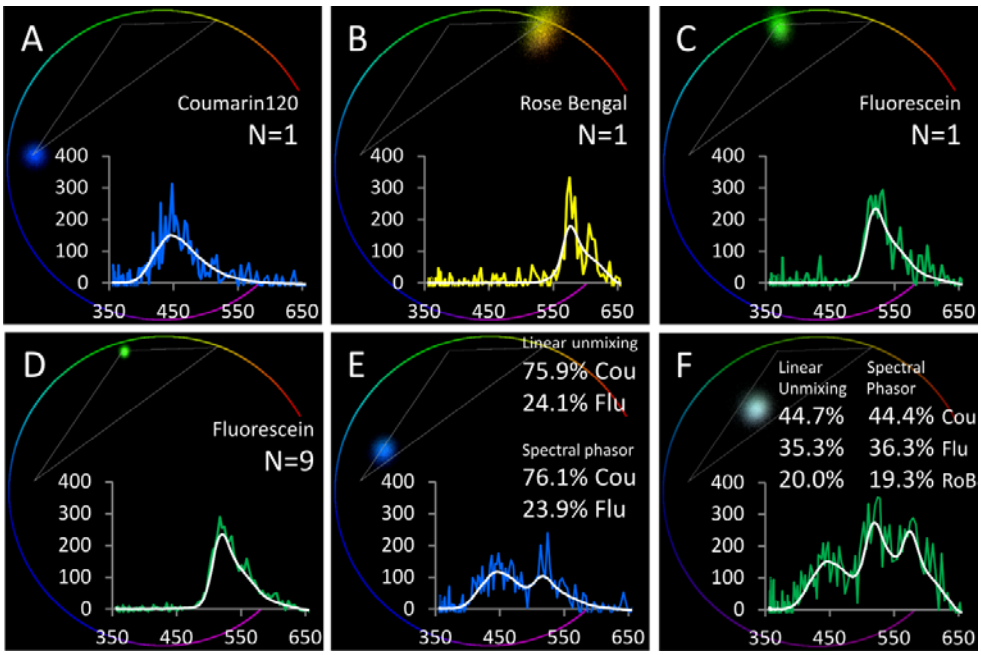

Fig.2 Spectral phasor analysis of solutions of organic dyes Coumarin 120 (A), Rosebengal (B) and Fluorescein (C-D), mixtures of Coumarin 120 and Fluorescein, and a mixture of Coumarin 120 , Fluorescein and Rosebengal (F). In each phasor diagram also the average spectrum over the whole image (white line) and of a single pixel is displayed (coloured line). A reference semicircle of Gaussian spectra (370-650 nm, 500 cm^{-1}) and a grey triangle connecting the reference positions of the dyes are indicated in each phasor diagram. We note that positions in the phasor plot are colour coded according to their real RGB colour.

Binning results in a narrower distribution of the phasor points; here the size of the phasor cloud is reduced to ~5 nm by ~500 cm^{-1}. The higher signal level clearly affords separating smaller spectral differences.

The spectral phasor approach enables convenient spectral unmixing of mixtures of fluorophores based on Eq. 8. This is exemplified in Figs.2 (e-f), where phasors of (homogeneous) mixtures of Coumarin 120 and Fluorescein (E) and of Coumarin 120, Fluorescein and Rose Bengal (F) are shown. Conventional linear unmixing of the average spectrum of the Coumarin and Fluorescein image results in relative contributions of 75.9% and 24.1%, respectively. This is in excellent agreement with the phasor unmixing results of 76.1% and 23.9% (Fig.2(e)). The results for the unmixing of the mixture of Coumarin 120,

Fluorescein and Rose Bengal are again in excellent agreement. Linear unmixing yields relative contributions of 44.7%, 35.3% and 20%, respectively; spectral phasor unmixing yields contributions of 44.4%, 36.3% and 19.3%, respectively.

Spectral phasor based unmixing of labeled cells

To further evaluate the capability of spectral phasor analysis to unmix spectral images, we analysed spectral images of Molecular Porbe FluoCells test slide #2 and #6. The fluorescent dyes in these specimens can be simultaneously excited by two-photon excitation at 790 nm. Fig.3 summarizes the phasor analysis of a single cell on the test slide#2. In Fig.3(b) the "real colour RGB" fluorescence image [16] of the cell is shown. Fig.3(a) shows the phasor plot of the cell. For unmixing, reference phasor positions should be identified to construct the triangle discussed in Fig.2(b). Ideally, reference phasors are obtained from areas in the specimen that contain only a single fluorescent component. Such references may be found at the edges of the phasor distribution. To verify whether these edges indeed correspond to "pure" components, the spectra from the selected areas in the phasor diagram (indicated by the dashed boxed areas) are shown in Fig.3(a). The spectra are clearly not pure, but do reveal clear emission maxima from the three dyes. The spectra in Fig.3(a) reveal that there are pixels that contain only Texas Red or DAPI but pixels containing BODIPY (white box) always contain a significant contribution of Texas Red. Consequently, the phasor cloud does not extend to the BODIPY reference point. Therefore, in Fig.3(a) phasor reference *curves* are added for each dye. The curves are constructed using Gaussian shaped emission spectra with the experimentally determined maximum emission wavelengths of the dyes (DAPI λ_{em} = 460 nm, BODIPY λ_{em} = 525 nm and Texas Red λ_{em} = 615 nm) and a spectral width that varies between 250 and 3000 cm^{-1}. The reference points can now be estimated by extrapolating the phasor clouds to the three reference curves. Spectral unmixing based on these reference phasors yields excellent results on this test specimen. The signal of DAPI (nucleus) is accurately separated from the Texas Red (actin) and BODIPY (tubulin) signals; also the latter two are remarkably well unmixed with no detectable bleed through, see Figs.3(c-e) sample 1. The same approach is applied to the test slide #6. The emission maxima for Alexa 488, Alexa 555 and TO-PRO-3 are again derived from selected areas in the phasor diagram. Next, the three reference curves are drawn for these maxima. Again clear segmentation without bleeding through of actin, mitochondria and nucleus is achieved (Figs. 4(c-e)).The images of Figs. 3 and 4 are also analysed using the Nonnegative Matrix Factorization algorithm introduced by Neher *et al* [11]. Independent of their 'segregation bias' some spectral bleed through is observed. Input of approximate reference spectra is required to correctly unmix the image with minimal bleed through (not shown).

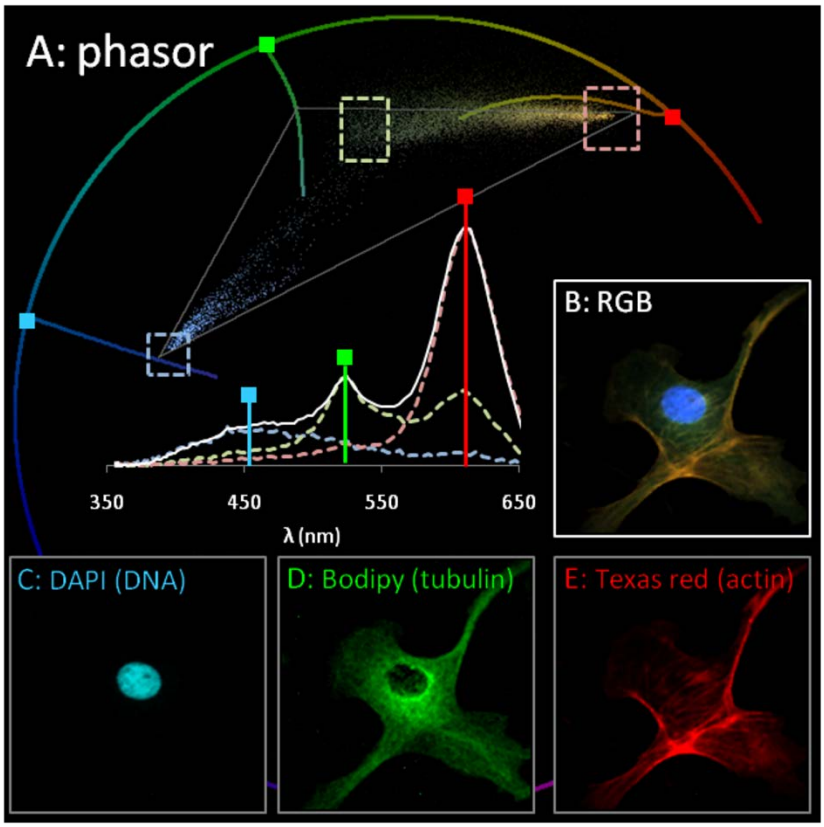

Fig.3 Spectral phasor analysis of FluoCells test slides #2 (field of view 80x80μm) A) Spectral phasor plot; for three areas in the phasor plot (indicated by the dashed boxes), the spectra are averaged and displayed together with the average spectrum of the whole image. A solid reference semicircle (370-650 nm, 500 cm^{-1}) and three solid reference lines corresponding to the positions of the emission maxima found from the spectra are shown in the phasor plot. B) Real colour representation of the original image. C-E) Unmixed images of DAPI, BODIPY and Texas Red.

Unmixing of autofluorescence in grass blade

The analysis of specimens containing endogenous (autofluorescent) fluorophores can be challenging, especially when their origin and spectral characteristics are not known. To exemplify the analysis of an unknown biological specimen, a multiphoton spectral image of the autofluorescence of a randomly picked grass blade is analysed. The spectral phasor plot and RGB fluorescence image of the grass blade are shown in Figs.5(a-b). The blue/green fluorescence mainly originates from hydroxycinnamic acids and/or flavonoids [17, 18], whereas the red emission is mainly from chlorophylls [19]. The distribution of the points in the phasor plot is triangularly shaped and the average spectra near the edges of the triangle (taken from the areas indicated by the dashed squares) reveal that the blue and red components have their main emission maxima at 470 nm and 635 nm respectively. The main peak of the green emission is at 495 nm, but a strong second peak is also observed at approximately the same wavelength as the red emission. Clearly, the image does not

contain pixels that contain pure green emission. For the spectral unmixing of this specimen, reference phasors lines corresponding to the locations of the emission maxima (λ_{em} = 470 nm for the blue, λ_{em} = 495 nm for the green and λ_{em} = 635 nm for the red component) and a range of spectral widths (from 250 and 3000 cm^{-1}) are drawn into the phasor plot.

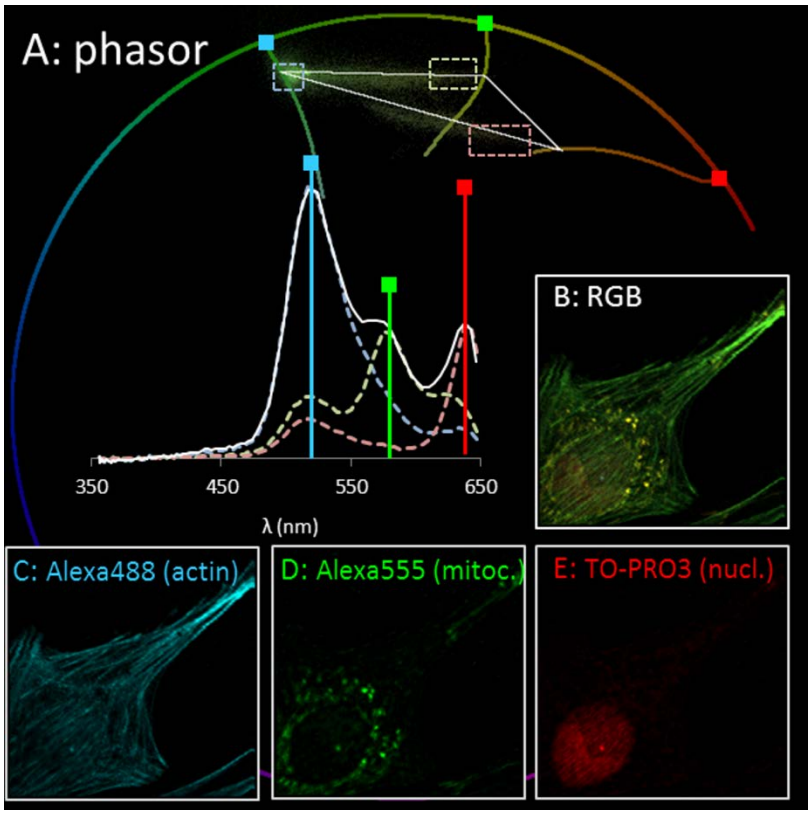

Fig. 4 Spectral phasor analysis of FluoCells test slides #6 (field of view 50x50µm); A) Spectral phasor plot; for three areas in the phasor plot (indicated by the dashed boxes), the spectra are averaged and displayed together with the average spectrum of the whole image. A solid reference semicircle (370-650 nm, 500 cm^{-1}) and three solid reference lines corresponding to the positions of the emission maxima found from the spectra are shown in the phasor plot. B) Real colour representation of the original image. C-E) Unmixed images of Alexa 488, Alexa 555 and TO-PRO3.

The edges of the solid triangle in Fig.5(a) are found by extrapolating the phasor clouds manually. Figs.5(c-e) shows the spectrally unmixed components of the grass blade. Again the spectrally unmixed images are of good quality and no obvious bleed through is observed between the different components.

Compatibility of spectral phasor analysis with other (hyper-) spectral imaging systems

The spectral images employed in the above examples were recorded using a spectrograph with 128 wavelength channels per pixel. This system has a sufficiently high spectral resolution to determine the emission maxima and spectral widths.

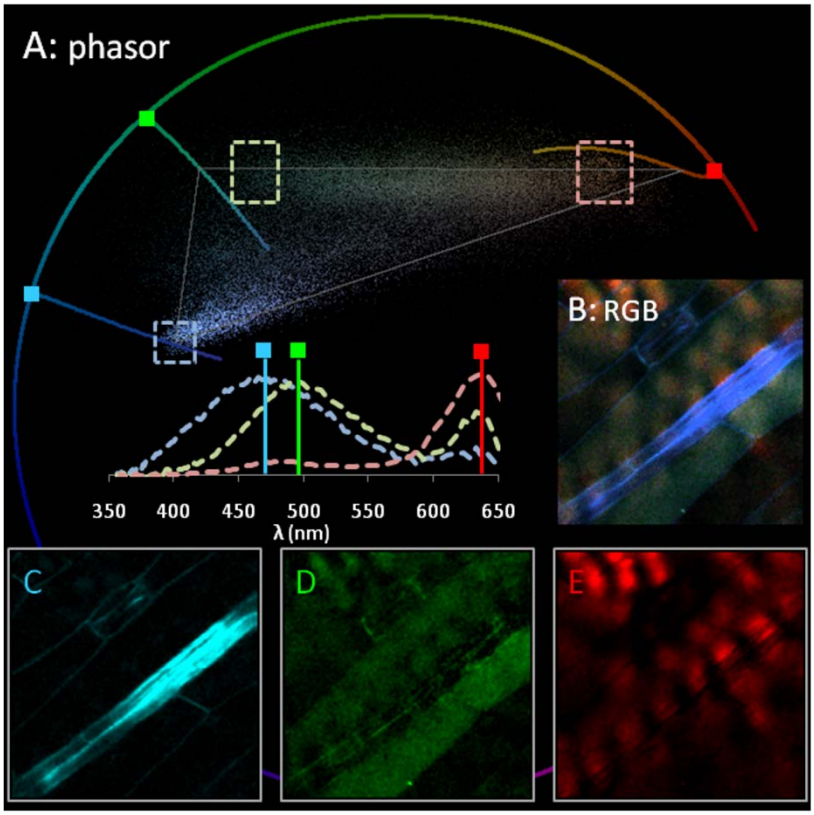

Fig. 5. Spectral phasor plot of a Grass blade autofluorescence image. For three areas in the phasor plot, the spectra are averaged and displayed (indicated by dashed boxes and spectra) together with the average spectrum of the whole image. A solid reference semicircle of Gaussian spectra (370-650 nm, 500 cm^{-1}) and three solid reference lines of the positions of emission maxima found in the spectra (470 nm, 495 nm and 630 nm) are also shown. The grey triangle connects the reference positions of the dyes, allowing unmixing of the image in the three channels. B) The real colour representation of the autofluorescence image. C-E) The unmixed signals.

Most commercial spectral imaging systems are based on (multi-anode) photo multiplier tubes. Typically, they are equipped with a 32, 16, 8 or 4 detection channels. To investigate the effect of the number of spectral channels on phasor based segmentation we calculated phasor plots of Gaussian reference spectra for imaging systems with 16, 8 and 4 detection channels (see Figs.6(a),(b),(c)). The raster patterns in Fig.6 correspond to emission wavelength steps of 10 nm and spectral width steps of 500 cm^{-1} (similar to Fig.1(a)). At 16 channels the raster pattern is unaffected by the reduction of the number of channels; at 8 channels, however, the pattern is distorted in particular for narrow spectra (<1000 cm^{-1}).

For 4 channels the distortion of the pattern is even more severe. Next, the spectral image shown in Fig.3 is re-binned to 4, 8 and 16 spectral channels (linear with wavelength) and represented in spectral phasor plots (see Figs.6(a),(b),(c)). Interestingly, the spectral unmixing is not affected by the reduction in the number of spectral channels. To quantify the similarity between the spectrally unmixed images, Manders overlap coefficients are calculated [20]. The value of this coefficient ranges from 0 to 1, with 1 indicating perfect overlap and zero indicating no overlap of the two images. For convenience the three unmixed images are stitched together to be able to calculate a single Manders coefficient per set of unmixed images. Next, the Manders coefficients for 128, 16, 8 and 4 channel unmixing are calculated.

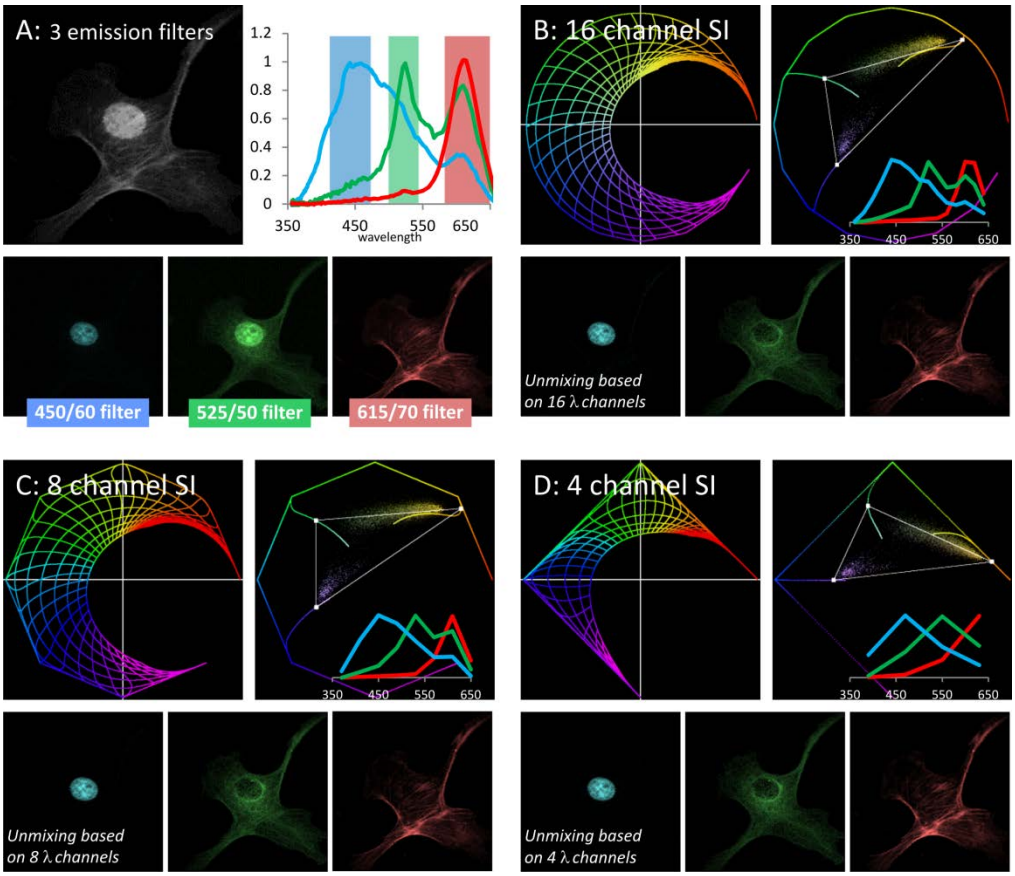

Fig. 6. Spectral analysis of the BPAE cells shown in Fig.3. (A) Images corresponding to 3 emission filters (top) and total intensity (bottom). (B-D) Spectral phasor diagrams of spectral images with 16, 8 and 4 wavelength channels respectively. The reference phasor grids (top left) cover emission maxima from 370 – 650 nm and spectral widths from 500 – 4000 cm^{-1}. Spectra of regions at the edges of the phasor cloud are included.

Here, the 128 channel value (original Fig. 3) serves as a reference. In all cases the Manders coefficient is between 0.97 and 0.98, indicating almost perfect overlap. For comparison, images corresponding to three spectrally filtered emission windows (420-480nm for DAPI, 500-550nm for BODIPY and 580-650 for Texas Red) are constructed from the 128 channel

spectral data (see Fig.6 (d)). In this case (no unmixing), strong bleed through of DAPI into the green channel is observed. When comparing these images (again stitched) to the 128 channel phasor unmixing result the overlap is considerably reduced, the Manders coefficient amounts to 0.87.

At 4 wavelength channels, the phasor based spectral unmixing requires prior knowledge of the emission maxima of the dyes. Here, the low spectral resolution does not allow establishing the positions of the emission maxima. Consequently it is not possible to construct reference phasor lines for the emission maxima. At least 8 channels are required to obtain sufficient information to construct the reference phasor lines.

DISCUSSION

In this work, it is demonstrated that phasor analysis can be applied to spectral imaging data. Here, similar to phasor analysis of time-domain lifetime imaging, the Fourier transform representation is used for visualization and analysis of the image data. Fourier transformation results in a spectrum of harmonics and the phasor plots are constructed by employing the real and imaginary components of the first harmonic of the transform as X and Y coordinates in a scatter plot. Spectral phasor analysis is a fast and photon efficient way to extract two characteristic numbers from a spectrum that are related to the maximum wavelength and width of the spectrum. In principle also the higher harmonics can be employed to construct phasor plots. However, the first harmonic has the highest amplitude and is therefore least sensitive to noise. Closer examination of Eq.7 reveals that it is not possible to unmix more than 3 components. A sample with 4 components requires estimating 3 unknown parameters (α_1, α_2 *and* α_3) while the number of equations is limited to two. Including the additional information that the higher order harmonics provide might enable the unmixing of more than three components. This is possible due to the orthogonality of the Fourier components which allows adding additional dimensions to the phasor plot and extending it into a 3D histogram. However, analysis of this 3D cloud is not trivial. The development of an algorithm that automatically finds the reference points is under consideration.

In the phasor unmixing we employ Gaussian reference curves generated by varying the widths of Gaussian shaped spectra. These curves serve as guidelines to assign the reference points for samples where the vertices of the phasor plot are not clearly visible. Assuming a different shape for the reference spectra introduces a small shift in the positions of the reference curves. However, in our experience the choice of the reference points is not very critical; variations of the reference points have only small effects on the accuracy of the unmixing.

The spectral phasor offers similar capabilities for image analyses as the lifetime phasor [14], but now based on spectral properties. Phasor plots can be employed for segmentation since image pixels mapped onto the same position in the phasor plot have

similar widths and maximum wavelengths [21]. Images can be unmixed and in addition information is available about the heterogeneity in the pixel composition. Spectral phasor analysis does not require extensive calibration. In this work the Fourier transformation is carried out on un-calibrated spectra. The spectral range of 350 to 700 nm is detected by a 128 channel spectrograph. Because of the nonlinear dispersion of the prism, the channel numbers are not linear with wavelength (from ~2 nm/pixel at 400 nm to ~5 nm/pixel at 700 nm). On a wavenumber scale (energy), the scale is close to linear in the visible range (100-120 cm^{-1}/pixel). Moreover, at 655 nm the emission is cut off by an emission filter. All these factors influence the position of the measured spectrum in the phasor plot. Clearly, the use of other spectral detectors and microscopes will affect the phasor plot. This can be avoided by calibration of the wavelength scale and response of the spectral imaging system. There are several other unmixing methods that can be employed to separate the components in spectral images. Linear unmixing is the most common technique, it is straightforward and software is readily available. Importantly, linear unmixing requires accurate reference spectra of the individual components which is not straight-forward. Emission spectra often depend on the local environment of the dyes; the spectra in cells may very well differ from those in solution. This compromises the accuracy of linear unmixing. Several blind unmixing approaches were introduced to overcome these difficulties such as PARAFAC [22], principle component analyses (PCA) [23] and non-negative matrix factorization (NMF) [11]. PARAFAC is complicated by the fact that both excitation and emission spectra need to be measured. This makes the method fairly complicated and impractical for fluorescence microscopy. PCA is mathematically complicated and reveals the internal structure of the data in a way which best explains the variance in the data. One of the complications with this method is that it is sensitive to round-off errors and that noise in the images may result in negative contributions of components. These problems were mitigated in the NMF method which has been demonstrated to yield good results on spectral images of fluorescent cells with up to 4 labels. However, the NMF needs to be fed with approximate reference spectra that are modified during the unmixing procedure. Unfortunately, the unmixing result does depend on the initial value of the start spectra. The spectral phasor approach also requires reference values, but the phasor plot itself can provide these reference values. The phasor plot allows determination of the peak positions of the fluorescent molecules in their native environment. The results show improved unmixing results compared to linear and NMF based unmixing.

The most important advantage of the spectral phasor based unmixing compared to other approaches is that it is fast, robust and that reference phasors can be derived from the phasor plot. Creating a phasor plot of a 256x256 pixel image with 128 spectral channels takes about one second on a standard PC, much faster than the NMF method. However, so far no more than three components can be unmixed with the spectral phasor approach. We note that the time required calculating the phasor plot is significantly reduced for lower numbers of spectral channels. One of the interesting features of the phasor

approach is that areas selected in the phasor plot can be mapped back to the image to realize segmentation based on spectral differences. In this way (many) more than 3 'components' can be separated. Phasor based unmixing relies at present on the manual assignment of the positions of the reference points in the phasor plot. Nevertheless, it is easy to check whether suitable reference points have been chosen by determining the emission maxima of average spectra of selected regions in the vicinity of the anticipated reference point. Overall, spectral phasor analysis is a method to unmix spectral images with minimal input, and the input that is required can be obtained from the spectral image itself. The most important prerequisite is that the fluorescent dyes have emission maxima that can be extracted from the average spectrum of (part of) the image. For fluorescent labels, this is often the case, especially when the number of spectral channels is large. The examples in this paper show the power of the spectral phasor method: it facilitates rapid separation of the fluorescence components in images. Since it can be applied to most spectral imaging data, we believe that spectral phasor analysis is valuable tool for the analysis of spectral images.

An ImageJ plugin for spectral phasor analyses is available from the author's web site: http://www.Spechron.com/

REFERENCES

1. J. Pawley, ed., Handbook of Biological Confocal Microscopy (Springer, 2006).

2. T. Zimmermann, J. Rietdorf, and R. Pepperkok, “Spectral imaging and its applications in live cell microscopy, ” FEBS Lett. **546,** 87-92 (2003).

3. Y. Garini, I. T. Young, and G. McNamara, “Spectral imaging: Principles and applications, ” Cytometry Part A **69,** 735-747 (2006).

4. H. C. Gerritsen, A. V. Agronskaia, A. N. Bader, and A. Esposito, “Time domain FLIM: Theory, instrumentation, and data analysis, ” in FRET and FLIM techniques, T. W. J. Gadella, ed. (Elsevier, 2009), 95-132.

5. P. J. Verveer and Q. S. Hanley, “Frequency domain FLIM theory, instrumentation, and data analysis, ” in FRET and FLIM Techniques, T. W. J. Gadella, ed. (Elsevier, 2009), 59-94.

6. P. I. H. Bastiaens and A. Squire, “Fluorescence lifetime imaging microscopy: Spatial resolution of biochemical processes in the cell, ” Trends Cell Biol. **9,** 48-52 (1999).

7. J. Willem Borst and A. J. W. G. Visser, “Fluorescence lifetime imaging microscopy in life sciences, ” Measurement Science and Technology **21,** (2010).

8. V. E. Centonze, M. Sun, A. Masuda, H. Gerritsen, and B. Herman, “Fluorescence resonance energy transfer imaging microscopy, ” Methods in Enzymology **360,** 542-560 (2003).

9. A. N. Bader, A. M. Pena, C. J. Van Voskuilen, J. A. Palero, F. Leroy, A. Colonna, and H. C. Gerritsen, “Fast nonlinear spectral microscopy of in vivo human skin, ” Biomed. Opt. Express **2,** 365-373 (2011).

10. J. A. Palero, G. Latouche, H. S. de Bruijn, van der Ploeg van den Heuvel,A., H. J. Sterenborg, and H. C. Gerritsen, “Design and implementation of a sensitive high-resolution nonlinear spectral imaging microscope, ” Journal of biomedical optics **13,** 044019 (2008).

11. R. A. Neher, M. Mitkovski, F. Kirchhoff, E. Neher, F. J. Theis, and A. Zeug, “Blind source separation techniques for the decomposition of multiply labeled fluorescence images, ” Biophys. J. **96,** 3791-3800 (2009).

12. D. M. Jameson, E. Gratton, and R. Hall, “The measurement and analysis of heterogeneous emissions by multi frequency phase and modulation fluorometry, ” Appl. Spectrosc. Rev **20,** 55-106 (1984).

13. P. J. Verveer, A. Squire, and P. I. H. Bastiaens, “Global analysis of fluorescence lifetime imaging microscopy data, ” Biophys. J. **78,** 2127-2137 (2000).

14. G. I. Redford and R. M. Clegg, “Polar plot representation for frequency-domain analysis of fluorescence lifetimes, ” J. Fluoresc. **15,** 805-815 (2005).

15. M. A. Digman, V. R. Caiolfa, M. Zamai, and E. Gratton, “The phasor approach to fluorescence lifetime imaging analysis, ” Biophys. J. **94,** L14-L16 (2008).

16. J. A. Palero, H. S. De Bruijn, Van Der Ploeg-Van Den Heuvel,A., H. J. C. M. Sterenborg, and H. C. Gerritsen, “In vivo nonlinear spectral imaging in mouse skin, ” Optics Express **14,** 4395-4402 (2006).

17. C. Buschmann and H. K. Lichtenthaler, “Principles and characteristics of multi-colour fluorescence imaging of plants, ” J. Plant Physiol. **152,** 297-314 (1998).

18. S. Meyer, A. Cartelat, I. Moya, and Z. G. Cerovic, “UV-induced blue-green and far-red fluorescence along wheat leaves: A potential signature of leaf ageing, ” J. Exp. Bot. **54,** 757-769 (2003).

19. R. Cisek, L. Spencer, N. Prent, D. Zigmantas, G. S. Espie, and V. Barzda, “Optical microscopy in photosynthesis, ” Photosynthesis Res. **102,** 111-141 (2009).

20. E. M. M. Manders, F. J. Verbeek, and J. A. Aten, “Measurement of co-localization of objects in dual-colour confocal images, ” J. Microsc. **169,** 375-382 (1993).

21. F. Fereidouni, A. Esposito, G. A. Blab, and H. C. Gerritsen, “A modified phasor approach for analyzing time-gated fluorescence lifetime images, ” J. Microsc. **244,** 248-258 (2011).

22. H. Shirakawa and S. Miyazaki, “Blind Spectral Decomposition of Single-Cell Fluorescence by Parallel Factor Analysis," Biophys. J. **86,** 1739-1752 (2004).

23. I. T. Jolliffe, Principle Component Analysis (Springer Verlag, 1986).

4

Phasor analysis of multiphoton spectral images distinguishes autofluorescence components of in vivo human skin

Submitted to: Journal of Biophotonics .

ABSTRACT

Autofluorescence images of skin contain contributions from many different components. Using spectral imaging this rich information content can be unveiled. However, detailed analysis is complicated by the overlap of emission bands and the comparatively low signal levels. Here, a spectral phasor method is employed to analyze two photon excited autofluorescence and second harmonic generation in *in vivo* human skin images. This method allows segmentation of images based on spectral features as well as unmixing of the autofluorescent components. Various structures in the skin could be distinguished, including Stratum Corneum, epidermal cells and dermis. The spectral phasor analyses allowed investigation of their fluorescence composition and can identify signals from NADH, keratin, FAD, melanin, collagen and elastin. Interestingly, two populations of epidermal cells could be distinguished with different melanin content.

INTRODUCTION

Multiphoton microscopy/tomography is a powerful tool to study biological tissues[1, 2]. The near infrared excitation light affords in-depth imaging of the specimen with minimal photo damage. Moreover, it can be conveniently used to excite autofluorescence (AF) and generate scattering signals such as second harmonic generation (SHG)[3-6]. Autofluorescence imaging is particularly interesting for biomedical applications, including in vivo imaging of (human) skin, because no exogenous fluorophores are required. This technology is now being applied both in clinics and industry to, for instance, diagnose diseased tissue[1, 7, 8] and for the testing of cosmetic products without the need for sacrificing test animals[9].

The contrast in multiphoton images is typically provided by differences in the intensity of AF and SHG signals. Discrimination between various structures in skin therefore mainly relies on differences in morphology and intensity. More detailed information can be obtained by utilizing the spectroscopic properties of the emission. For instance, fluorescence lifetime imaging[4, 8] and spectral imaging[3, 10] yield additional information that allows in depth analyses of the specimen.

Detailed analysis of autofluorescence spectral images, in particular identifying and segmenting different fluorescent components, can be challenging and requires significant effort. Moreover, autofluorescence images often suffer from poor signal-to-noise ratio which makes analyses even more challenging. We note that in in vivo imaging the maximum number of photons that can be detected is limited by the maximum allowed excitation power and exposure time[3]. Furthermore, reference spectra may not be available, or may be susceptible to the micro environment[11]. In some cases, the emission spectra almost completely overlap which further complicates analyses. For instance, the emission maxima of free and bound NADH are separated by only 20 nm[12]. In this reference this complication was overcome by fitting the spectrum in each pixel with Gaussian approximations of the reference spectra; a common approach in spectral imaging/unmixing[13].

Here, we simplify and improve the analysis of complex spectral images of tissue by employing the recently introduced spectral phasor analysis method[14]. Image stacks of in vivo human epidermis and upper dermis of the skin of a tanned male volunteer (Caucasian skin type) were recorded that contain AF signals of Stratum Corneum, epidermal cells, melanized epidermal cells and SHG of dermal collagen fibers. It is shown that spectral phasor analysis (1) enables segmentation of these structures, (2) allows identification of the fluorescent components including NADH, keratin, FAD, melanin, collagen and elastin, (3) can spectrally unmix the (3D) images.

METHODS

Spectral phasor analysis

Spectral phasor analysis was carried out using a homemade ImageJ plugin (available from http://www.spechron.com). The phasor approach has previously been implemented to analyze lifetime[15, 16] and spectral images[14]. It provides a fast, reliable and easy way to analyze the images using a graphical approach that requires only little computational power.

In spectral phasor analyses the spectra are Fourier transformed, next the real and imaginary parts serve as coordinates in a 2D histogram. In this histogram, referred to as phasor plot, pixels are mapped onto a position that is related to their spectral shape and peak position. A basic demonstration of the approach is shown in the Fig. 1A. Here, the phasors of Gaussian spectra with different maximum emission wavelength λmax and spectral width Δλ are shown. In this case, the spectral images contain 128 spectral channels, but different numbers of spectral channels can be used as well[14]. By changing λmax of a Gaussian spectrum from red to blue, which corresponds to moving from channel 0 to 127, the phasor moves along the semicircle from top to the bottom. This is explained by the shift theorem of Fourier transformation, where a shift in a function is represented by a rotation in Fourier space. By increasing the width of the spectrum the phasor moves toward the center; it is approaching the phasor for a flat background signal which is located at the centre of the phasor plot. In Fig. 1a spectral widths, Δλ , of 1, 10 and 20 spectral channels are shown. The deviations from a semicircle at the ends of the phasor curves are due to truncation of the spectra at the edges of the spectral window.

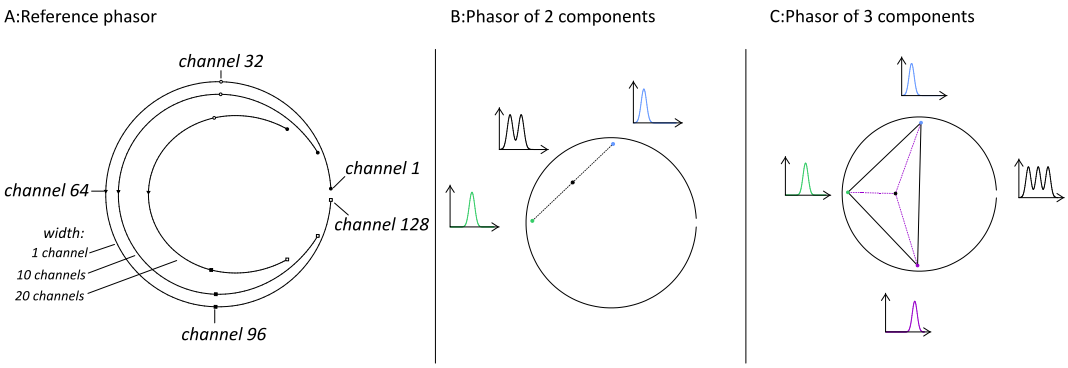

Fig.1 (a) The spectral phasor plot for Gaussian spectra with different maximum emission wavelengths and spectral widths. The phasor moves along the semicircle as the emission maximum moves from first to last spectral channel. The radius of the semi-circle shrinks when the spectral width goes up. (b) Phasors are additive; the phasor of a binary system can be found from the sum of the individual components and their amplitudes. (c) The total phasor of a 3 component system.

An important property of the phasor approach is the way mixtures of spectra appear in the phasor plot. A phasor of a mixture of two spectra falls on a line connecting the two individual phasors (Fig. 1b). The distance from the resultant phasor to the individual "reference" phasor points is a measure for the contribution of that component, where shorter distance means higher contribution. By extending this to a spectrum composed of three different spectra (Fig. 1c), the total phasor falls inside a triangle where the vertices are made up by the phasors of the pure spectra. The contribution of a spectral component to the total spectrum can be determined by calculating the area covered by its phasor and the two opposing vertices divided by the total area of triangle.

Spectral phasor analyses can be employed in several ways. First, the phasors of the data can be compared to the phasor of reference spectra. This provides a simple way to verify the presence of specific fluorescent components in the sample and whether it is present as single component or a mixture. Second, since the phasor points and the image pixels are correlated, a region of interest in the phasor plot can be back projected and highlighted in the original image[17]. This provides a means to visualize a specific population of fluorescent molecules in the image. Third, the linear property of the phasors allows for spectral unmixing of up to three components[14]. To this end the vertices of a reference triangle are manually selected or obtained from reference compounds. Next, the relative contribution of the three components is calculated, as outlined above, for each pixel in the image and multiplied by the intensity in that pixel. This results in three separate images of the individual components.

The accuracy of the analysis is determined by the signal-to-noise in the spectra. Spectra with high signal-to-noise will appear as a point in the phasor plot. However, usually the spectra contain significant levels of noise which introduces variations in the spectrum. As a result, the spot in the phasor plot becomes a diffuse circular cloud. An ellipsoidal cloud, on the other hand, indicates the presence of two components with varying contributions in the pixels.

Instrumentation

Multi-photon spectral imaging was performed using a custom-built imaging system that was described in detail previously[3, 18]. Briefly, the excitation light (Tsunami Titanium: Sapphire laser, Spectra-Physics, Sunnyvale, CA, tuned to 760 nm) is scanned in the XY plane using a galvanometer mirror scanner (040EF, LSK, Stallikon, Switzerland). The infinity-corrected water-immersion objective (40×, NA = 0.8, Nikon, Japan) with a long working distance (2 mm) is mounted on a z-piezo objective translation stage (Mad City Labs, Madison, WI, USA). The emission light is filtered by the dichroic mirror and a multiphoton emission filter (FF01-680/SP-25, Semrock, Rochester, NY, USA). The spectrum is dispersed by a fused silica equilateral prism (Linos, Göttingen, Germany) and focused on a section (~3 lines x 128 pixels) of an EMCCD camera (Cascade 128+ EMCCD, Photometrics, Tucson, AZ, USA, EM gain of 30%-of-maximum has been used in all experiments). Spectral acquisition is

controlled by software written in V++ (Digital Optics, Auckland, New Zealand). The acquisition software read out two equal areas of the CCD chip of 10 lines x 128 pixels separated by 50 lines; the first centered around the image of the spectrum and the second served as a background recording.

Imaging conditions and processing

All in vivo human skin images were recorded using an excitation wavelength of 760 nm, 20 mW excitation power at the specimen. At this excitation wavelength multiple autofluorescence components are simultaneously excited[6]. Here, a pixel dwell time of 128 µs was used and the image size amounted to 224x224 pixels (100x100 µm2). This resulted in a total image acquisition time of 6.5 seconds. Spectral images of the skin of a tanned male volunteer (Caucasian skin type) were acquired. We note that only minimal photo bleaching was observed during the experiments. Each pixel of the spectral image was background corrected by subtracting the simultaneously recorded background from each spectrum. This turned out to be a reliable way to correct for background signals and take care of background variations in time. Before the phasor analyses the spectrum of each pixel was averaged with the spectra of its eight neighboring pixels to increase signal-to-noise.

The spectral images shown here are visualized using a real color visualization method. Briefly, the spectral information is used to assign an RGB value to each pixel that corresponds to the color as perceived by eye. To this end the spectra are multiplied by the wavelength dependent real-color RGB value and integrated over the spectral channels[6].

RESULTS

Fig. 2 shows the spectral phasor analysis of a typical image stack of in vivo Caucasian human skin. As insets, real color RGB images are displayed that show epidermal cells. Besides the blue emission from the epidermal cells, multiple other structures can be distinguished. At the top left, part of the stratum corneum is visible that emits yellow/green emission and at the deeper layers of the purple emission of the dermis is visible[3, 10]. The stratum corneum is present in the top left corner due to a wrinkle in the tissue. The structure of a papillary is clearly visible; it is characterized by strong autofluorescence at intermediate depths and the purple centre due to SHG of collagen in the dermis[3, 5]. The white/green autofluorescence that surrounds the dermal papillary can be attributed to melanin which is abundantly present in papillary of tanned skin[3, 8, 19].

For each image in the stack, spectral phasor plots were calculated. In all phasor plots there is a pronounced spot at the top left quadrant, with a tail pointing to the top right of the plot. With increasing depth a second tail emerges pointing to the bottom center and the first tail becomes more pronounced.

To verify the origin of the different areas in the phasor plot, a more detailed analysis was carried out (Fig. 3). Pixels inside a selected region-of-interest (ROI) in the phasor plot can be traced back to the original image, resulting in a segmented image of pixels with similar spectral properties. Doing this for the pronounced spot in the phasor plot in Fig. 3A shows excellent resemblance between the blue colored cells in the RGB image and the emission from the ROI in the phasor plot. This confirms that this emission indeed origins from the epidermal cells. Selecting the tail to the top right corner in the phasor plot shows that this

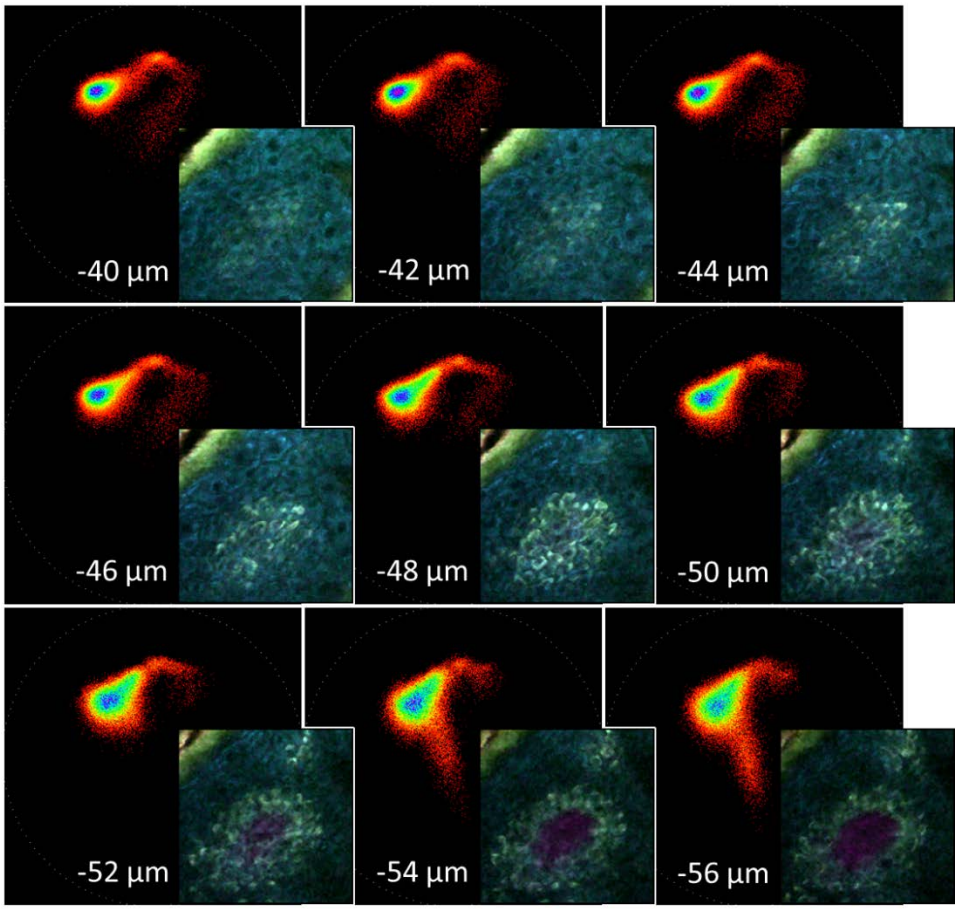

Fig. 2 : Spectral phasor plots of a 3D multiphoton spectral image stack of *in vivo* human skin (Caucasian skin type). Real color RGB images are shown as insets. XY images are 224×224 pixels, corresponding to 70×70 µm²; imaging depth is 40-56 µm. Excitation power is 20 mW, acquisition time is 128 µs per pixel (6,5 s per image), and excitation wavelength is 760 nm. The detection window ranges from 700 nm (channel 1) to 350nm (channel 128); the wavelength is not linear with channel number in the prism based spectrograph.

signal corresponds to emission from the stratum corneum and epidermal cells. Further identification of the emission from the selected regions can be obtained by closer examination of the emission spectra. We note that for each pixel in the image the corresponding position in the phasor plot is determined by the spectrum of that pixel. Therefore, the phasor plot also allows investigation of the biochemical origin of the autofluorescence; phasors can be compared to the phasors of fluorescent reference

components. Here, we employed phasors of reference spectra recorded by Palero et al[6]. Briefly, the upper epidermal cells mainly exhibit fluorescence from keratin[20] (AF with emission maximum λmax=455nm and spectral width Δλ=80-100nm), NADH[21] (AF with λmax=450nm and Δλ=70-90nm) and FAD[22] (AF with λmax=515nm and Δλ=70-90nm), see Fig. 3A. For the epidermal cells near a dermal papillary , there is an additional contribution of melanin (AF with λmax=580nm and Δλ=200-240nm) that is in agreement with literature[3, 8, 23], see Fig. 3B. The fluorescence from the stratum corneum is dominated by keratin and some melanin[3, 20, 23]. In the dermis, there are signals from collagen[5, 24] (SHG at 380 nm, Δλ=0-20nm) and elastin fibers[25] (AF with λmax=490nm and Δλ=110-130nm) (Fig. 3C).

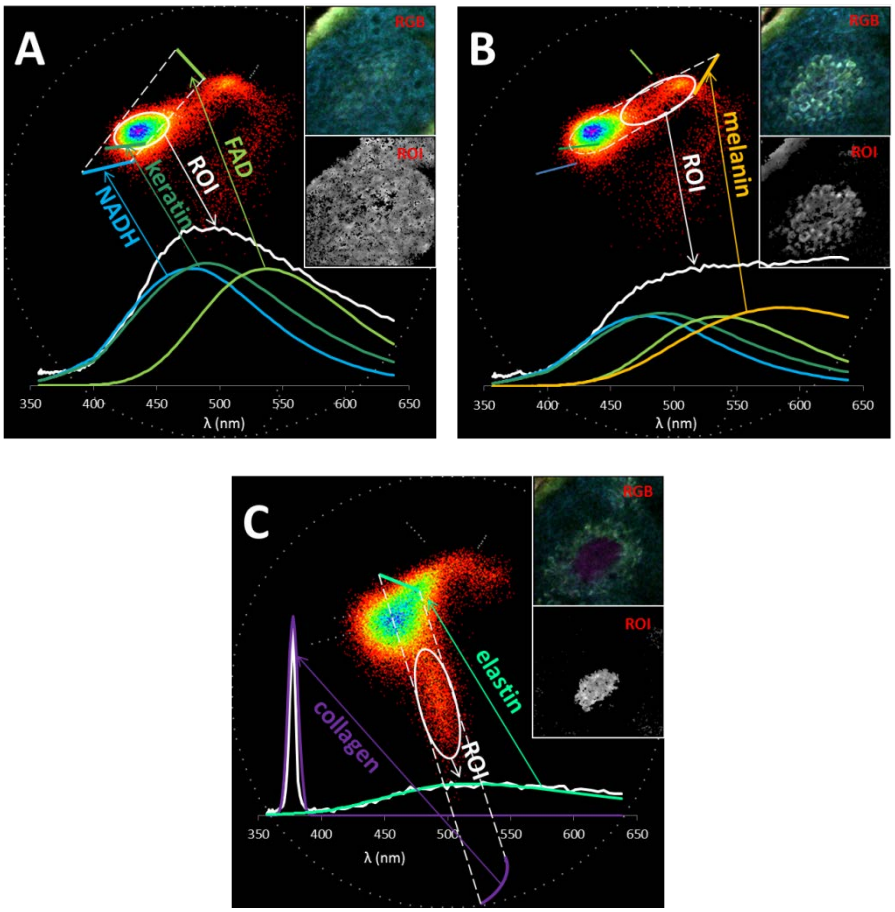

Fig.3 : Analysis of three images (RGB images displayed in insets) of in vivo human skin, based on spectral phasor plots. The pixels segmented inside the white circle are displayed in the ROI image (insets), their average spectrum (white) is compared to reference spectra for collagen (purple), NADH (light blue), keratin (dark green), FAD (yellow/green), elastin (light green) and melanin (yellow). The position of the reference spectra in the phasor is indicated by the solid line (fixed emission maximum, ~20 nm variation in the width of the spectrum is introduced). Experimental conditions are the same as for Fig. 2.

The phasors of these reference compounds are displayed as solid colored lines instead of points in Fig. 3.Reliable values of the width of the spectra is often lacking, the line takes a spread in Δλ into account. Moreover, the spread is used to partially cover spectral variations due to variations in micro-environment, inner filter effects, etc. . The corresponding emission spectra, and the emission spectra of selected ROI, are included in the phasor plot in Fig. 3. The figure confirms the origin of the fluorescence contributions of the various skin layers. The phasors of the epidermal cells are located between the references for NADH, keratin and FAD. Moreover, the cloud in the phasor plot has a slightly oval shape. This is indicative of contributions from multiple fluorescent components.

Fig. 4 shows another image of the same volunteer. Here, a region with low tanning was imaged; therefore the contribution of melanin is comparatively low. The earlier mentioned oval region in the phasor cloud indicates variations in the distribution of fluorescent compounds in the epidermal cells. By selecting regions in the phasor plot this can be analyzed in more detail. Regions with “high”, “average” and “low” NADH to FAD ratio are selected and back projected onto the original image. High and average ratios are observed inside and/or close to the nucleus of the cells. A low ratio, corresponding to comparatively high FAD levels, is found at the periphery of and/or in between the cells.

The phasor plot of the dermis is clearly different from that of the epidermis. In particular it contains a distinct tail pointing in the direction of the lower right corner of the diagram where the phasor of the SHG signal from collagen is found. From this tail-like shape, it is clear that there is large heterogeneity in the collagen fraction in the spectra of dermal pixels. Note that NADH, keratin and FAD are largely absent in the dermis. Instead, fluorescence from elastin is observed here. Unfortunately, elastin has an emission spectrum that can be confused with the NADH/keratin/FAD spectrum of epidermal cells. Still, advantage is taken from the clear spectral difference between AF of elastin and SHG from collagen, and the corresponding strong separation of their reference phasor. This allows us to map the collagen content (relative to elastin) in the dermis (Fig. 5). Structures enriched in collagen can be easily highlighted in this way.

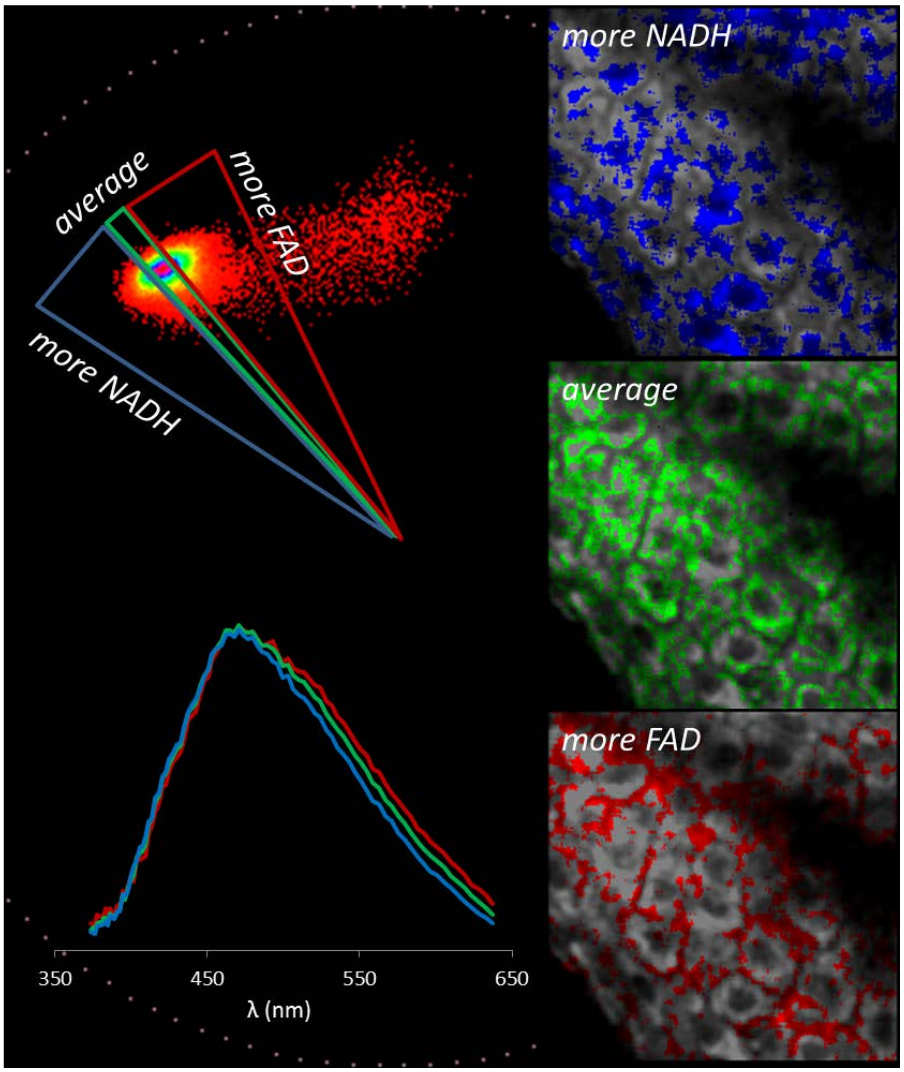

Fig. 4: Spectral phasor plot of image of epidermal cells in *in vivo* human skin (minimal tanning). For three Region of interests (blue = more NADH, green = average, red = more FAD), the average spectra are included. Also the pixels in these ROI are highlighted in their corresponding color in the grayscale intensity images. Experimental conditions are the same as for Fig. 2.

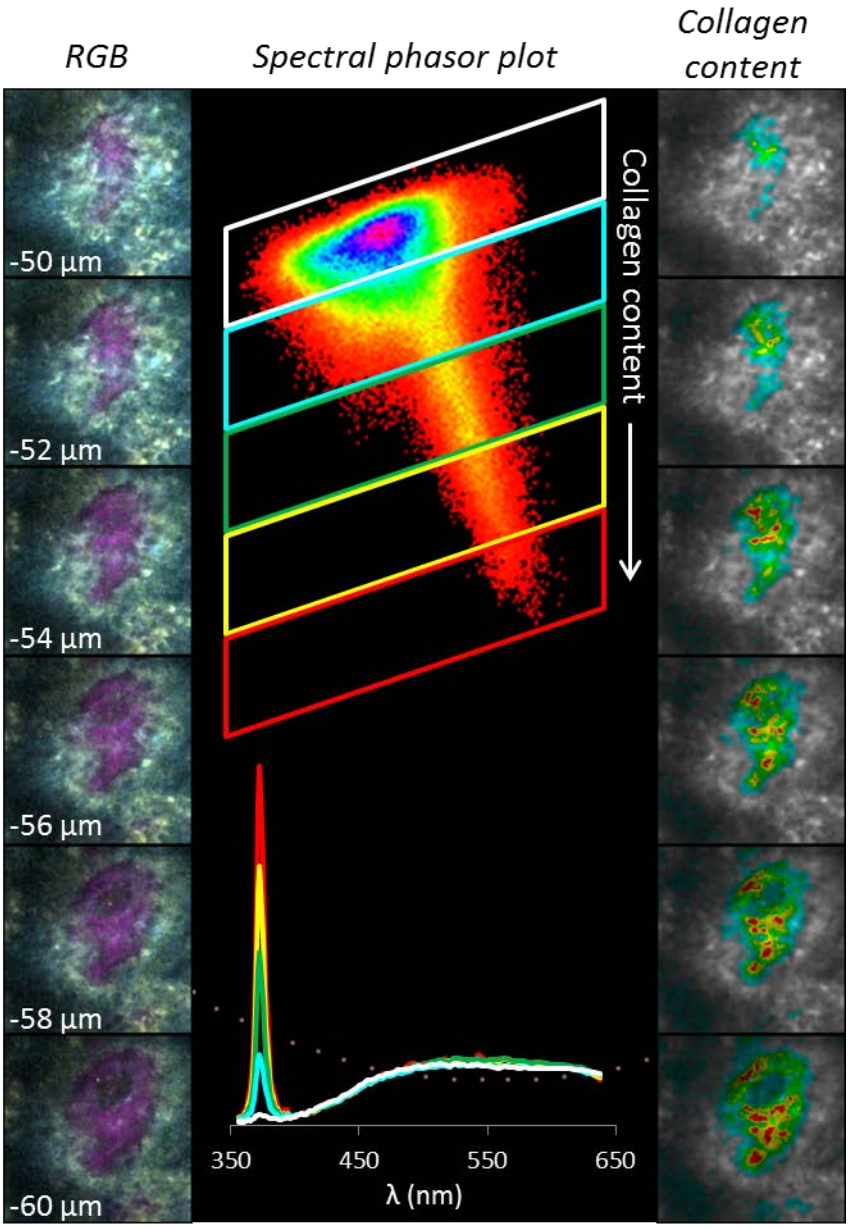

Fig. 5 : Spectral phasor plot of a stack of images of the epidermis/dermis interface in *in vivo* human skin. For five colored ROIs (with increasing collagen content), the average spectra are includes. Also the pixels in these ROI are highlighted in their corresponding color in the grayscale intensity images. Experimental conditions are the same as for Fig. 2.

Phasor analysis can be also employed for spectral unmixing (Fig. 6). The shape of the phasor cloud of tanned skin can be conveniently used for the selection of the vertices of a

reference triangle: the first is the center of the cloud of the epidermal cells (top left), the second is melanin reference (top right) and the third is the collagen reference (bottom). The contribution of melanin in the epidermal cells near the dermal papillary is unmixed and displayed in separate images. The remaining fluorescence of epidermal cells seems independent on the melanin content. Also the signal of the dermis is properly unmixed this way.

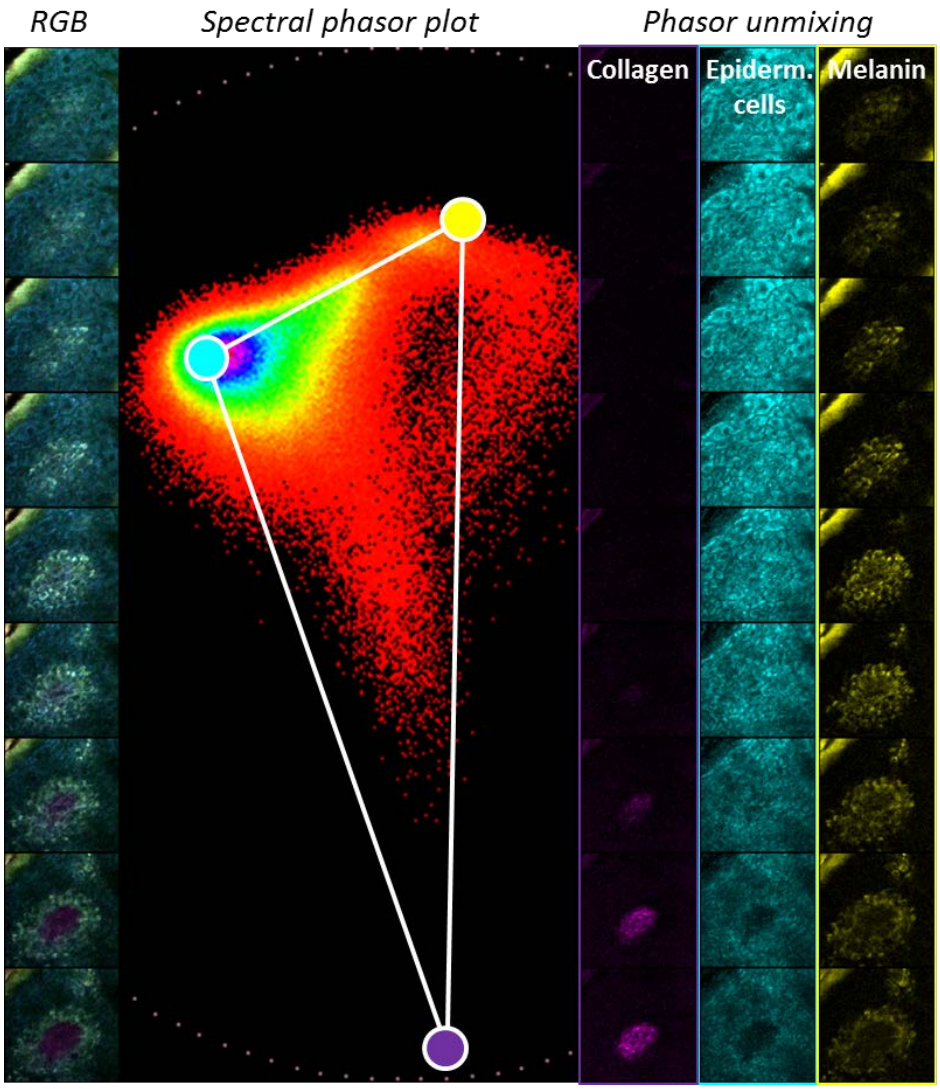

Fig. 6: Unmixing of the image stack of Fig. 2, based on the overall spectral phasor plot. Reference points for epidermal cells (cyan), collagen (purple) and melanin (yellow) were selected as described in the text. The three phasor unmixed image stack are displayed on the right.

DISCUSSION

In the current work, we have evaluated the use of spectral phasors to analyze in-vivo skin. Conventional spectral analyses methods like linear unmixing and principal component analyses methods have been used to analyze conventional spectral imaging data from fluorescently labeled specimens. These techniques are, however, less suitable for analyzing AF and SHG images. In the case of autofluorescence, the number of components is large and often the spectral differences are only minor.

Here, we applied spectral phasor analysis to examine the distribution of autofluorescent components in in-vivo skin. Epidermal cells that are enriched in melanin can be clearly discriminated from cells that show no melanin. Also the Stratum Corneum and dermis contain autofluorescence and SHG features that can be segmented.

A key feature of spectral phasor analysis is that it segments pixels based on their spectral features. Calculating a phasor plot, which can be seen as the “map of spectral properties”, involves only relatively simple mathematics and requires only moderate computational power; a phasor plot can be calculated in a matter of seconds on a standard PC. Once familiar with this type of representation, a phasor plot provides a convenient way of analyzing spectral images. It is easy to incorporate a spread in the fluorescent properties of a compound (λmax and $\Delta\lambda$) as introduced by solvent environment or instrumentals effects. These can be readily detected because the phasor of the measured spectrum does not overlap with the reference phasor.

Another clear advantage over other analysis methods is that it does not rely on fitting algorithms. The outcome of such algorithms can be dependent on the input, and its optimization can be tedious. Even for blind source separation algorithms like nonnegative matrix factorization (NMF)[11] such optimization can be required. When the NMF method was applied on the spectral images used in this paper, it failed to return the separate components; optimization of input spectra was needed to get reasonable results.

The combination of spectral imaging and phasor analysis is a powerful tool for investigating structures and their composition in skin. Of course, it can be applied to other types of tissue as well. Recent advances in multiphoton microscopy / tomography allow noninvasive or minimally invasive investigation of patients. Fast and reliable image analysis tools, like the phasor based approach presented here, are essential for the successful application of these techniques in clinical research.

REFERENCES

1. K. König, "Clinical multiphoton tomography," Journal of biophotonics **1**, 13-23 (2008).

2. T. H. Tsai, S. H. Jee, C. Y. Dong, and S. J. Lin, "Multiphoton microscopy in dermatological imaging," Journal of Dermatological Science **56**, 1-8 (2009).

3. A. N. Bader, A. M. Pena, C. Johan van Voskuilen, J. A. Palero, F. Leroy, A. Colonna, and H. C. Gerritsen, "Fast nonlinear spectral microscopy of in vivo human skin," Biomedical Optics Express **2**, 365-373 (2011).

4. K. König, and I. Riemann, "High-resolution multiphoton tomography of human skin with subcellular spatial resolution and picosecond time resolution," Journal of Biomedical Optics **8**, 432-439 (2003).

5. G. Cox, E. Kable, A. Jones, I. Fraser, F. Manconi, and M. D. Gorrell, "3-Dimensional imaging of collagen using second harmonic generation," Journal of Structural Biology **141**, 53-62 (2003).

6. J. A. Palero, H. S. De Bruijn, A. Van Der Ploeg Van Den Heuvel, H. J. C. M. Sterenborg, and H. C. Gerritsen, "Spectrally resolved multiphoton imaging of in vivo and excised mouse skin tissues," Biophysical Journal **93**, 992-1007 (2007).

7. C. Y. Dong, and P. J. Campagnola, "Optical diagnostics of tissue pathology by multiphoton microscopy," Expert Opinion on Medical Diagnostics **4**, 519-529 (2010).

8. E. Dimitrow, I. Riemann, A. Ehlers, M. J. Koehler, J. Norgauer, P. Elsner, K. König, and M. Kaatz, "Spectral fluorescence lifetime detection and selective melanin imaging by multiphoton laser tomography for melanoma diagnosis," Experimental Dermatology **18**, 509-515 (2009).

9. R. Bazin, F. Flament, A. Colonna, R. Le Harzic, R. Bückle, B. Piot, F. Laizé, M. Kaatz, K. König, and J. W. Fluhr, "Clinical study on the effects of a cosmetic product on dermal extracellular matrix components using a high-resolution multiphoton tomograph," Skin Research and Technology **16**, 305-310 (2010).

10. J. A. Palero, H. S. De Bruijn, A. Van Der Ploeg-Van Den Heuvel, H. J. C. M. Sterenborg, and H. C. Gerritsen, "In vivo nonlinear spectral imaging in mouse skin," Optics Express **14**, 4395-4402 (2006).

11. R. A. Neher, M. Mitkovski, F. Kirchhoff, E. Neher, F. J. Theis, and A. Zeug, "Blind source separation techniques for the decomposition of multiply labeled fluorescence images," Biophysical Journal **96**, 3791-3800 (2009).

12. J. A. Palero, A. N. Bader, H. S. de Bruijn, A. P. van den Heuvel, H. J. C. M. Sterenborg, and H. C. Gerritsen, "In vivo monitoring of protein-bound and free NADH during ischemia by nonlinear spectral imaging microscopy," Biomedical Optics Express **2**, 1030-1039 (2011).

13. Y. Garini, I. T. Young, and G. McNamara, "Spectral imaging: Principles and applications," Cytometry Part A **69**, 735-747 (2006).

14. F. Fereidouni, A. N. Bader, and H. C. Gerritsen, "Spectral phasor analysis allows rapid and reliable unmixing of fluorescence microscopy spectral images," Optics Express **20**, 12729-12741 (2012).

15. M. A. Digman, V. R. Caiolfa, M. Zamai, and E. Gratton, "The phasor approach to fluorescence lifetime imaging analysis," Biophysical Journal **94**, L14-L16 (2008).

16. F. Fereidouni, A. Esposito, G. A. Blab, and H. C. Gerritsen, "A modified phasor approach for analyzing time-gated fluorescence lifetime images," Journal of Microscopy **244**, 248-258 (2011).

17. C. Stringari, A. Cinquin, O. Cinquin, M. A. Digman, P. J. Donovan, and E. Gratton, "Phasor approach to fluorescence lifetime microscopy distinguishes different metabolic states of germ cells in a live tissue," Proceedings of the National Academy of Sciences of the United States of America **108**, 13582-13587 (2011).

18. J. A. Palero, G. Latouche, H. S. De Bruijn, A. Van Der Ploeg Van Den Heuvel, H. J. C. M. Sterenborg, and H. C. Gerritsen, "Design and implementation of a sensitive high-resolution nonlinear spectral imaging microscope," Journal of Biomedical Optics **13** (2008).

19. K. Sugata, S. Sakai, N. Noriaki, O. Osanai, T. Kitahara, and Y. Takema, "Imaging of melanin distribution using multiphoton autofluorescence decay curves," Skin Research and Technology **16**, 55-59 (2010).

20. A. M. Pena, M. Strupler, T. Boulesteix, and M. C. Schanne-Klein, "Spectroscopic analysis of keratin endogenous signal for skin multiphoton microscopy," Optics Express **13**, 6268-6274 (2005).

21. D. W. Piston, B. R. Masters, and W. W. Webb, "Three-dimensionally resolved NAD(P)H cellular metabolic redox imaging of the in situ cornea with two-photon excitation laser scanning microscopy," Journal of Microscopy **178**, 20-27 (1995).

22. S. Huang, A. A. Heikal, and W. W. Webb, "Two-photon fluorescence spectroscopy and microscopy of NAD(P)H and flavoprotein," Biophysical Journal **82**, 2811-2825 (2002).

23. L. H. Laiho, S. Pelet, T. M. Hancewicz, P. D. Kaplan, and P. T. So, "Two-photon 3-D mapping of ex vivo human skin endogenous fluorescence species based on fluorescence emission spectra," Journal of Biomedical Optics **10**, 024016 (2005).

24. M. Strupler, A. M. Pena, M. Hernest, P. L. Tharaux, J. L. Martin, E. Beaurepaire, and M. C. Schanne-Klein, "Second harmonic imaging and scoring of collagen in fibrotic tissues," Optics Express **15**, 4054-4065 (2007).

25. N. Ramanujam, "Fluorescence spectroscopy in vivo," Encyclopedia of Analytical Chemistry, 20-56 (2000).

5

High Speed Multispectral Fluorescence Lifetime Imaging

Submitted to: Optics Express.

ABSTRACT

We report a spectrally resolved fluorescence lifetime imaging system based on time gated single photon detection with a fixed gate width of 200 ps and 7 spectral channels. Time gated systems can operate at high count rates but usually have large gate widths and sample only part of the fluorescence decay curve. In the system presented in this work the fluorescence signal is sampled using a high speed transceiver. An error analysis is carried out to characterize the performance of both lifetime and spectral detection. The effect of gate width and spectral channel width on the accuracy of estimated lifetimes and spectral widths is described. The performance of the whole instrument is evaluated at count rates of up to 12 MHz. Accurate fluorescence lifetimes (error < 2%) are recorded at count rates as high as 4 MHz. This is limited by the PMT performance, not by the electronics.

Analysis of the large spectral lifetime image sets is challenging and time consuming. Here, we demonstrate the use of lifetime and spectral phasors for analyzing images of fibroblast cells with 3 different labeled components. The phasor approach provides a fast and intuitive way of analyzing the results of spectrally resolved fluorescence lifetime imaging experiments.

INTRODUCTION

Lifetime and spectral imaging are complementary techniques that offer noninvasive solutions for quantitative biomedical microscopy. These techniques can, for instance, be used for extracting information about metabolic processes, identification of biochemical compounds and visualization of molecular interactions. The decay kinetics and the emission spectrum of the excited chromospheres can be spatially mapped using a standard microscope equipped with time resolved detection systems for lifetime imaging or spectrographs for spectral imaging. Emission spectra of the excited molecules can be used in co-localization studies of different molecules via unmixing algorithms [1,2], to assess pH [3] and intermolecular energy transfer [4].

Fluorescence lifetime imaging adds another dimensionality to fluorescence imaging and can be employed to assess environmental parameters like calcium concentration [5,6], pH[7], oxygen saturation [8], discriminating bound and free NADH [9]. It can also be used to identify individual components in tissues and their fractional contribution to the fluorescence signal [10]. Importantly, lifetime imaging has become the technique of choice to study molecular interactions. To this end two molecules, donor and acceptor, are fluorescently labeled with different, matched fluorophores. When the molecules are within 10nm of each other Förster Resonance Energy Transfer (FRET) takes place which results in shortening of the donor fluorescence lifetime. This application turned lifetime imaging into a major tool for biological applications [11,12].

Time resolved and spectral imaging provides complementary and sometimes overlapping information. Simultaneous recording of spectra and lifetimes offers the prospect of exploiting this and obtain more and more reliable information than with a single technique. To fully take advantage of this, novel instrumentation that is both robust and affordable is required.

Spectrally resolved lifetime imaging systems have been reported based on both time domain and frequency domains approaches [13]. These systems have been used to improve the accuracy of FRET analyses by including information from both donor and acceptor channels [14,15]. Another application is the unmixing of fluorescence components without a priori knowledge of the sample [16].

To date, all the time domain multispectral FLIM systems are based on time correlated single photons counting (TCSPC). FLIM systems based on continuous sampling, including some time-gating implementations, offer advantages over TCSPC systems. Due to the low dead time of the electronics these systems can operate at high count rates (~10 MHz) without noticeable pile-up effects due to detector electronics, which makes them well suited for rapid lifetime imaging. However, in Time Gating the gates are usually comparatively long and only a limited number of gates are employed. As a result part of the decay curve is not recorded and the curve is often sampled with comparatively long

gate widths. The effects of truncation and sampling of the decay curve are described in "[10,17]".

In this paper we introduce a novel multi-channel detection method for spectrally resolved fluorescence lifetime imaging. This "Lambda-Tau" detector employs an FPGA (Field-programmable gate array) equipped with 8 high speed transceivers running at 5 GHz to record whole decay curves at high count rates and high time resolution (200ps). The multi-channel feature of the FPGA enables simultaneous recording of decay curves for each spectral channel and offers a powerful, scalable solution for spectrally resolved fluorescence lifetime imaging.

MATERIALS AND METHODS

Instrument details

The setup consists of a confocal microscope (Nikon C1, Japan) equipped with a 473 nm solid state diode laser (Becker & Hickl, BDL-473-SMC) with a pulse repetition rate of 20-80 MHz and pulse-width of 40 ps. Imaging of solutions of Fluorescein is performed using a 10x objective (NA = 0.3 Nikon, Japan) and cells are imaged with a 60x water immersion objective (NA = 1.2, Nikon, Japan). In all cell images the field of view is 60x60 um2 and the image size is 160x160 pixels. The confocal microscope is equipped with a fiber coupled output port. A 900 µm diameter fibre is used to couple the microscope to a prism based spectrograph The spectrograph consists of a 100 mm achromatic lens, to make the fluorescence beam parallel, an anti-reflection coated SF10 prism and another lens with the same focal length to focus the dispersed spectrum onto a 32 channel multi-anode linear PMT. The spectral range from 510 nm to 690 nm covers the 7 anodes of the PMT used in our experiments. The spectrograph is wavelength calibrated using a white light super continuum source (NKT photonics, SuperK) equipped with an Acousto-Optic Tunable Filters (AOTF). Single photon output pulses of the PMT channels are fed into the "Lambda-Tau" electronics module. The total measurement time window in our experiments depends on the laser frequency and varies from 12.5 ns to 50 ns . The dead time of the electronics itself is about 1ns, but at present only one photon can be detected per laser pulse per detection channel. A schematic overview of the detection system is shown in Fig.1. The output signals from the multi-anode PMT are first amplified by a fast 8 channel amplifier (bandwidth 1.5GHz, Phillips scientific 774-s-50). Next the pulses are thresholded using a high-speed comparator (MAX9600). Signals above the threshold are fed into the high speed smart transceivers of an FPGA. The FPGA, an Altera Stratix II GX FPGA FPGA, is equipped with eight high speed (5 Gbit) transceivers, (Rocket IO).

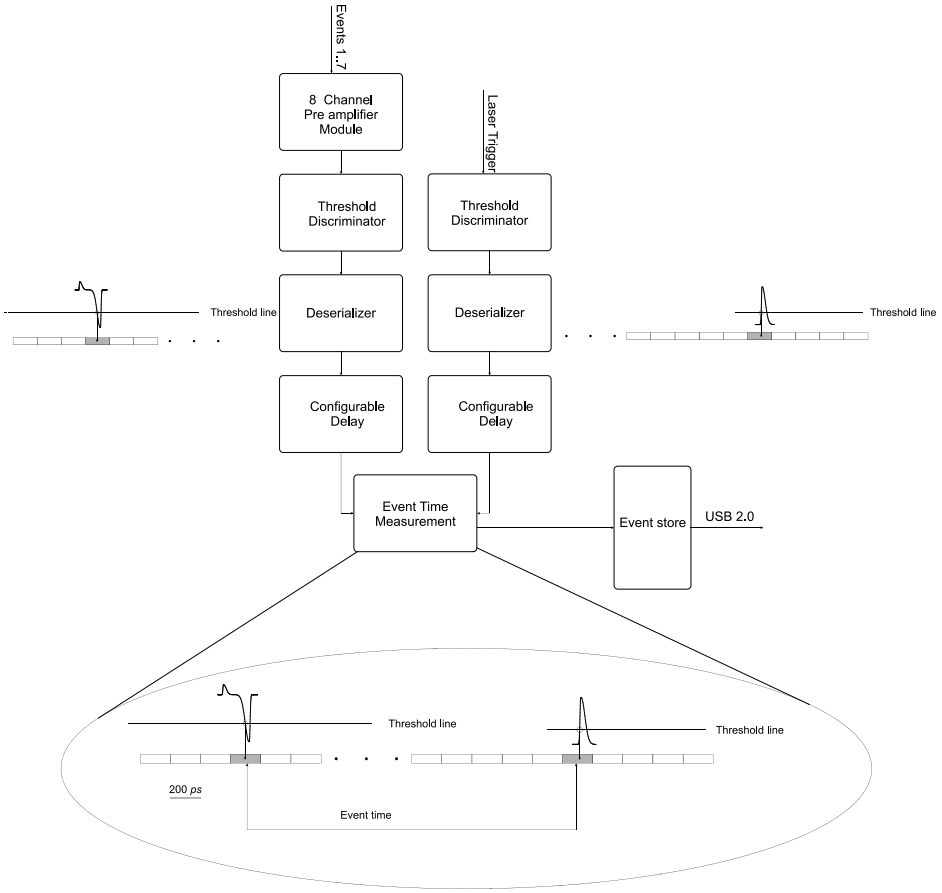

Fig 1. The Schematic diagram of the Lambda-Tau electronics.

The transceiver units convert the serial input signal into 40-bit words, buffer the 40-bit words using a FIFO and also contain a programmable delay with a resolution of 1 ps. The programmable delays are employed to compensate the inter channel time delays, optical delays, PMT color effects [18], signal path length differences and component delays. Here, the delays of the whole system are calibrated by recording the single exponential fluorescence decay from a dye solution (1 mM aqueous solution of Fluorescein at pH 10). Delays are found by fitting an exponential decay convoluted with the experimentally recorded instrument response function and using the shift as a fit parameter.

The laser trigger signal is treated in a similar way and added to the photon event signal of all photon channels by means of a logical adder. One of the transceivers is reserved for recording the laser trigger signal and the remaining channels are employed for recording the signal from the single fluorescence photon events. The laser trigger signal serves as timing reference for the event time measurement of all channels. The deserializer output is analyzed for the presence of the laser trigger and event signals and used to determine the

time difference between the rising edges of the laser trigger and event signals with a time resolution of 200 ps. The performance of the system is tested using a fast pulse generator. A sustained count rate of 25 MHz can be detected; this is limited by the communication speed of the USB 2 port. The event times of all channels are stored in the 512 Mb buffer memory via the PLD memory controller before transfer to the host PC through the USB 2.0 port. A count rate of 125 MHz can be recording for 500 ms before filling up the entire buffer memory.

Data analysis

Spectral lifetime imaging results in very large data sets and requires fast and reliable methods for data analyses. The most commonly used method to analyse fluorescence lifetime data is iterative convolution based on non-linear least square minimization [19]. This is a standard method that is time consuming and not capable of providing fast (real-time) analyses of the acquired data. Although techniques have been developed to improve analyses speed [19-21], this approach remains computationally intensive and comparatively slow. Lambda-Tau images are typically one order of magnitude larger than standard lifetime images. Therefore, implementation of nonlinear least square fitting on a pixel by pixel basis is not suitable for fast analyses of Lambda-Tau images.

Alternatively, recently introduced phasor approaches can be employed to analyse lifetime [10,22] or spectral images [2]. These are graphical approaches that are comparatively simple and fast, but need prior calibration on well characterized samples to obtain quantitative results [23]. Briefly, the real and imaginary parts of the Fourier transform of the fluorescence decay curve or fluorescence emission spectrum are used as coordinates in the phasor plot. The phasor plot and the image are correlated; every point in the phasor plot can be traced back to pixels with the same property in the image. Moreover, every decay or spectrum is mapped onto a unique position in the phasor plot and the position of the phasor determines the lifetime or the spectrum. A region of interest in the phasor plot can be back projected to the pixels correlated with the selected phasor points. This results in fast and convenient image segmentation.

The application of the phasor approach to time domain data with different time gate settings and acquisition periods has been shown before [10]. This theoretical frame work can be applied to different time gate configurations. The general phasor semi-circle is expressed by:

$$R(\tau) = \frac{1}{\cos\left(\frac{\pi}{K}\right) - \sin\left(\frac{\pi}{K}\right)\coth\left(\frac{T}{2K\tau}\right)j} \qquad (1)$$

where K is the number of time gates , T is the total acquisition period and τ is the lifetime. R is a complex number and the reference semicircle is generated by drawing the imaginary part of R versus real part. Fig. 2a shows the modified reference semicircle for different gate

numbers and the same acquisition period for a lifetime range from $\tau / T = 0.01$ to $\tau / T = 5$. As the lifetime increases the phasor moves on the semicircle from right to left. When $K \to \infty$, *R* converges to the standard phasor curve [10]:

$$R(\tau) = \frac{1}{1 - j\frac{2\pi}{T}\tau} \tag{2}$$

The average lifetime can be estimated by the following equations:

$$\tau = \frac{T}{2KArc\coth\left(\frac{G}{S}\cot\left(\frac{\pi}{K}\right)\right)} \tag{3}$$

where G is the Imaginary and S the real part of the phasor. For a binary system with invariant lifetimes and a spread in the relative contributions of the components, a line can be fitted through the phasor points and the intersection of this line with the phasor semicircle yields the lifetimes of the two components:

$$\tau_{1,2} = \frac{T/2K}{Arc\coth\left(\pm\frac{\sqrt{1-2u^2-4uv\cos\left(\frac{\pi}{K}\right)-2u^2\cos\left(\frac{2\pi}{K}\right)}\pm 1}{2u\sin\left(\frac{\pi}{K}\right)}\right)} \tag{4}$$

where *v* and *u* are the slope and the intercept of the fitted line.

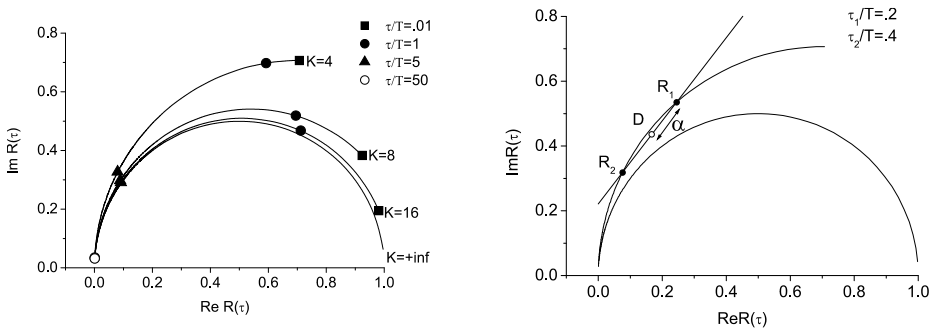

Fig 2 a) Plot of the modified semi-circle for different gate numbers. b) The phasor of a bi-exponential decay curve with lifetimes $\tau_1 / T = 0.2$, $\tau_2 / T = 0.4$ and fractional intensity $\alpha = 0.5$ (open circle).

Similar to lifetime images, the spectral images recorded with the Lambda-Tau detector can be analyzed using the spectral phasor approach; at present the number of spectral channels of the hardware is limited to 7 but this can be easily extended. The spectral phasor approach is versatile and can be employed at low and high numbers of spectral channels see [2]. Briefly, based on the shape and the maximum emission wavelength, the Fourier transform of the spectra are mapped to a unique position in the phasor plot. The peak position (center of gravity) defines the phase in the phasor plot. When the emission moves from red to blue, the phasor rotates from small angles to large angles. The width of the spectrum is related to the modulus of the phasor and as the width gets broader the phasor moves toward the center of the phasor plot. The phasors of artificial Gaussian spectrums with variable peak position k_0 and widths are shown in Fig. 3 for different numbers of spectral detection channels (*K*=8, *K*=16 and *K*=128). The phasor curves for zero width (w=0, corresponding to a delta function) show the maximum extent of the phasors. Non zero width spectra fall inside these curves. In Fig. 3 curves are shown for widths w=0, w=K/8 and w=K/4. The reduction in extent of the semicircle for larger widths is due to the truncation of the Gaussian spectra at the edges of the spectrograph; part of the spectra is not recorded. The phasors for peak positions $k_0=K/4$, $k_0=K/2$ and $k_0=3K/4$ are also shown in Fig. 3. For the zero width spectra, these phasors have phase angles of $\pi/2$, π and $3\pi/2$ radians respectively.

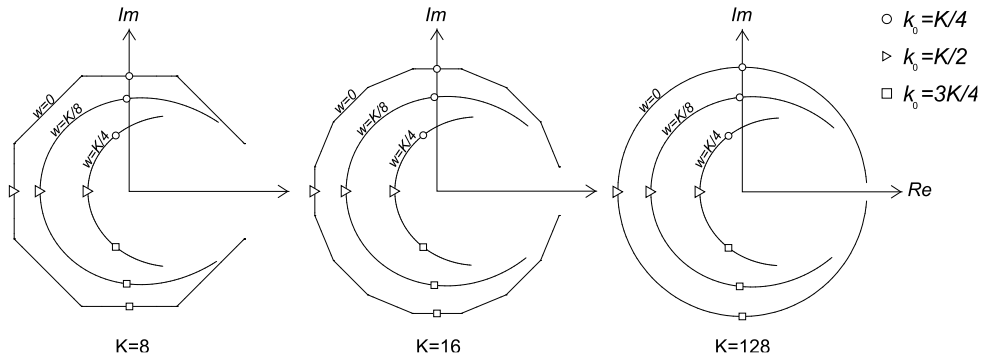

Fig. 3 Spectral phasor plots for Gaussian spectra recorded with K spectral channels and with widths 0, K/8 and K/4. k_0 indicates the peak position (wavelength) of the spectrum.

By increasing the spectral widths the length of the phasor curves shortens; a deviation for $k_0=K/4$ and $k_0=3K/4$ phasors is observed which is due to the non-symmetrical recording of the spectra. The spectra are truncated at the edges of the spectrograph at one end. This effect is not observed for the spectra which are positioned at the center of spectral range of the spectrograph.

Sample details

The Lambda-Tau detector is tested using different specimens. 1 mM aqueous solutions are prepared from Fluorescein (Sigma-Aldrich F6377). FluoCells slide #6 from Invitrogen (F-35925) are used in the imaging experiments. They contain fixed, permeabilized, and labelled muntjac skin fibroblast cells. Mitochondria are labelled with mouse anti–OxPhos Complex V inhibitor protein antibody and visualized using orange-fluorescent Alexa Fluor 555 goat anti–mouse IgG antibody. F-actin is labelled with green-fluorescent Alexa Fluor 488 phalloidin, and the nucleus is stained with TO-PRO-3 iodide.

RESULTS

Error analysis

The Lambda-Tau makes use of continuous sampling of the laser trigger signal and the fluorescence signal. Therefore, it can operate at almost any laser frequency and the total sampling period of the decay equals the time between two laser pulses. The width of the time gates, however, is determined by the clock frequency of the high speed transceivers and fixed at 200 ps. Two major factors determine the accuracy of lifetime acquisition systems: the length of the measurement window and the gate widths. The latter affects the estimation of short lifetimes due to under sampling and the former the estimation of long lifetimes by truncation effects. In order to investigate the sensitivity of the system and compare different settings, a figure of merit *F* [24] was calculated. *F* does not depend on the number of detected photons and its magnitude is always larger than 1. Moreover, lower values of *F* correspond to higher sensitivities for the lifetime measurements. F_τ for lifetime measurements is defined as:

$$F_\tau = \frac{\Delta\tau}{\tau} \Big/ \frac{\Delta N}{N} \qquad (5)$$

where τ is the lifetime and $\Delta\tau$ is the standard deviation of the estimated lifetime. It is assumed that the $\Delta\tau/\tau$ and $\Delta N/N$ are governed by Poisson statistics. Therefore we can rewrite F as:

$$F_\tau = \frac{\Delta\tau}{\tau} \cdot \sqrt{N} \qquad (6)$$

The effect of the gate width and the length of the measurement window can be incorporated by employing the results of Köllner et.al [25]. The analytical solution of the variance in the lifetime estimation can be calculated using Fischer information theory and is given by:

$$\mathrm{var}_N(\tau) = \frac{1}{N}\tau^2 \frac{K^2}{r^2}\left[1-\exp(-r)\right]\left(\frac{\exp\left(r/K\right)\left[1-\exp\left(-r\right)\right]}{\left[\exp\left(r/K\right)-1\right]^2} - \frac{K^2}{\exp\left(r\right)-1}\right)^{-1} \tag{7}$$

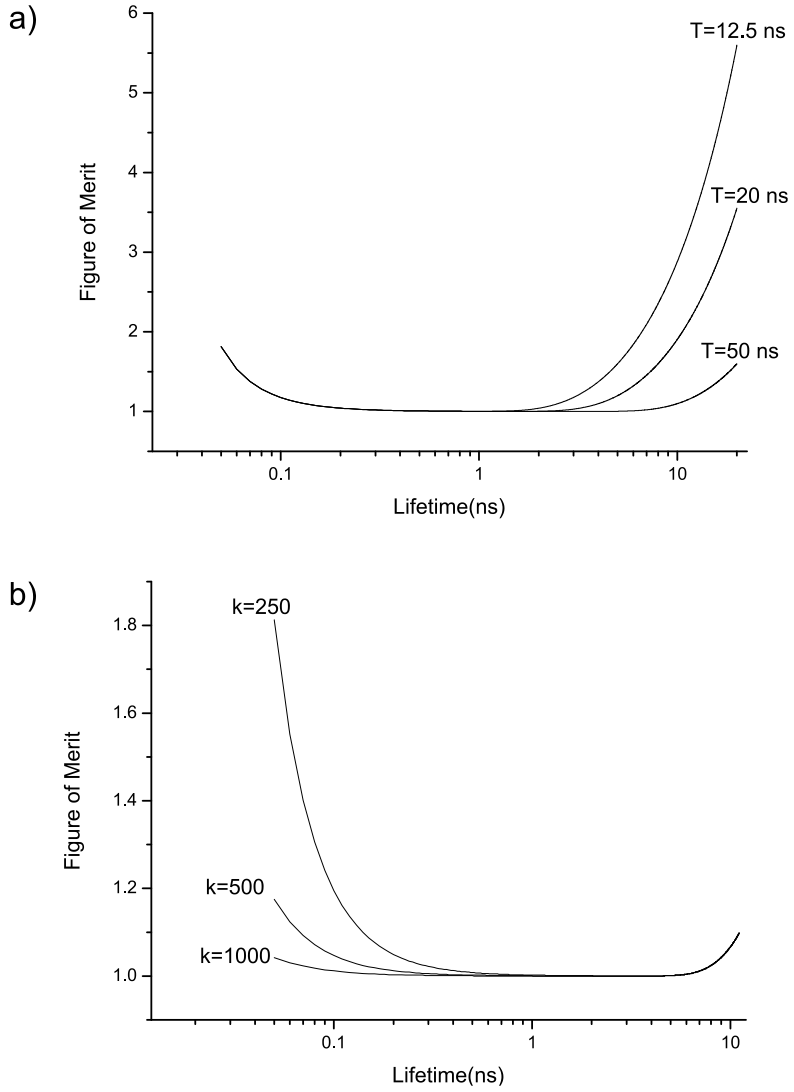

Fig. 4 a) Figure of merit for total time windows of 12.5ns, 20ns and 50 ns and a gate width of 200 ps and b) for a fixed total time window of 50ns and K=1000, 500 and 250 corresponding to gate widths of 50ps, 100ps and 200 ps respectively

where *K* is the number of time gates, *T* is the total length of the measurement window, τ is the lifetime and $r = T/\tau$. Using Eq. 7, F_τ can be written as:

$$F_\tau = \frac{\sqrt{\mathrm{var}_N(\tau)}}{\tau}\sqrt{N} = \sqrt{\mathrm{var}_1(\tau)} \tag{8}$$

where

$$\mathrm{var}_1(\tau) = \frac{K^2}{r^2}\left[1-\exp(-r)\right]\left(\frac{\exp(r/K)\left[1-\exp(-r)\right]}{\left[\exp(r/K)-1\right]^2} - \frac{K^2}{\exp(r)-1}\right)^{-1} \tag{9}$$

Fig 4a. shows the Figure of merit F_τ as a function of lifetime for a total measurement time windows of 12.5ns, 20ns and 50 ns, which corresponds to laser frequencies of 80MHz, 50MHz and 20 MHz respectively. The figure shows that for short lifetimes the F_τ values for different total time windows converge to the same curve, determined by the fixed gate width of 200ps. For long lifetimes F_τ increases due to truncation of the decay curve. Part of the signal is not included in the analyses and the sensitivity of the measurement goes down.

In order to demonstrate the effect of the gate width on F_τ, Fig. 4b shows F_τ as a function of lifetime for gate widths of 50ps, 100ps and 200 ps and a total measurement window of 50ns. This corresponds to K=1000, 500 and 250 respectively. As expected, now the figure of merit for longer lifetimes takes on the same values for different gate widths, but for short lifetimes, F_τ increases more rapidly for large gate widths. The required number of photons to realize certain accuracy can be calculated using:

$$N \geq \frac{\mathrm{var}_1(\tau)}{(\text{desired accuracy})^2} \tag{10}$$

For instance, to analyze a mono exponential decay with a lifetime of 200 ps using gate widths of 200 ps, the required number of photons for realizing a 10% accuracy amounts to 108. This is, only 8% higher than the number of photons for F_τ=1. In order to investigate the sensitivity of the spectral imaging system a figure of merit F_λ was defined and calculated for different configurations. Assuming a Gaussian spectrum with spectral width σ, k spectral channels and a total spectral detection range L, the variance in the spectral width can be calculated using Fischer information theory:

$$\mathrm{var}_N(\sigma) = \frac{1}{N}\left(\sum_{i=1}^{k}\frac{erf\left(\frac{\sqrt{2}L}{4k\sigma}(k-2i+2)\right) - erf\left(\frac{\sqrt{2}L}{4k\sigma}(k-2i)\right)}{erf\left(\frac{\sqrt{2}L}{4\sigma}\right)}\right)^{-1} \tag{11}$$

where *erf* is the error function and N the number of detected photons. The figure of merit for the spectral width estimation can now be calculated using Eq.6. Spectral figure of merit curves are shown in Fig. 5 for a fixed spectral window of 300 nm for 4, 8, 16 and 32 spectral channels. The maximum emission wavelength is assumed to be fixed and at the centre of the spectral range. For large spectral widths the figure of merit curves exhibits the same behaviour for all numbers of spectral channels and the figure of merit gradually goes up for increasing wavelengths. This is due to the truncation of the spectra at the edges of the spectrograph. For small spectral widths the figure of merit rapidly increases; as expected this effect starts sooner for spectrographs with a low number of channels. For typical organic fluorescent dye molecules the spectral widths are in the order of 40nm. Increasing the number of spectral channels from 8 to 32 only slightly improves the performance of the spectrograph at this spectral width. F_λ changes from 0.77 to 0.72, corresponding to a decrease from 58 photons to 51photons for realizing 10% accuracy. We note that the current configuration of Lambda-Tau has 7 spectral channels. The figure of merit curves for 7 and 8 spectral channels almost completely overlap.

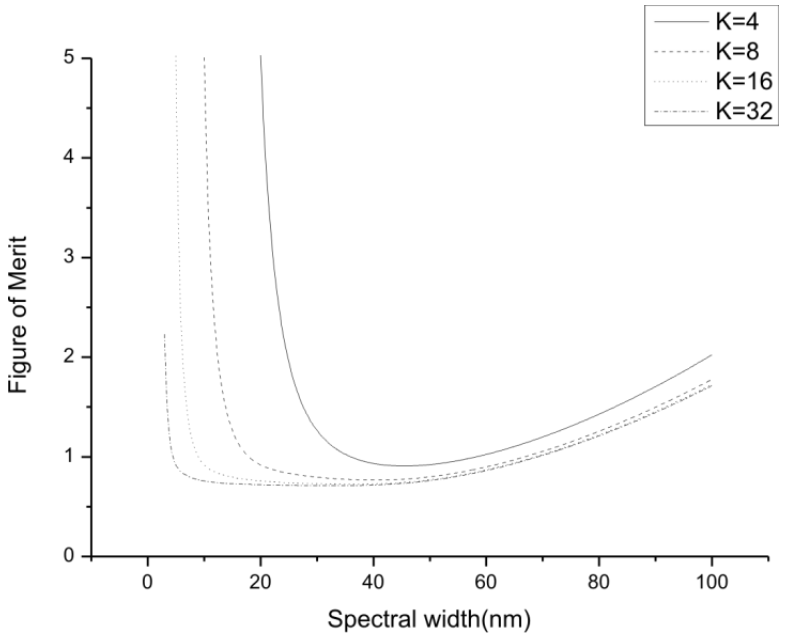

Fig. 5 The figure of merit for spectral widths for different numbers of spectral channels.

Lifetime accuracy and count rate

To demonstrate the performance of the system at different count rates, a 0.1mM aqueous solution of Fluorescein with pH 10 is imaged using different neutral density filters in the emission path. In this way effects on the fluorescence emission related to variations in the excitation power, e.g. saturation effects, are avoided. The recorded images are sorted according to their count rates and analysed with iterative convolution technique. The laser is operated at a 20 MHz repetition frequency corresponding to a 50ns time window and

250 time gates. The instrument response is measured by recording scattered laser light from the surface of a cover glass. Fig. 6a shows a typical measured decay curve recorded at a count rate of 0.1 MHz and a single exponential fit. The latter is based on iterative convolution that includes the instrument response function; the $\chi^2 = 1.12$ indicates a good quality fit. The background signal is estimated in a separate fit. Fig. 6b shows the estimated lifetime as a function of count rate. The fitted lifetime decreases with count rate. This is explained by the dead-time of the PMT; by increasing the count rate the probability of two successive photons arriving at the PMT within the dead-time of the PMT goes up. This pile-up is more probable at the beginning of the decay curve which results in a shortening of the measured lifetime. In addition, the detection efficiency goes down. Below a count rate of 1MHz the shortening in the life time due to the dead-time of the PMT is less than 2% (dotted line). In order to test the Lambda-Tau at higher count rates, the outputs of four PMT are combined using high bandwidth power combiners and connected to a single channel of the Lambda-Tau electronics. Now, the error in the lifetime stays below 2% up to a count rate of about 5MHz, see Fig. 6c. By increasing the count rate above 5 MHz the error in the estimated lifetime increases and it shows a similar trend as in the case of a single PMT. This demonstrates that the individual channels of the Lambda Tau can operate at high count rates without significant pile-up effects. Importantly, in most spectral imaging experiments the fluorescence signal is spread out over multiple spectral channels; in our 7 channel system count rates as high as 7 MHz can be realized without significant pulse pile-up effects. Basically, the performance is limited by the detector performance and when al 32 PMT channels would be used count rates as high as 32 MHz can be dealt with without significant pile-up effects.

Analysis of recoded image of cells

Spectral lifetime images (60x60 μm^2) of FluoCells test slide #6 are recorded with the Lambda Tau detector and analyzed using the Spectral Phasor and Time Gated Phasor methods. Homemade ImageJ plugins are used for the analyses (plugins are available from http://www.spechron.com/). Fig. 7 shows a series of lifetime images recorded at different spectral channels and their corresponding phasor plots. The 7^{th} channel with central wavelength of 754 nm is not shown here because of very low counts collected at this channel. Lifetimes are calculated employing Eq.3 using *K*=62 and *T*=200 ps (80 MHz laser frequency). The central wavelength of each spectral channel is indicated at the bottom left in the lifetime images. By moving from the green to the red emission channels, the lifetime phasor gradually moves from the phasor of Alexa 488 with average lifetime of 2.23 ns to the phasor of Alexa 555 with lifetime of about 1.55 ns. In the fourth channel both Alexa 488 and Alexa 555 are present resulting in an elongated phasor. In the lifetime images the same trend is visible from the color coding of the lifetimes; when moving from shorter to longer emission wavelengths the Alexa 555 lifetime becomes visible.

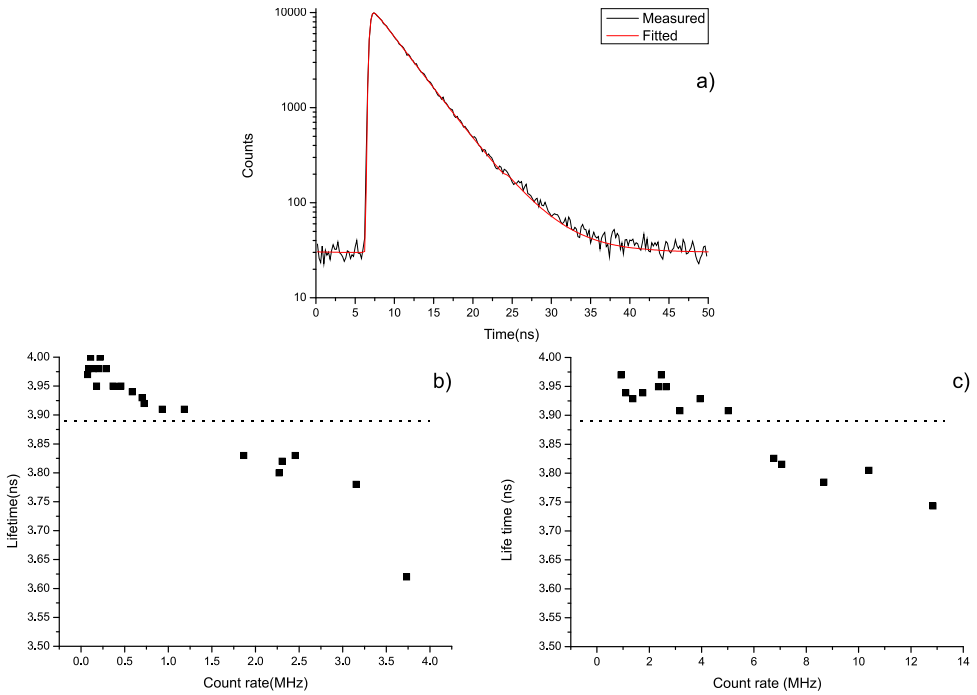

Fig. 6 a) Measured and fitted fluorescence decay curves. b) Fitted lifetimes as a function of detection count rate using a single detection channel. c) As in b) using the signal from 4 combined channels. The dashed line indicates an accuracy of 98%.

In the second image, central wavelength 536nm, most of the pixels have count rates of ~0.5 MHz and some pixels have count rates close to 1MHz. The minimum image acquisition time is determined by the time required to collect enough photons in each pixel. According to Eq. 10 and using K=62, T=200 ps and 160x160 pixels, it takes 140 photons to measure a lifetime of 3ns with 10% accuracy. This takes about 4 seconds at 1MHz count rate. Considering 7 spectral channels the total count rate can reach 7 MHz and binning of all channels results in acquisition times of less than 1 second. For the image of Fig. 7 the recording time is almost 30 seconds. This is due to the comparatively low count rate at the longest wavelength channel. Fig. 8a shows the spectral phasor and the real-color representation of the spectral image [26]. The spectral image is obtained by binning all time channels. As expected for a two component system the phasor is elongated. Two circular regions of interests are selected in the phasor plot and the corresponding images are shown on the right. The region of interest indicated by the upper circle selects the pixels with shorter emission wavelengths and the lower circle selects the pixels with longer emission wavelengths.

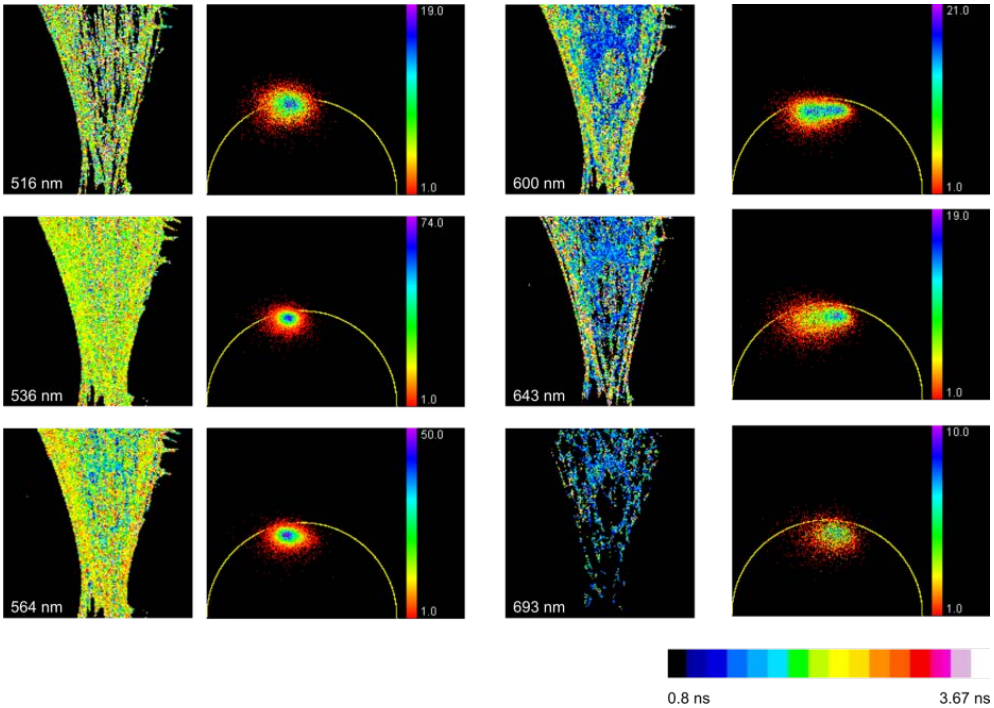

Fig. 7 The phasor plots and fluorescence lifetime images calculated using Eq. 3.

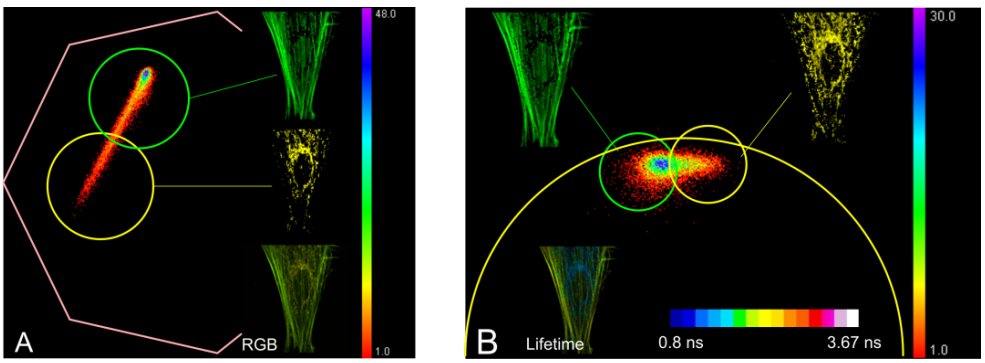

Fig. 8 Spectral phasor based segmentation.

Segmentation based on back projecting these region into the original image yields images corresponding with the Alexa 488 colored actin fibers and Alexa 555 colored mitochondria. Fig. 8b shows the time gated phasor for the same image set, now binned over the spectra. Again, two circular regions of interest are selected and their corresponding pixels are shown. The left circle segments the pixels with longer lifetime, corresponding to Alexa 488, and the right circle segments the pixels with shorter lifetime, corresponding to Alexa 555. Good correlation is observed between the segmented images from spectral and time gated

phasors. Fig. 8b also shows the lifetime image at the bottom. Here, the lifetime is color coded and scaled with the intensity (counts). The complete lifetime phasor analyses of 7 spectral channels with 64 time bins each per pixel of an 160x160 pixels image takes about 4 seconds using a single core on a standard PC. This is much faster than standard iterative convolution technique which takes about 1 second per pixel to estimate the lifetime. Phasor analysis facilitates fast analysis of the large spectral lifetime images.

Discussion and conclusions

A spectrally resolved fluorescence lifetime imaging system based on FPGA technology is presented. This novel system samples the decay with 200 ps resolution and can record full decay curves. The total measurement window is limited by the laser repetition frequency; it can be extended by lowering the frequency of the laser. An error analysis to investigate the performance of the system for lifetime detection is performed and shows that only 108 photons are required to achieve 10% accuracy in lifetimes as short as 200 ps. In biological applications the lifetimes vary between ~200 ps to ~8 ns. The current configuration (200 ps gate width, 50 ns time window) is very well suitable for this kind of application. The accuracy for longer lifetimes can be increased by increasing the total measurement window. The system is capable of operating at high count rates which makes it useful for many applications. We showed the performance of the instrument at different count rates and it is found that the system can handle count rates as high as 4 MHz per channel without any significant pulse pile-up effects. The maximum count rate is limited by the PMT performance and it is shown that the count rate can go up to 1 MHz and below this range 98% accuracy in lifetime estimation is achieved. This is particularly important in FRET experiments. Here, the FRET efficiency is proportional to the lifetime shortening. The error in the lifetime sets a limit to the smallest FRET efficiencies that can be detected. The total spectral window is about 280 nm wide, from 500 nm to 780 nm, and covers the spectra of a large number of fluorophores. It can be easily shifted to include more blue spectra. Compared to single dimensional detectors, like spectral imaging or lifetime imaging systems, this setup provides more information with the same number of detected photons. Combined analyses of spectral and lifetime data can provide more quantitative and more accurate information of biological events. Combined analysis of excitation spectra and lifetimes has been employed already for the unmixing of fluorophores; here fractional intensities and excitation spectra of each component were recovered with minimal a priori information [16].

FRET imaging is a major application for spectral imaging and lifetime imaging. The simultaneous recording of emission spectra and fluorescence lifetimes opens the possibility for a full and simultaneous analyses of the emission of both donor and acceptor molecules. Simultaneous analysis has the potential to provide more accurate energy transfer efficiencies at low signal levels. The analysis of multidimensional images, however, is challenging.

Here, a basic analysis based on a phasor approach is reported. This provides a fast and reliable means to analyses the spectral data and the lifetime data. Currently, the number of spectral channels in our system is limited to 7 but this can easily be extended to meet the requirements of more demanding experiments. Extending the system to handle higher number of spectral channels is under considerations. Multiple (8-channel) units can run in parallel to extend the number of spectral channels. On the other hand photon statistics should be considered as well; extending the number of spectral channels reduces the signal to noise ratio. It is shown that the Lambda-Tau unit can count higher count rates and the limitation is only due to the PMT. Lambda-Tau can be a perfect match for SPAD or hybrid detectors which can handle higher count rates[27].

REFERENCES

1. R. A. Neher, M. Mitkovski, F. Kirchhoff, E. Neher, F. J. Theis, and A. Zeug, "Blind source separation techniques for the decomposition of multiply labeled fluorescence images," Biophys. J. **96,** 3791-3800 (2009).

2. F. Fereidouni, A. N. Bader, and H. C. Gerritsen, "Spectral phasor analysis allows rapid and reliable unmixing of fluorescence microscopy spectral images," Optics Express **20,** 12729-12741 (2012).

3. M. R. Hight, D. D. Nolting, E. T. McKinley, A. D. Lander, S. K. Wyatt, M. Gonyea, P. Zhao, and H. C. Manning, "Multispectral fluorescence imaging to assess pH in biological specimens," J. Biomed. Opt. **16,** (2011).

4. Y. Chen, J. P. Mauldin, R. N. Day, and A. Periasamy, "Characterization of spectral FRET imaging microscopy for monitoring nuclear protein interactions," J. Microsc. **228,** 139-152 (2007).

5. A. Agronskaia, L. Tertoolen, and H. Gerritsen, "Fast fluorescence lifetime imaging of calcium in living cells," J. Biomed. Opt. **9,** 1230 (2004).

6. A. Celli, S. Sanchez, M. Behne, T. Hazlett, E. Gratton, and T. Mauro, "The epidermal Ca2 gradient: Measurement using the phasor representation of fluorescent lifetime imaging," Biophys. J. **98,** 911-921 (2010).

7. R. Sanders, A. Draaijer, H. C. Gerritsen, P. M. Houpt, and Y. K. Levine, "Quantitative pH imaging in cells using confocal fluorescence lifetime imaging microscopy," Anal. Biochem. **227,** 302-308 (1995).

8. J. Lakowicz, "Principles of Fluorescence spectroscopy. 1999," Kluwer Academic/Plenum Publisher, New York, Kap **9,**.

9. J. R. Lakowicz, H. Szmacinski, K. Nowaczyk, and M. L. Johnson, "Fluorescence lifetime imaging of free and protein-bound NADH," Proceedings of the National Academy of Sciences **89,** 1271 (1992).

10. F. Fereidouni, A. Esposito, G. Blab, and H. Gerritsen, "A modified phasor approach for analyzing time-gated fluorescence lifetime images," J. Microsc. (2011).

11. V. E. Centonze, M. Sun, A. Masuda, H. Gerritsen, and B. Herman, "Fluorescence resonance energy transfer imaging microscopy," Methods Enzymol. **360,** 542-560 (2003).

12. R. Clegg, "Fluorescence Resonance Energy Transfer, Fluorescence Imaging Spectroscopy and Microscopy, vol. 137," John Wiley & Sons, New York **155,** 156 (1996).

13. Q. S. Hanley, "Spectrally resolved fluorescent lifetime imaging," Journal of The Royal Society Interface **6,** S83-S92 (2009).

14. D. Strat, F. Dolp, B. von Einem, C. Steinmetz, C. A. F. von Arnim, A. Rueck, and others, "Spectrally resolved fluorescence lifetime imaging microscopy: Fo\ rster resonant energy transfer global analysis with a one-and two-exponential donor model," J. Biomed. Opt. **16,** 26002 (2011).

15. Y. C. CHEN and R. Clegg, "Spectral resolution in conjunction with polar plots improves the accuracy and reliability of FLIM measurements and estimates of FRET efficiency," J. Microsc. (2011).

16. S. Schlachter, S. Schwedler, A. Esposito, G. Kaminski Schierle, G. Moggridge, and C. Kaminski, "A method to unmix multiple fluorophores in microscopy images with minimal a priori information," Optics Express **17,** 22747-22760 (2009).

17. R. W. K. Leung, S. C. A. Yeh, and Q. Fang, "Effects of incomplete decay in fluorescence lifetime estimation," Biomedical optics express **2,** 2517-2531 (2011).

18. D. Bebelaar, "Time response of various types of photomultipliers and its wavelength dependence in time-correlated single-photon counting with an ultimate resolution of 47 ps FWHM," Rev. Sci. Instrum. **57,** 1116-1125 (1986).

19. D. O'connor, W. Ware, and J. Andre, "Deconvolution of fluorescence decay curves. A critical comparison of techniques," J. Phys. Chem. **83,** 1333-1343 (1979).

20. A. Gafni, R. L. Modlin, and L. Brand, "Analysis of fluorescence decay curves by means of the Laplace transformation," Biophys. J. **15,** 263-280 (1975).

21. J. A. Jo, Q. Fang, T. Papaioannou, and L. Marcu, "Fast model-free deconvolution of fluorescence decay for analysis of biological systems," J. Biomed. Opt. **9,** 743 (2004).

22. M. A. Digman, V. R. Caiolfa, M. Zamai, and E. Gratton, "The phasor approach to fluorescence lifetime imaging analysis," Biophys. J. **94,** L14-L16 (2008).

23. B. Spring and R. Clegg, "Image analysis for denoising full-field frequency-domain fluorescence lifetime images," J. Microsc. **235,** 221-237 (2009).

24. H. Gerritsen, M. Asselbergs, A. Agronskaia, and W. Van Sark, "Fluorescence lifetime imaging in scanning microscopes: acquisition speed, photon economy and lifetime resolution," J. Microsc. **206,** 218-224 (2002).

25. M. Köllner and J. Wolfrum, "How many photons are necessary for fluorescence-lifetime measurements?" Chemical Physics Letters **200,** 199-204 (1992).

26. J. A. Palero, H. De Bruijn, van der Ploeg-van den Heuvel, A., H. Sterenborg, and H. Gerritsen, "In vivo nonlinear spectral imaging in mouse skin," Optics Express **14,** 4395-4402 (2006).

27. D. U. Li, J. Arlt, J. Richardson, R. Walker, A. Buts, D. Stoppa, E. Charbon, and R. Henderson, "Real-time fluorescence lifetime imaging system with a 32× 32 0.13 μm CMOS low dark-count single-photon avalanche diode array," Optics express **18,** 10257-10269 (2010).

6

Blind unmixing of spectrally resolved lifetime images

ABSTRACT

A novel method is presented for blind unmixing spectrally resolved fluorescence lifetime images. The method is based on the combined analyses of spectral and lifetime phasors and allows unmixing of up to 3 components without any prior knowledge. Fractional intensities, spectra and decay curves of the individual components can be extracted with this new technique. The reliability and sensitivity is investigated and the possibility of extending the method to unmix more components is discussed. The method is evaluated on mixtures of fluorescent dyes and labeled cells.

INTRODUCTION

Unmixing of spectral and lifetime images has been extensively used to study the distribution and colocalization of fluorophores in specimens. In spectral or lifetime unmixing the total spectrum or decay is decomposed into the separate components. Applications of unmixing can be found in for instance, biology, chemistry, earth sciences and numerous unmixing algorithms have been developed. Among the techniques developed for unmixing the principal components, linear unmixing serves as a standard and straightforward technique which assumes a linear superposition of different components [1]. This approach requires the knowledge of reliable references for the individual components. However, recording reference spectra or decays is not always trivial; they may be subject to changes induced by e.g. solvents. This complication also occurs when we are dealing with the unmixing of endogenous fluorophores in which case recording of the reference spectra or decays is often not feasible.

Recently, novel techniques including Spectral Phasor Analyses (SPA) [2], Non-negative Matrix Factorization (NMF) [3] and Principal Component Analysis (PCA) [4] have been developed that overcome this problem. Principal Component Analyses (PCA) is based on setting up a perpendicular coordinate system, called principal components, and maximization of the variances of the data points along each of the perpendicular coordinates. The method is mathematically complicated and has been successfully used, for instance, for unmixing of Flavin autofluorescence components [5]. NMF uses constraints including non-negative spectra and intensity fractions and the minimization of a cost function to unmix the spectral images. The application of NMF for analyzing lifetime images is also reported [6]. In this technique a rough estimation of spectra of constituent components is necessary as an input and the final result is dependent on the initial input. In SPA unmixing is achieved by employing reference phasors and exploiting the linear behavior of the phasors. The reference phasors can be estimated from the recorded spectral image itself. This is performed by extracting the maximum emission wavelength of pure spectra from the average spectrum. The choice of the reference points is subject to errors and the accuracy of the unmixing depends on the estimate of the reference points by the user.

Efforts have been made to employ extra information, like excitation spectra or lifetimes, to alleviate the requirement of reference data and to increase the robustness of the unmixing. The parallel factor analysis (PARAFAC) [7] was introduced to blindly unmix up to 5 components without prior knowledge; here, a filter wheel was employed to record fluorescence excitation images and increase the amount of data available for unmixing. This method suffers from comparatively long acquisition times, and a fairly complicated acquisition process.

Schlachter et. al [8] employed a series of lifetime images recorded at different excitation wavelengths to enhance the unmixing process. They successfully demonstrated the

unmixing of two components without prior knowledge about the components. This method is, however, limited to dyes exhibiting single exponential decays and the unmixing is performed based on a global lifetime estimation using a phasor approach.

A combined multi modal analysis has the potential to provide more detailed information about the fluorophores. Moreover, the simultaneous recording with a single detector of different properties of the fluorophore, for instance emission wavelength and fluorescence lifetime, results in additional information from the same number of photons compared to the recording of a single property. This potentially opens the door to reliable unmixing with fewer numbers of detected photons. This requires, however, that the fluorophores to be unmixed have differences in multiple of the imaging modalities. A good example is the presence of a free and bound state of NADH. The emission maxima of free and bound NADH differs by 20nm [9] and their lifetimes are 0.3 ns - 0.5ns and 1.6 - 3.7 ns [10] for free and bound NADH respectively.

In frequency domain lifetime imaging systems, two different modulation frequencies need to be used to extract the lifetimes of a two component mixture; this complicates the image acquisition and results in longer acquisition times. Hanley et al. [11] used frequency domain spectral lifetime imaging and employed a phasor approach to unmix two components and their lifetimes using only a single modulation frequency for the excitation light. The spectral information removes the need for the extra recording at other harmonics. In a more recent publication [12] it is shown that the unmixing process becomes more accurate when spectral and lifetime information is combined. It is possible to unmix the signals from Rhodamine and fluorescein even when the fractional intensity of the Rhodamine is below 2%.

In this paper we report a new technique which combines spectral and lifetime data to unmix the fractional intensities, emission spectra and decays of pure components. This method relies on the use of spectral phasors and lifetime phasors and does not require any reference data for unmixing. Every spectrum or decay curve is transformed into a single point in the phasor plot; this reduces the unmixing procedure to finding the reference phasor points of pure components. The method is tested on digitally added images of single dye solutions to generate a two and a three component system. We show that unmixing can be performed with average photon counts as low as 500 counts/pixel. Moreover, images with spectra separated by only 20 nm and lifetimes separated by 700 ps can be unmixed. Finally, the method is also tested on images of labeled cells.

TEMPORAL AND SPECTRAL PHASOR ANALYSES

Our novel unmixing method is based on the use of phasors. Previously, phasor analysis has been successfully employed for analyzing spectral and lifetime images [2,13]. In this approach the decay curve or the spectrum are Fourier transformed and mapped as a single point in a phasor plot. Here, the x axis is used to map the real part and the y axis to map

the imaginary part of the first harmonic of the Fourier transformation. This approach facilitates the analysis of lifetime and spectral images by visualization of the data in a 2D plot.

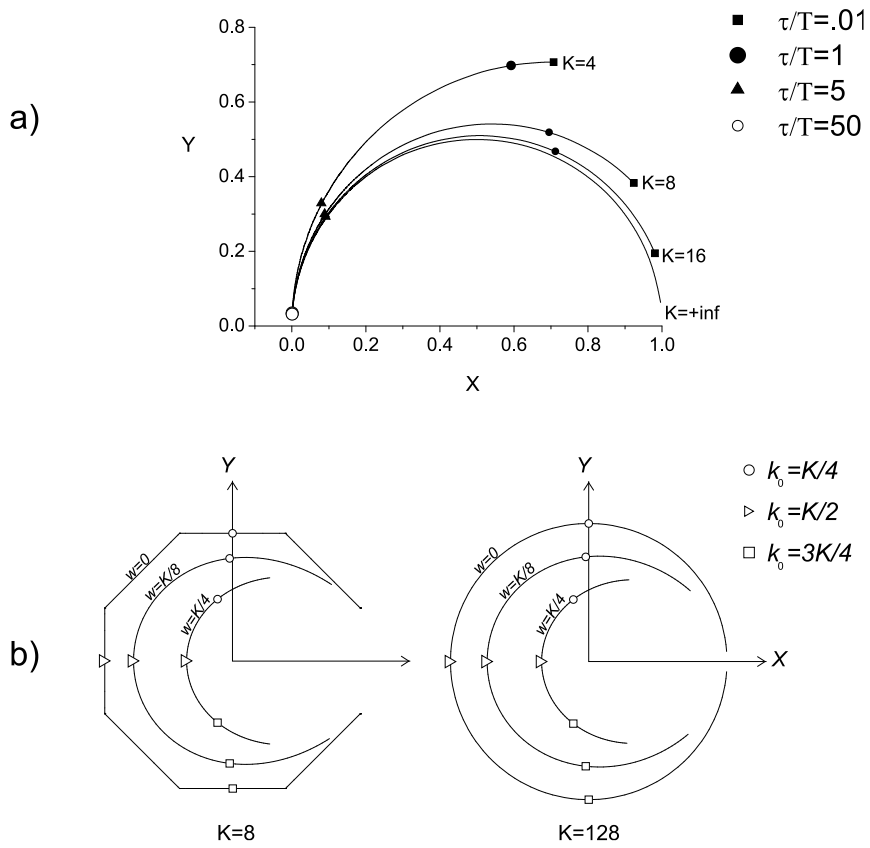

Fig. 1 a) Time gated phasors for different (normalized) lifetimes and numbers of time gates (K); b) spectral phasor reference curves for different numbers of spectral channels and spectral widths.

The position of the phasor depends on the shape of the spectrum or the decay curve. There is a one to one correlation between phasor points and pixels with a particular spectrum or lifetime; this allows for a simple and straightforward image segmentation. Fig. 1a shows reference phasor curves for a time gated system with different numbers of gates and the same total measurement window; the lifetime range runs from $\tau / T = 0.01$ to $\tau / T = 5$ where *T* is the total measurement time window.

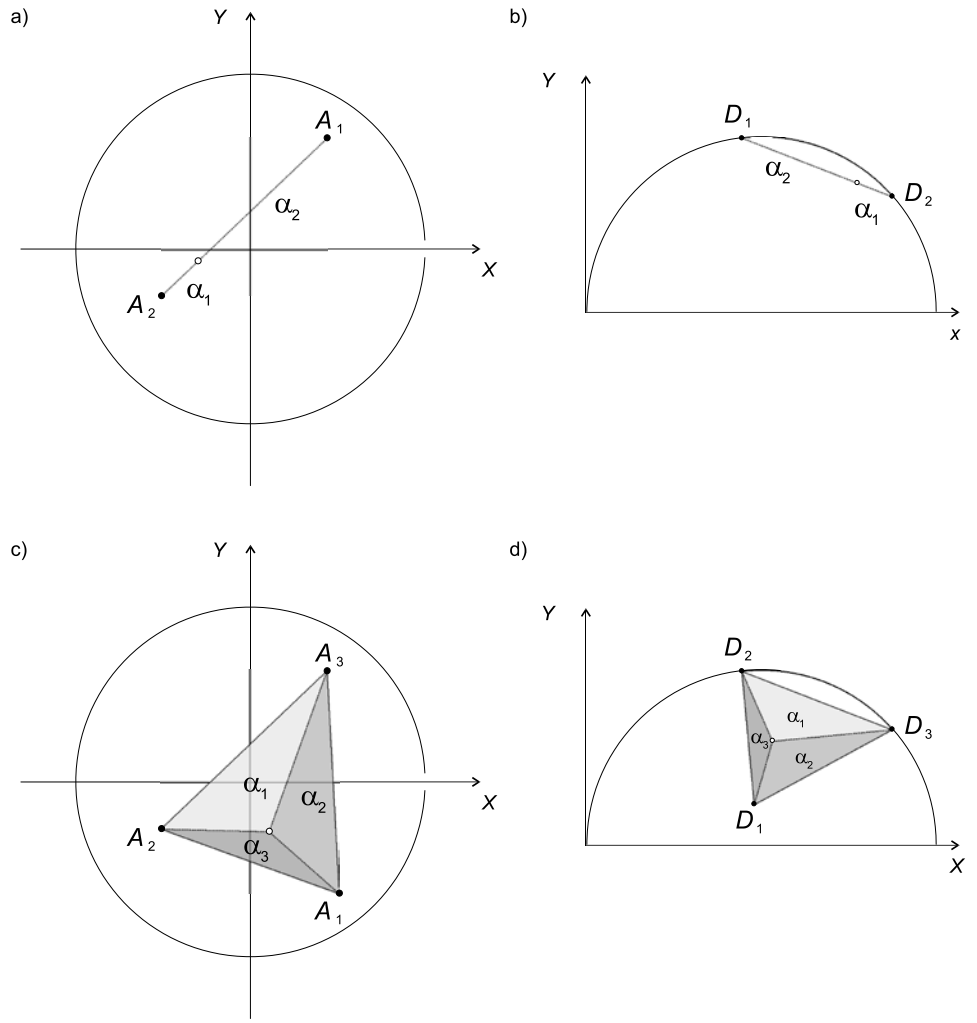

Fig. 2 The linear superposition of two components using a) temporal phasor and b) spectral phasor. For a three component system the linear superposition falls inside the triangle made up by the phasors of the pure components.

The phasors of artificial Gaussian shaped spectra with variable peak position k_0 and variable width *w* are shown in Fig. 1b Reference curves are shown for different numbers of spectral detection channels, *K*=8 and *K*=128. The phasor curves for zero width (w=0, corresponding to a delta function) show the maximum extent of the phasors. Non zero width spectra fall inside these curves. Importantly, phasors show a linear behavior. The phasor of a linear superposition of two spectra or decay curves is a linear superposition of the phasors of the pure components. This makes unmixing straightforward; the relative position of the phasor of a mixture with respect to the pure phasors yields the fractional intensities of each component. In a binary mixture the phasors fall on a line connecting the phasors of the pure components. The relative distance of the total phasor to the reference

points is determined by the fraction of that component. This is shown for both temporal and spectral phasor in Figs. 2a and 2b. In the case of a three component system, shown in Fig. 2c., the total phasor falls inside a triangle where the vertices are made up by the phasors of the pure components. The fractional intensities can be obtained by calculating the area spanned by the total phasor and two vertices and dividing this by the area of the triangle formed by the phasors of the pure components. Both spectral and temporal phasors have been used for unmixing. In temporal phasors unmixing of two components is straightforward and is realized by fitting a line through all phasor points; the intersections of the line with the reference semicircle yield the reference phasor points (lifetimes) of the pure components.

This, however, only works in the case of single exponential decays. Determining the reference points of multi-exponential decays is not possible in this way and the reference points need to be assigned manually. In the case of spectral phasors, the reference points can be estimated from the spectral image. First, the emission maxima of the pure components are estimated. This is accomplished by selecting regions in the phasor plot and showing the average spectra of the pixels that correspond to these regions. The average spectra show the emission maxima that can serve as reference values. Next, lines can be drawn in the phasor plot for the emission maxima and a range of spectral widths. By estimating straight lines through the phasor cloud, the position of suitable reference phasor points can be estimated. This is subject to errors when there are no pixels in the image with pure components and no unique triangle in the phasor cloud can be determined. In this paper we will introduce a new technique for finding the reference points in the phasor diagrams which is based on combining the information from lifetimes and spectra. The correlation between temporal and spectral phasor for a system with two and three components will be derived. This is the base for extracting all reference points, estimates of spectra and lifetimes and perform blind unmixing.

MATERIALS AND METHODS

Theory

Unmixing methods need a model to describe how different components are superimposed at the pixel level to estimate the fractional intensities and the pure spectra. In the absence of (interaction) effects such as solvatochromic shifts, linear superposition can be assumed. The normalized intensity *s* of a pixel with position index *j* in wavelength channel *n* and time bin *m* is related to the "fraction" α of fluorophore number *k* by:

$$s_{nmj} = \sum_k a_{nk} d_{mk} \alpha_{kj}. \qquad (1)$$

where a_{nk} and d_{mk} are the fractional contribution to the intensity of spectrum *k* at wavelength channel *n* and the decay *k* at time bin m respectively. The decays do not need to be single exponential and can take on any shape. Here, we assume the integrals of the

spectra (a_{n1}, a_{n2},…) and decay (d_{m1}, d_{m2},…) to be normalized to one. Therefore we can write:

$$s_{mj} = \sum_{n=0}^{N-1}\sum_{k} a_{nk} d_{mk} \alpha_{kj} = \sum_{k} d_{mk} \alpha_{kj}. \quad (2)$$

$$s_{nj} = \sum_{m=0}^{M-1}\sum_{k} a_{nk} d_{mk} \alpha_{kj} = \sum_{k} a_{nk} \alpha_{kj} \quad (3)$$

where N and M are the number of spectral channels and time gates respectively. The Fourier transformation of Eqs. 1-3 can be written as follow:

$$S_j^{AD} = \sum_{m=0}^{M-1}\sum_{n=0}^{N-1} s_{nmj} e^{i\frac{2\pi}{N}q(n+\frac{1}{2})} e^{i\frac{2\pi}{M}q(m+\frac{1}{2})} = \sum_{k} A_k D_k \alpha_{kj} \quad (4)$$

$$S_j^{A} = \sum_{n=0}^{N-1} s_{nj} e^{i\frac{2\pi}{N}q(n+\frac{1}{2})} = \sum_{k} A_k \alpha_{kj} \quad (5)$$

$$S_j^{D} = \sum_{m=0}^{M-1} s_{mj} e^{i\frac{2\pi}{M}q(m+\frac{1}{2})} = \sum_{k} D_k \alpha_{kj} \quad (6)$$

Where $A_k = \sum_{n=1}^{N} a_{nk} e^{i\frac{2\pi}{N}q(n+\frac{1}{2})}$ and $D_k = \sum_{m=1}^{M} d_{mk} e^{i\frac{2\pi}{M}q(m+\frac{1}{2})}$ are the discrete Fourier transforms of a_k and d_k, and q is the harmonic number. The Fourier transformation of Eq. 1 is basically a two dimensional transformation where one dimension is time and the other is wavelength.

For a case with two fluorophores Eqs. 4-6 are simplified to:

$$S_j^{AD} = A_1 D_1 \alpha_{1j} + A_2 D_2 (1-\alpha_{1j}) \quad (7)$$

$$S_j^{A} = A_1 \alpha_{1j} + A_2 (1-\alpha_{1j}) \quad (8)$$

$$S_j^{D} = D_1 \alpha_{1j} + D_2 (1-\alpha_{1j}) \quad (9)$$

We note that normalization requires that $\alpha_1 + \alpha_2 = 1$. Therefore α_2 can be replaced by $1 - \alpha_1$. For all pixels (different values of *j*) the phasors fall onto lines given by:

$$S_j^{AD} = u^{AD} + v^{AD} S_j^{A} \quad (10)$$

$$S_j^{D} = u^{D} + v^{D} S_j^{A} \quad (11)$$

where:

$$u^{AD} = \frac{A_1 D_1 - A_2 D_2}{A_1 - A_2}, \qquad v^{AD} = \frac{A_1 A_2 (D_2 - D_1)}{A_1 - A_2} \quad (12)$$

$$u^D = \frac{D_1 - D_2}{A_1 - A_2}, \qquad v^D = \frac{A_1 D_2 - A_2 D_1}{A_1 - A_2} \tag{13}$$

These Eqs. are valid for both the real and imaginary parts of the Fourier transformations.

Solving A_1, A_2, D_1, D_2 results in:

$$A_{1,2} = \frac{v^{AD} - u^D \pm \sqrt{\Delta}}{2v}, \qquad D_{1,2} = \frac{v^{AD} + u^D \pm \sqrt{\Delta}}{2} \tag{14}$$

where:

$$\Delta = \sqrt{(u^D)^2 - 2u^D v^D + (v^D)^2 + 4v^D u^{AD}} \tag{15}$$

The experimental analysis is performed by linear fitting of S_j^{AD} versus S_j^A and S_j^D versus S_j^A to estimate u^{AD}, v^{AD} and u^D, v^D respectively and solving Eqs. 14 and 15. After finding *A* and *D*, unmixing proceeds as follows:

$$\alpha_1 = \frac{S_j^D - D_2}{D_2 - D_1} \qquad or \qquad \alpha_1 = \frac{S_j^A - A_2}{A_2 - A_1} \tag{16}$$

This corresponds to the fractional distance of the phasor of the mixture to the pure phasor, see Fig.1. Interestingly, the spectra and decays of the pure components can be also calculated. This is achieved by generating the spectrally resolved temporal phasor and time resolved spectral phasors. This can be performed by :

$$S_m^A = \sum_{n=0}^{N-1} s_{nm} e^{i\frac{2\pi}{N}(n+\frac{1}{2})} / s_m = \sum_k A_k d_{mk} \alpha_k / \sum_k d_{mk} \alpha_k \tag{17}$$

$$S_n^D = \sum_{m=0}^{M-1} s_{nm} e^{i\frac{2\pi}{M}(m+\frac{1}{2})} / s_n = \sum_k D_k a_{nk} \alpha_k / \sum_k a_{nk} \alpha_k \tag{18}$$

S_m^A represents the time resolved spectral phasor; this is the Fourier transformation of the spectrum at time bin *m.* Similarly S_n^D represents the spectrally resolved temporal phasor which is the Fourier transformation of the decay at spectral channel *n.*

For a binary system the decays and spectra of the pure components can now be written as:

$$d_{m1,2} = \frac{S_m^A - A_{2,1}}{A_{2,1} - A_{1,2}} s_m \quad (19)$$

$$a_{n1,2} = \frac{S_n^D - D_{2,1}}{D_{2,1} - D_{1,2}} s_n \quad (20)$$

The pure decays (d_m) and spectra (a_n) can be found by simply multiplying the total decay s_m or spectrum s_n with the appropriate fractional intensity at each time bin (Eq. 19) or spectral channel (Eq. 20), respectively.

In the case of a three component system Eqs. 4-6 can be rewritten:

$$S_j^{AD} = A_1 D_1 \alpha_{1j} + A_2 D_2 \alpha_{2j} + A_3 D_3 (1 - \alpha_{1j} - \alpha_{2j}) \quad (21)$$

$$S_j^A = A_1 \alpha_{1j} + A_2 \alpha_{2j} + A_3 (1 - \alpha_{1j} - \alpha_{2j}) \quad (22)$$

$$S_j^D = D_1 \alpha_{1j} + D_2 \alpha_{2j} + D_3 (1 - \alpha_{1j} - \alpha_{2j}) \quad (23)$$

Normalization allows replacing α_3 by1- $\alpha_1 - \alpha_2$. All pixels with different fractional intensities lie in 4 planes defined by:

$$S_{jx,y}^D = v_{x,y}^D S_{jx}^A + w_{x,y}^D S_{jy}^A + u_{x,y}^D \quad (24)$$

$$S_{jx,y}^{AD} = v_{x,y}^{AD} S_{jx}^A + w_{x,y}^{AD} S_{jy}^A + u_{x,y}^{AD} \quad (25)$$

Here the x and y indices correspond to the real and imaginary parts of the Fourier transformations. We define:

$$M(X,Y,Z) = X_1 Y_2 Z_3 - X_1 Y_3 Z_2 - X_2 Y_1 Z_3 + X_2 Y_3 Z_1 + X_3 Y_1 Z_2 - X_3 Y_2 Z_1 \quad (26)$$

Then *v, w* and *u* can be expressed as:

$$v_{x,y}^D = -\frac{M(T_{x,y}, A_y, 1)}{M(A_x, A_y, 1)} \quad w_{x,y}^D = -\frac{M(T_{x,y}, A_x, 1)}{M(A_x, A_y, 1)} \quad u_{x,y}^D = \frac{M(T_{x,y}, A_x, A_y)}{M(A_x, A_y, 1)} \quad (27)$$

$$v_{x,y}^{AD} = -\frac{M(T_{x,y}A_{x,y}, A_y, 1)}{M(A_x, A_y, 1)} \quad w_{x,y}^{AD} = -\frac{M(T_{x,y}A_{x,y}, A_x, 1)}{M(A_x, A_y, 1)} \quad u_{x,y}^{AD} = \frac{M(T_{x,y}A_{x,y}, A_x, A_y)}{M(A_x, A_y, 1)} \quad (28)$$

The unmixing of 3 components relies on minimization of $\frac{|v_{xy}^{D}S_{jx}^{D}+w_{xy}^{D}S_{jy}^{D}+u_{xy}^{D}-S_{jx,y}^{D}|}{\sqrt{(v_{xy}^{D})^{2}+(w_{xy}^{D})^{2}+1}}$ and $\frac{|v_{xy}^{AD}S_{jx}^{D}+w_{xy}^{AD}S_{jy}^{AD}+u_{xy}^{AD}-S_{jx,y}^{AD}|}{\sqrt{(v_{xy}^{AD})^{2}+(w_{xy}^{AD})^{2}+1}}$ and yields *v, w* and *u*. This procedure corresponds to fitting a plane through the experimental points. The reference points of the spectral and temporal phasors are related by:

$$D_{kx}=v_{x}^{D}A_{kx}+w_{x}^{D}A_{ky}+u_{x}^{D}\quad D_{ky}=v_{y}^{D}A_{kx}+w_{y}^{D}A_{ky}+u_{y}^{D} \tag{29}$$

$$A_{kx}D_{kx}=v_{x}^{AD}A_{kx}+w_{x}^{AD}A_{ky}+u_{x}^{AD}\quad A_{ky}D_{ky}=v_{y}^{AD}A_{kx}+w_{y}^{AD}A_{ky}+u_{y}^{AD} \tag{30}$$

Substituting the D_{kx} and D_{ky} from Eq. 26 into Eq. 27 yields:

$$\begin{aligned}&v_{x}^{D}A_{kx}{}^{2}+(u_{x}^{D}-v_{x}^{AD}+A_{ky}w_{x}^{D})A_{kx}-(u_{x}^{AD}A_{ky}w_{x}^{AD})=0\\&w_{y}^{D}A_{ky}{}^{2}+(u_{y}^{D}-w_{y}^{AD}+A_{kx}v_{x}^{D})A_{ky}-(u_{y}^{AD}A_{kx}v_{y}^{AD})=0\end{aligned} \tag{31}$$

which can be solved numerically once *v, w* and *u* are known. The fractional intensities can be found from the spectral phasor or temporal phasor. These can be calculated from the areas in the phasor diagram, see Fig. 2. The area (*T*) of a triangle with vertices C_1, C2 and C_3 can be calculated by:

$$T(C_1,C_2,C_3)=\frac{1}{2}\left(C_{1x}C_{2y}-C_{1y}C_{2x}-C_{1x}C_{3y}+C_{1y}C_{3x}+C_{2x}C_{3y}-C_{2y}C_{3x}\right) \tag{32}$$

Using this, the fractional intensities as derived from the spectral phasor plot are:

$$\alpha_{1j}=\frac{T(A_2,A_3,S_j^{A})}{T(A_1,A_2,A_3)}\quad \alpha_{2j}=\frac{T(A_1,A_3,S_j^{A})}{T(A_1,A_2,A_3)} \tag{33}$$

And from the temporal phasor:

$$\alpha_{1j}=\frac{T(D_2,D_3,S_j^{D})}{T(D_1,D_2,D_3)}\quad \alpha_{2j}=\frac{T(D_1,D_3,S_j^{D})}{T(D_1,D_2,D_3)} \tag{34}$$

The pure decays and spectra are found from:

$$d_{m1}=\frac{T(A_2,A_3,S_m^{A})}{T(A_1,A_2,A_3)}s_m\quad d_{m2}=\frac{T(A_1,A_3,S_m^{A})}{T(A_1,A_2,A_3)}s_m\quad d_{m3}=\frac{T(A_1,A_2,S_m^{A})}{T(A_1,A_2,A_3)}s_m \tag{35}$$

$$a_{n1} = \frac{T(D_2, D_3, S_n^D)}{T(D_1, D_2, D_3)} s_n \quad a_{n2} = \frac{T(D_3, D_1, S_n^D)}{T(D_1, D_2, D_3)} s_n \quad a_{n3} = \frac{T(D_1, D_2, S_n^D)}{T(D_1, D_2, D_3)} s_n \tag{36}$$

Similar to the binary system the pure decays and spectra are found by multiplying the total decay spectrum with the appropriate fractional intensity at each time bin (or spectral channel).

Instrumental details

Two excitation sources were used for our experiments. A 473 nm solid-state diode laser (Becker & Hickl, BDL-473-SMC) with a pulse repetition rate of 80 MHz was used for single photon excitation experiments. In particular it was used for the simultaneous excitation of 2 fluorophores to validate the unmixing of binary systems.

A mode-locked Titanium:Sapphire (Ti:Sa) laser (Tsunami, Spectra-Physics, Sunnyvale, CA) tuned to 780 nm was used in the two-photon excitation experiments. It was employed to simultaneously excite three fluorophores in the test samples. The laser light is scanned in the XY direction using a galvanometer mirror scanner (040EF, LSK, Stallikon, Switzerland. The laser is focused into the sample by a microscope objective and the fluorescence emission is collected by the same objective lens. The results reported here are acquired using an infinity-corrected water-immersion objective (CFI Fluor 60xW, NA = 1.2, Nikon, Japan). The emission passes through a dichroic mirror (680 nm short pass or 490 nm long pass) and is filtered by a multiphoton emission filter (FF01-680/SP-25, Semrock, Rochester, NY, USA) when using the Ti:Sa laser and a 490 nm long pass filter when using the diode laser. The fluorescence is coupled into a 900 μm multimode fiber which is connected to a prism based spectrograph equipped with a multichannel PMT with 32 anodes of which only 7 anodes are used. The output of the PMT is amplified with a high bandwidth multi-channel amplifier (Philips scientific 774-s-50) and the amplified signals are connected to a multispectral lifetime imaging system (Lambda –Tau) described in chapter 5. The spectral width of each detection channel is about 20 nm and the time gates have a width of 200 ps. The 80 MHz repetition rate corresponds to a total time measurement window of 12.5 ns. All images shown here have a field of view of 60x60 μm^2 and the image size is 160x160 pixels. All experiments were carried out at room temperature.

The spectral images shown here are visualized using a real color visualization method. Briefly, the spectral information is used to assign an RGB value to each pixel that corresponds to the color as perceived by eye. To this end the spectra are multiplied by the wavelength dependent real-color RGB value and integrated over the spectral channels [14]. The temporal and spectral phasor plots are generated using homemade ImageJ plugins (plugins are available from http://www.Spechron.com/). The Fortran IMSL library was used for data fitting and root finding.

Sample details

1 mM aqueous solutions with pH=7 were prepared from Fluorescein (Sigma-Aldrich F6377), Alexa 532 (Invitrogen A-20001), Alexa 555 (Invitrogen A-20009) and Alexa 647 (Invitrogen A-20006). Imaging experiments on fixed cell were carried out using FluoCells prepared slide #2 (Invitrogen F-14781) and #6 (Invitrogen F-35925). Slide #2 contains bovine pulmonary artery endothelial cells (BPAEC). Here, Texas Red-X phalloidin is used for labelling F-actin, anti-bovine α-tubulin mouse monoclonal antibody in conjunction with BODIPY FL goat anti-mouse IgG antibody is used for labelling microtubules, and DAPI is used for labelling the nucleus. Slide #6 contains fixed muntjac skin fibroblast cells. Mitochondria are labelled with mouse anti-OxPhos Complex V inhibitor protein antibody and visualized using orange-fluorescent Alexa Fluor 555 goat anti–mouse IgG antibody. F-actin is labelled with green-fluorescent Alexa Fluor 488 phalloidin, and the nucleus is stained with TO-PRO-3 iodide. The plant leaf sample was freshly picked near the laboratory and immersed in water during the experiments to match the refractive index of the objective.

RESULTS

Unmixing of two components

In order to validate the unmixing method, separate images were recorded of Alexa 532 and Alexa 555 solutions. The Alexa 555 image contained a clear gradient in intensity and was added digitally to the approximately homogeneous Alexa 532 image. This approach is preferred over the use of synthetic images with added Poisson noise [13]. It yields images closely resembling images of real mixtures and allows the introduction of heterogeneities. Here, the Alexa 555 image was multiplied by a linear function that varies from 0 to 1 from left to right over the image. The images have 500 counts/pixel on average. Fig. 3 shows the images, decay curves and spectra after unmixing. The decay curve and the residual of the unmixed curve for Alexa 532 are shown in Fig. 3d. The lifetimes of both unmixed and original data are estimated by means of the Weber method [15]. This resulted in average lifetimes of 2.5 ns and 2.41 ns for the original and unmixed Alexa 532 respectively. The same approach resulted in lifetimes of 0.33 ns and 0.29 ns for the original and unmixed Alexa 555 respectively. The spectra from the original and unmixed data are in excellent agreement; this is demonstrated by the small residuals of both components, see Fig. 3(e, h). The average unmixed fraction of Alexa 532 in the digitally added image was calculated from the two original images and found to be 70.1%. This is in good agreement with the value of 69.3% found using the blind unmixing procedure.

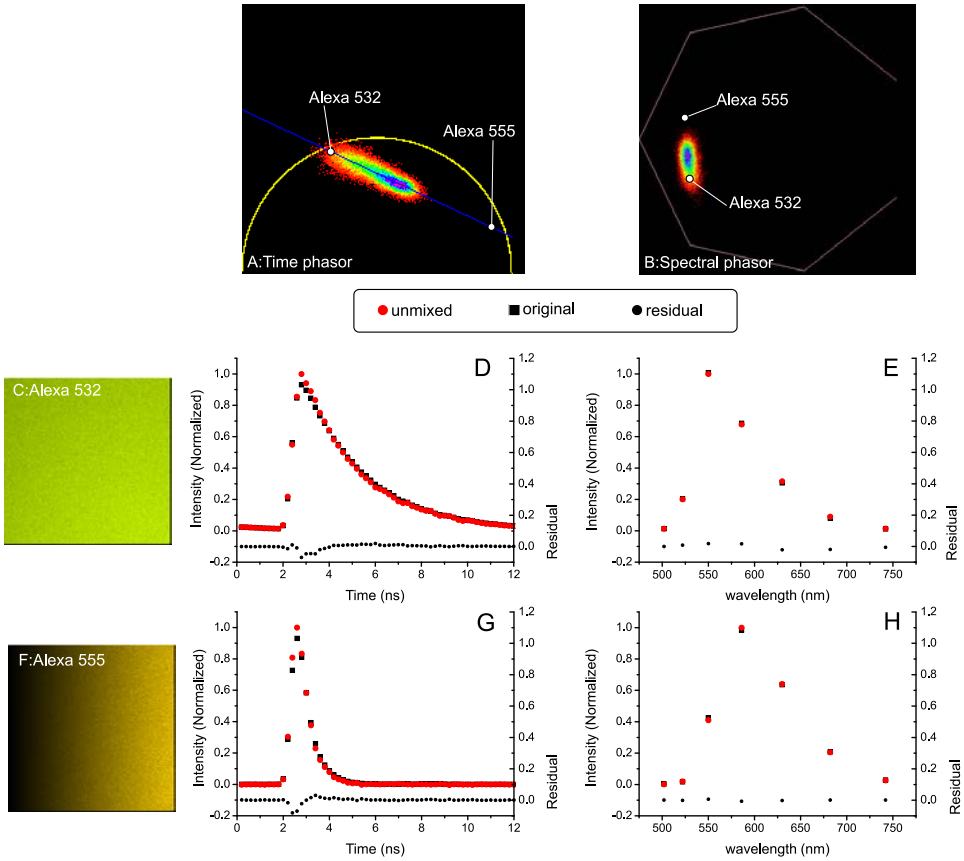

Fig. 3 Temporal (a) and Spectral (b) phasor plots of the Alexa 532 - Alexa 555 mixture image. The images (c, f), decays (d, g) and spectra from unmixed and original data are shown (e, h).

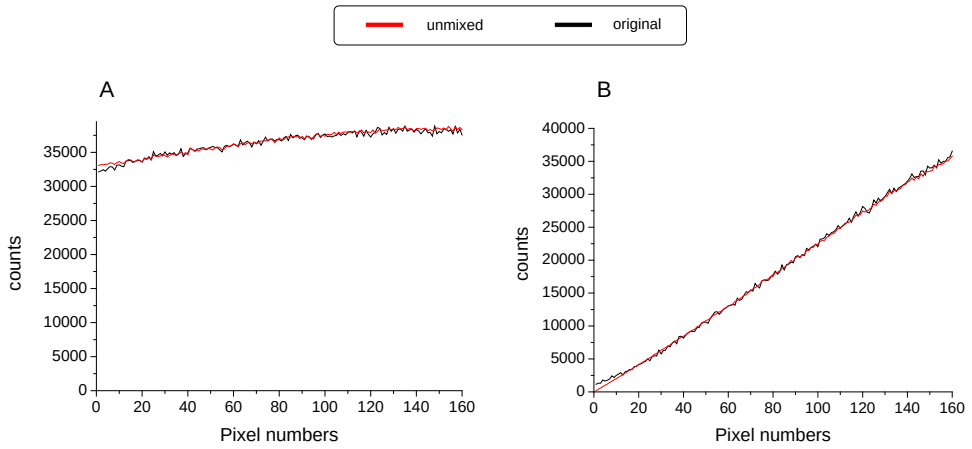

Fig. 4 The comparison between original and unmixed image intensity profile binned in y direction for (a) Alexa 532 and (b) Alexa 555.

Fig. 4 shows a comparison between two intensity traces in the original and unmixed Alexa 532 and Alexa 555 images. The pixels are binned in the y direction and the graph shows the total intensity in each pixel in the x direction. A very good overlap is observed for all pixels. Quantitative comparison of the Alexa 532 and Alexa 555 intensities in the original and unmixed images using the Manders [16]overlap coefficient yields coefficients of 0.994 and 0.992 respectively (see Table 1). This indicates good overlap between the original and unmixed images.

The temporal and spectral phasor diagrams are shown in Fig. 3 a and b respectively; the elongated shape of the phasors is characteristic for a two component system. The reference points for the phasors are indicated in both diagrams. The reference point for Alexa 555 falls outside the phasor clouds, indicating there is no pixel which includes pure Alexa 555 in the image. At the left side of the image the fraction of Alexa 532 is almost 100% and for that reasons the reference point of Alexa 532 falls inside the phasor cloud in both the temporal and spectral phasor diagrams. The two components can be unmixed when they show different lifetimes by employing the temporal phasor diagram. To this end a line is fitted through the phasor points and the intersections of the line with the reference phasor curve yields the lifetimes of the pure components (Fig. 3 a). In addition, the fractional intensities can be estimated from the distance between the phasor point and the intersections [13]. By applying this method to the synthetic image of Alexa 532 and Alexa 555, lifetimes of 2.8 ns and 0.15 ns for Alexa 532 and Alexa 555 are obtained respectively. The average fractional intensity for Alexa 532 is estimated at 63% which is different from the 69% found from the combined analysis. The difference is due to the fact that the fractional intensities are estimated based on the assumption that the reference points lie on the reference semicircle. The reference points calculated from the combined analysis fall on the fitted line but do not lie on the semicircle. The discrepancy between the positions of the reference points is explained by the multi-exponential decay of the dyes; only mono-exponential decays fall on the semicircle.

The combined analysis does not require the decays to be single exponentials; it works also with multi-exponential decays. We note that the emission maxima of Alexa 532 and Alexa 555 are separated by only 20 nm and the images contain only 500 counts/pixel on average. Nevertheless, good unmixing results are obtained. To test the method for the unmixing of three components, images of solutions of Fluorescein, Alexa 532 and Alexa 647 were recorded and added digitally.

Table 1. Summary of the unmixed and original data for the Alexa 532 - Alexa 555 image.

Component	$\tau_{original}$	$\tau_{unmixed}$	M
Alexa 532	2.5 ns	2.41 ns	99.4%
Alexa 555	0.33 ns	0.29 ns	99.2%

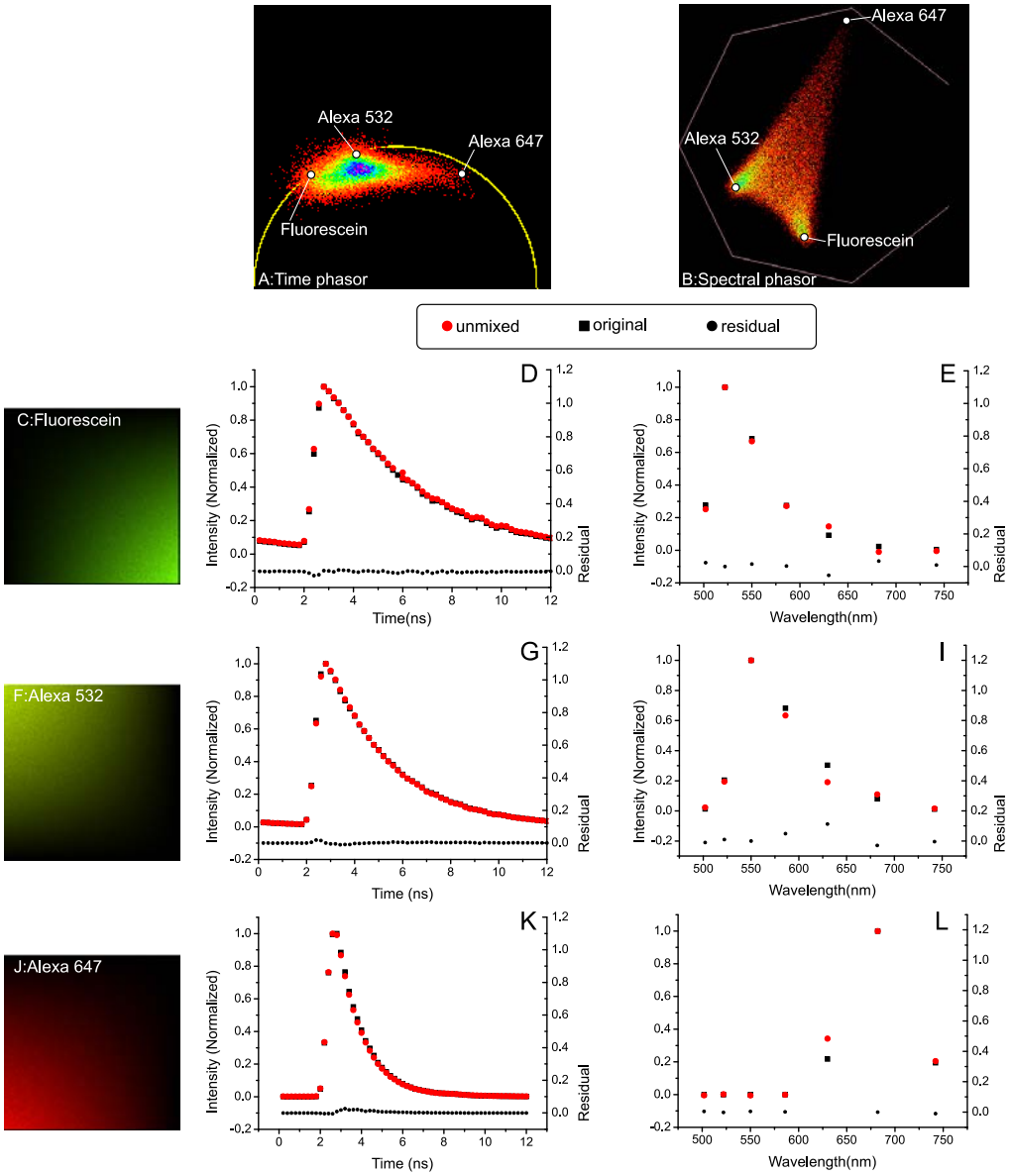

Fig. 5 Temporal (a) and spectral (b) phasors for the Fluorescein - Alexa 532 - Alexa 647 mixture image. Unmixed images (c,f and j), corresponding decays (d,g,k) and spectra from unmixing and original data are shown (e,i,l).

Synthetic intensity gradients were added to all images by multiplying a linear gradient that varies from 0 to 1, from bottom right to top left for Fluorescein, from top left to bottom right for Alexa 532 and from bottom left to top right for Alexa 647, see Fig. 5 (c, f and j). The reference spectra and decays are shown in Fig. 5(d, e) for Fluorescein, Fig.5(g, i) for Alexa 532 and Fig. 5 (k, l) for Alexa 647. The unmixed images for Fluorescein, Alexa 532 and

Alexa 647 are shown in Fig. 4c, Fig. 4f and Fig. 5g respectively. The average fractional intensities of Fluorescein, Alexa 532 and Alexa 647 in the original images amount to18.5%, 36.9% and 44.8% respectively. Blind unmixing of the digitally added images results in fractional intensities of 18.5%, 37.4%, and 44.2% respectively.

We previously reported the unmixing of three components using the spectral phasor approach [2].This was based on manually estimating the reference points based on the shape of the phasor cloud and drawing reference phasor lines based on the emission maximum of pure components. The temporal and spectral phasor clouds in Fig. 5(a, b) show a triangle with clear vertices. This is due to the fact that there are clear regions in the composed image that contain pure components from each dye. This is a comparatively simple unmixing problem and there is excellent agreement between the unmixed and input data. The average lifetimes of the original and unmixed dyes are found to be 3.85 ns and 3.84 ns for Fluorescein, 2.5ns and 2.46 ns for Alexa 532, and 1.02 ns and 0.99 ns for Alexa 647. The results for the lifetime estimations and Manders overlap coefficient are summarized in table 2. Unmixing using the spectral phasor diagram alone is complicated when there is a large overlap between the components and the vertices of the triangle are not clearly visible. We therefore carried out another, more demanding, unmixing experiment. Fig. 6 shows the spectral and temporal phasors for the Fluorescein - Alexa 532 - Alexa 647 mixture image which were added with more overlap. The spectral phasor cloud exhibits an irregular shape with some edges but in the temporal phasor no edges are observed. As expected from the increased overlap the phasor clouds are more condensed. The unmixing analysis results in estimated average fractions of 18.7%, 32.1% and 49.12% for Fluorescein, Alexa 532 and Alexa 647 respectively. This is in very reasonable agreement with the fractions of 18.5%, 36.9% and 44.8% for the original data. This example demonstrates that in spite of large overlap between different components in the image, the blind unmixing analysis performs well.

Table 2. Comparison between the unmixed and original data for the Fluorescein – Alexa 532 - Alexa 647 mixture image

Component	$\tau_{original}$	$\tau_{unmixed}$	M
Fluorescein	3.85 ns	3.84 ns	99.3%
Alexa 532	2.5 ns	2.46 ns	99.4%
Alexa 647	1.02 ns	0.99 ns	99.5%

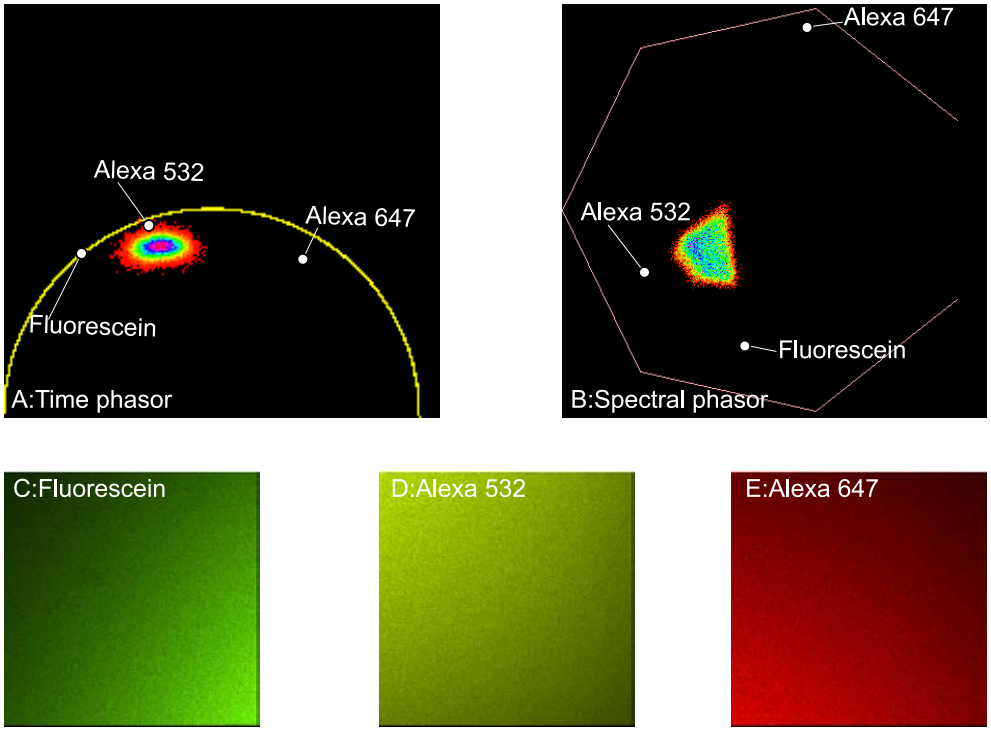

Fig. 6 Temporal (a) and spectral phasors (b) for the Fluorescein - Alexa 532 - Alexa 647 mixture image. The phasor cloud in the spectral domain shows some edges due to the limited number of spectral channels but in time domain the phasor cloud has no edges. The unmixed images are shown in c, d and e.

Unmixing of two components in labeled cells

Images of FluoCells prepared slide #6 were recorded and blind unmixed, see Fig. 7. The unmixed fractional intensity images, extracted decay curves and spectra are shown for both components. Visual inspection of the unmixed images suggests good separation of the signals of the two dyes. One of the components shows an emission maximum in the second spectral channel with a central wavelength of 522 nm and has an average fluorescence lifetime of 2.23 ns. This component corresponds to Alexa 488 used for staining the actin fibers in the specimen.The maximum emission wavelength of the second component is found in the 4^{th} spectral channel with a central wavelength of 586 nm and it has an average lifetime of 1.65 ns. This component corresponds to Alexa 555 used to label the mitochondria. The fraction of this component amounts to less than 3% of the total intensity in the image. This demonstrates the sensitivity of the method for resolving small fractions. We note that the average lifetimes of the two components are close which explains the small size of the phasor cloud in the time domain (Fig. 7b). In the spectral domain, however, the components are separated by almost 60 nm which results in the elongated shape of the phasor cloud in the spectral domain (Fig. 7c). The Alexa 555 overlaps with Alexa 488 everywhere in the image and for that reason there are almost no phasor point close to the phasor of pure Alexa 555.

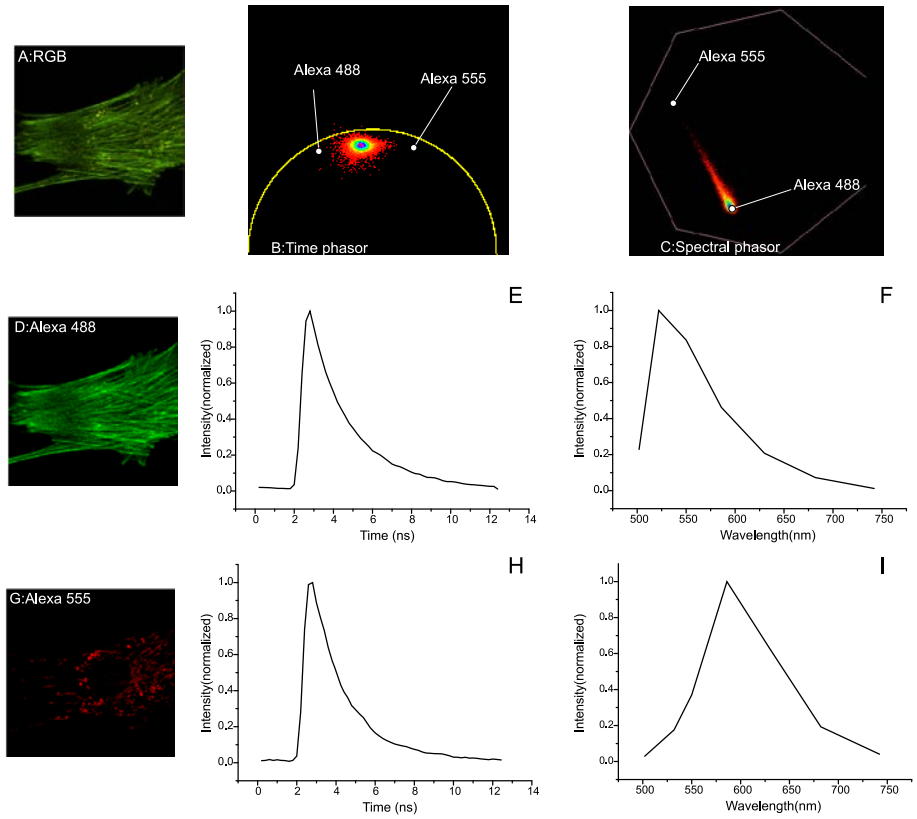

Fig. 7 The RGB image (a) and unmixed images (d, g) of FluoCells prepared slide #6. The temporal (b) and spectral phasors (c), estimated decays (e, h) and spectra (f, i) are shown.

Unmixing of three components in labeled cells

The image of the FluoCells prepared slide #2 was obtained by two-photon excitation imaging at an excitation wavelength of 780 nm. This enabled exciting all three dyes in the specimen simultaneously. The spectral range of the spectrograph was shifted to include the blue emission from DAPI. The RGB image, the unmixed components and extracted spectra and decays are shown in Fig. 8. Clear segmentation is achieved and the maximum emission wavelengths of DAPI, Bodipy and Texas red are measured at 457nm, 505nm and 636 nm respectively which is in accordance with the literature values of 461 nm, 505 nm and 620 nm [17]. We note that the average width of the spectral channels is 20 nm.The references temporal and spectral phasor of the pure dyes as obtained from the analyses are depicted in Fig. 8. Inspection of the reference points in the temporal phasor shows a comparatively short lifetime for DAPI and close lifetimes for BODIPY and Texas red.

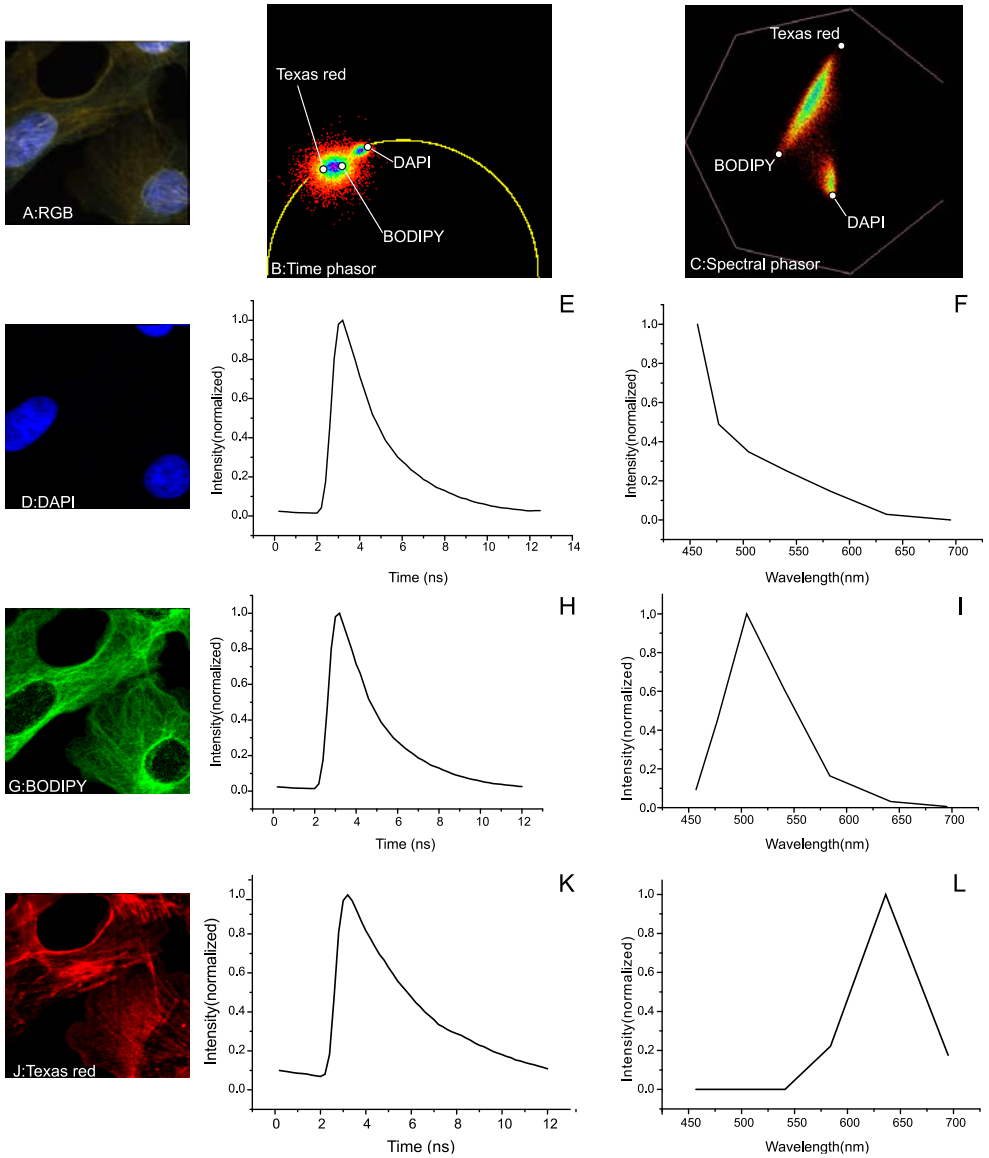

Fig.8 RGB image (a) and unmixed images (d, g, j) of FluoCells prepared slide #2). The temporal (b) and spectral phasors (c) and estimated decays (e, h, k) and spectra (f, I, l) are also shown.

CONCLUSION AND DISCUSSION

A novel phasor based method is introduced for blind unmixing of spectral lifetime images. The combined analysis of temporal and spectral phasors yields fractional intensities, spectra and decay curves for up to three fluorescent dyes without any prior knowledge about the fluorophores. The temporal and spectral phasors for a mixture of dyes are correlated and for a binary system we demonstrated a linear relationship between the spectral and temporal phasors. This can be extended to a system with three fluorophores.

In this case the phasors with different fractional intensities behave linearly and lie in a plane.

Using a phasor approach considerably simplifies the unmixing process. By converting the spectra and decay curves into phasors and plotting the phasors of all pixels in 2D diagrams, the unmixing process is reduced to finding the reference points of the pure dyes in the phasor plot and a linear interpolation. Both the real and imaginary parts of the Fourier transforms show the linear and planar relationships between the phasor points. For unmixing a sample with only two components only the real or the imaginary part of the phasors are required.

For a sample with three components all the phasor points fall in a plane. In this case we use both the real and imaginary parts of the spectral phasors as *x* and *y* coordinates and the real and imaginary parts of time and spectral-time phasors as *z*.

We note that we only use the first harmonic of the Fourier transform because it has the highest amplitude and is therefore least sensitive to noise. A very important feature of this method is that it does not need the decay curves to be single exponential, multi exponential decays can be analysed and used in the unmixing as well.

Generalization of the method to a higher number of components is feasible but requires the employment of higher harmonics to relate the different Fourier transformations. Visualizing the phasors of more than three components is not trivial and requires a 3D representation to visualize the cloud of phasor points. However, compared to SPA the reference points are not estimated manually from the phasor cloud and visualization in 3-D has less importance.

The blind unmixing method presented here is a global method; lifetimes and spectra are assumed to be invariant in the image. This enhances the estimation accuracy considerably due to employment of all photons in the image. All the pixels take part in the unmixing process which yields superior results even in presence of components with low fractional intensities. In one of the examples presented here, a component with a contribution of less than 3% to the image is well resolved.

The assumption of invariant lifetimes and spectra is not valid in all cases. For instance, in FRET experiments the lifetime of the donor dye may vary from pixel to pixel which is not compatible with our unmixing method.

We assume the fluorescence lifetime to be invariant over the whole spectral range. This is a good approximation in many cases. The fluorescence lifetime usually shows picosecond variations over the spectrum due to the effects of internal conversion. Such small variations, however, hardly influences the unmixing accuracy. Even small lifetime changes

of Alexa 647 over the spectrum hardly affect the unmixing process. In spite of this the fractional intensities could be estimated with high accuracy.

The reference points for a two component system can be found analytically. This simplifies the unmixing procedure and reduces the total time required for unmixing, extracting the fractional intensity maps, decay curves and spectra. This whole procedure takes less than 5 seconds for a 160x160 pixel spectral lifetime image. When more components are present the reference points cannot be found analytically any longer and numerical methods have to be used. Using FORTRAN IMSL functions for solving the equations numerically slightly increases the total time for unmixing to 6 seconds. Optimization of the code and implementing multi-threading should significantly speed up the unmixing.

Finally, the phasor based unmixing of spectral lifetime images is a fast and robust technique. It does not require any prior knowledge and it provides information about the spectra, decay curves and fractional intensities of the components.

REFERENCES

1. T. Zimmermann, "Spectral imaging and linear unmixing in light microscopy," Microscopy Techniques 1308-1310 (2005).

2. F. Fereidouni, A. N. Bader, and H. C. Gerritsen, "Spectral phasor analysis allows rapid and reliable unmixing of fluorescence microscopy spectral images," Optics Express **20,** 12729-12741 (2012).

3. R. A. Neher, M. Mitkovski, F. Kirchhoff, E. Neher, F. J. Theis, and A. Zeug, "Blind source separation techniques for the decomposition of multiply labeled fluorescence images," Biophys. J. **96,** 3791-3800 (2009).

4. I. Jolliffe, *Principal component analysis* (Wiley Online Library, 2005).

5. D. Chorvat Jr, J. Kirchnerova, M. Cagalinec, J. Smolka, A. Mateasik, and A. Chorvatova, "Spectral unmixing of flavin autofluorescence components in cardiac myocytes," Biophys. J. **89,** L55 (2005).

6. P. Pande, B. E. Applegate, and J. A. Jo, "Application of non-negative matrix factorization to multispectral FLIM data analysis," Biomedical Optics Express **3,** 2244-2262 (2012).

7. H. Shirakawa and S. Miyazaki, "Blind spectral decomposition of single-cell fluorescence by parallel factor analysis," Biophys. J. **86,** 1739-1752 (2004).

8. S. Schlachter, S. Schwedler, A. Esposito, G. Kaminski Schierle, G. Moggridge, and C. Kaminski, "A method to unmix multiple fluorophores in microscopy images with minimal a priori information," Optics Express **17,** 22747-22760 (2009).

9. H. D. Vishwasrao, A. A. Heikal, K. A. Kasischke, and W. W. Webb, "Conformational dependence of intracellular NADH on metabolic state revealed by associated fluorescence anisotropy," J. Biol. Chem. **280,** 25119-25126 (2005).

10. J. A. Palero, A. N. Bader, H. S. de Bruijn, A. P. van den Heuvel, H. J. C. M. Sterenborg, and H. C. Gerritsen, "In vivo monitoring of protein-bound and free NADH during ischemia by nonlinear spectral imaging microscopy," Biomedical optics express **2,** 1030-1039 (2011).

11. Q. Hanley and A. Clayton, "AB-plot assisted determination of fluorophore mixtures in a fluorescence lifetime microscope using spectra or quenchers," J. Microsc. **218,** 62-67 (2005).

12. Y. C. CHEN and R. Clegg, "Spectral resolution in conjunction with polar plots improves the accuracy and reliability of FLIM measurements and estimates of FRET efficiency," J. Microsc. **244,** 21-37 (2011).

13. F. Fereidouni, A. Esposito, G. Blab, and H. Gerritsen, "A modified phasor approach for analyzing time-gated fluorescence lifetime images," J. Microsc. **244,** 248-258 (2011).

14. J. A. Palero and H. S. De Bruijn, "Spectrally resolved multiphoton imaging of in vivo and excised mouse skin tissues," Biophys. J. **93,** 992 (2007).

15. S. Schlachter, A. Elder, A. Esposito, G. Kaminski, J. Frank, L. Van Geest, and C. Kaminski, "mhFLIM: resolution of heterogeneous fluorescence decays in widefield lifetime microscopy," Optics express **17,** 1557-1570 (2009).

16. E. Manders, F. Verbeek, and I. Aten, "Measurement of co-localization of objects in dual-colour confocal images," J. Microsc. **169,** 375-375 (1993).

17. F. Bestvater, E. Spiess, G. Stobrawa, M. Hacker, T. Feurer, T. Porwol, U. Berchner-Pfannschmidt, C. Wotzlaw, and H. Acker, "Two-photon fluorescence absorption and emission spectra of dyes relevant for cell imaging," J. Microsc. **208,** 108-115 (2002).

7

Quantitative FRET estimation by spectrally resolved lifetime imaging

INTRODUCTION

Förster Resonance Energy Transfer (FRET) refers to the transfer of excited state energy between two fluorophores that exhibit spectral overlap and are in close proximity, up to ~10 nm, to each other [1]. Upon excitation, the donor molecule transfers its energy via a non-radiative dipole-dipole interaction to an adjacent acceptor molecule. The energy transfer results in shortening of the donor lifetime and intensity decrease. In contrast both the acceptor intensity and average lifetime increases. For a given spectral overlap and transition dipole orientations, the decrease in intensity and lifetime is a measure of the distance between the two chromospheres. The sensitivity of FRET to distance variations is high and it has been successfully employed as a 'molecular ruler' to measure distance in the 1-10 nm range [1]. FRET has been successfully used to overcome the spatial resolution limitations of optical microscopes and monitor the interactions of molecules. FRET imaging is at present the technique of choice to visualize molecular interactions in cells [2].

Different approaches have been investigated to estimate the FRET efficiency, including donor lifetime measurements [3], donor or acceptor photo bleaching [4,5] and spectral ratio methods [6]. An excellent overview of the different approaches can be found in reference "[7]". Among these methods, fluorescence lifetime measurements of the donor molecule have been extensively used to estimate the proportion of transferred energy to the acceptor molecule. This is preferred over fluorescence lifetime measurements of the acceptor due to comparatively simple behavior of the donor. Studying the acceptor behavior is more complicated and has been investigated in several studies [8,9]. Including the whole spectral range in the FRET analyses, and thus information of both donor and acceptor, offers the prospect of more accurate and detailed information about the system. Spectrally resolved fluorescence lifetime imaging methods have been employed for the analyses of FRET. It has been shown that simultaneous monitoring of both donor and acceptor enhances the sensitivity of FRET measurements [10]. This is expected since more photons are collected compared to approaches where only the donor or acceptor is monitored.

A spectrally resolved frequency domain fluorescence lifetime imaging system has been used to study FRET [11] in a multi-fluorophore system. Here, it turned out to be possible to discriminate between situations where all or some of the fluorophores are interacting. In another application the employment of a spectrally resolved lifetime imaging system has been used to estimate the FRET efficiency in a system with a mixture of interacting (FRET) and non-interacting donor molecules. It was proven that the FRET estimation accuracy goes up when the information from all spectral channels is used [12].

In this chapter we introduce a method to extract the FRET efficiency by simultaneous analysis of the signal from all spectral channels. This method is based on phasor approach which simplifies the study of acceptor behavior. We have tested the method with

fluorescently labeled DNA and we demonstrate the possibility of extraction of FRET efficiency in presence of non-interacting and interacting donor molecules.

MATERIALS AND METHODS

Theory

Upon excitation of a binary system of donor and acceptor molecules, both can relax to the ground state via radiative and non radiative decays. The donor, however, can exhibit another decay process when it is in close proximity of an acceptor; it can transfer its excited state energy via a long-range dipole-dipole interaction to the acceptor molecule. This results in de-excitation of the donor and excitation of the acceptor. The donor serves as an excitation source that promotes the acceptor molecule to the excited state. This source has a complex temporal profile dictated by the decay kinetics of the system.

The donor kinetics can be described by:

$$\frac{d}{dt}D(t) = \sigma_D I(t) - \frac{D(t)}{\tau_D} - \frac{k}{\tau_D}D(t) \qquad (1)$$

Where $D(t)$ is the number density of donor molecules at time *t* , σ_D is the absorption cross section of the donor, $I(t)$ is the temporal excitation profile of the excitation source, τ_D is the donor lifetime without acceptor, and *k* is the energy transfer efficiency. The latter depends on the spectral overlap between donor emission and acceptor excitation spectra, donor and acceptor transition dipole orientations and, importantly, the distance between the donor and the acceptor. The energy transfer efficiency is defined by $k = \left(R_0 / R\right)^6$ where R_0 is the distance where the energy transfer efficiency is 50%. The acceptor can be excited directly by the laser pulse and by energy transfer from the donor:

$$\frac{d}{dt}A(t) = \sigma_A I(t) - \frac{A(t)}{\tau_A} + \frac{k}{\tau_D}D(t) \qquad (2)$$

Note the difference in the sign for the term containing the transfer rate in Eq. 1 and Eq. 2. Solving the rate equations for the donor yields the number of donor molecules in the excited state time *t*:

$$D(t) = \sigma_D I(t) * e^{-\frac{t}{\tau_D}(1+k)} = \sigma_D I(t) * e^{-\frac{t}{\tau_{DA}}} \qquad (3)$$

Where $*$ denotes the convolution operator. τ_{DA} is the shortened lifetime of the donor in presence of the acceptor and is defined by: $\tau_{DA} = \frac{\tau_D}{\left(1+k\right)}$.

The acceptor can be directly excited by the excitation source and in addition the donor can act as a second excitation source. Now, the acceptor kinetics is determined by the convolution of the exponential acceptor decay with the sum of the excitation source profile and the donor decay profile:

$$\begin{aligned} A(t) &= \sigma_A I(t) * e^{-\frac{t}{\tau_A}} + \left(\frac{k}{\tau_D} \sigma_D I(t) * e^{\frac{-t}{\tau_{DA}}} \right) * e^{-\frac{t}{\tau_A}} \\ &= \sigma_A I(t) * e^{-\frac{t}{\tau_A}} + \frac{k\sigma_D \tau_A}{\tau_A - \tau_D + k\tau_A} \left(e^{-\frac{t}{\tau_A}} - e^{-\frac{t}{\tau_{DA}}} \right) \end{aligned} \quad (4)$$

Both the fluorescence of the donor and the acceptor are wavelength dependent. This can be incorporated by multiplying equations (3) and (4) by the spectrally resolved transition rates:

$$f_D(t,\lambda) = D(t)\gamma_D a_D(\lambda) I(t) * e^{-\frac{t}{\tau_{DA}}} \quad (5)$$

γ_D is the transition rate for the donor and $a_D(\lambda)$ normalized emission profile of donor. Similarly we can write for the acceptor:

$$f_A(t,\lambda) = A(t)\gamma_A a_A(\lambda) = \sigma_A \gamma_A a_A(\lambda) I(t) * e^{-\frac{t}{\tau_A}} + \frac{k\sigma_D \tau_A}{\tau_A - \tau_D + k\tau_A} \gamma_A a_A(\lambda) I(t) * \left(e^{-\frac{t}{\tau_A}} - e^{-\frac{t}{\tau_{DA}}} \right) \quad (6)$$

Where again γ_A is the transition rate for the acceptor and $a_A(\lambda)$ the emission profile of the acceptor. Adding the equations 5 and 6 and replacing γ with Q/τ, where Q is the quantum efficiency, yields the full description of the time and wavelength dependent fluorescence emission:

$$\begin{aligned} f(t,\lambda) = &\left(\sigma_D \frac{Q_D}{\tau_D} a_D(\lambda) - \frac{k\sigma_D}{\tau_A - \tau_D + k\tau_A} Q_A a_A(\lambda) \right) I(t) * e^{-\frac{t}{\tau_{DA}}} + \\ &\left(\sigma_A \frac{Q_A}{\tau_A} a_A(\lambda) + \frac{k\sigma_D}{\tau_A - \tau_D + k\tau_A} Q_A a_A(\lambda) \right) I(t) * e^{-\frac{t}{\tau_A}}. \end{aligned} \quad (7)$$

This equation contains a linear superposition of donor and acceptor fluorescence. The second term between the brackets of the bottom part of the equation is responsible for the ingrowth of the acceptor signal; it is only observed in the acceptor signal because it is multiplied by the acceptor emission spectrum.

Both the lifetime reduction of the donor and the acceptor ingrowth provide valuable information about the FRET process and the donor - acceptor stoichiometry. This includes the ratio of donor to acceptor molecules exhibiting FRET and the number of donors and acceptors that are not involved in the energy transfer process.

The phasor based approach to analyze fluorescence lifetime images has recently become popular [13]. This is a graphical approach which provides an easy and fast way of analyzing lifetime images; a detailed description can be found in chapter2. Briefly, the real and imaginary parts of the first harmonic of the Fourier transform of the decay curve are used as coordinates in a scatter plot. The effect of the instrument response function on the fluorescence decay can be simply taken into account by either a rotation of the phasors over a fixed angle obtained from a reference measurement on a dye with a known lifetime or by direct measurement of the instrument response. The phasor approach can also be employed to analyze spectral images. The principle is similar to the lifetime phasor analyses and it is discussed in detail in chapter 3.

In Fourier theory the convolution of two functions is transformed into the product of the transforms of the individual functions, therefore the effect of the instrument response function can be removed by dividing the phasors by the instrument response function phasor. The linear superposition of the donor and acceptor appears as a line in the phasor diagram where the phasors from each spectral channel fall on a line connecting the acceptor phasor and donor phasor. The normalized phasors of the spectral lifetime channels are represented by:

$$F(\lambda)=\frac{\left(\sigma_D\frac{Q_D}{\tau_D}a_D(\lambda)-AQ_Aa_A(\lambda)\right)\frac{\tau_{DA}}{1-j\omega\tau_{DA}}+\left(\sigma_A\frac{Q_A}{\tau_A}a_A(\lambda)+AQ_Aa_A(\lambda)\right)\frac{\tau_A}{1-j\omega\tau_A}}{\left(\sigma_D\frac{Q_D}{\tau_D}a_D(\lambda)-AQ_Aa_A(\lambda)\right)\tau_{DA}+\left(\sigma_A\frac{Q_A}{\tau_A}a_A(\lambda)+AQ_Aa_A(\lambda)\right)\tau_A} \quad (8)$$

where we have used the phasor transformation $\frac{e^{-t/\tau}}{\tau} \xrightarrow{Phasor} \frac{1}{1-j\omega\tau}$ and $A = \frac{k\sigma_D}{\tau_A - \tau_D + k}$ denotes the ingrowth factor. Eq.(8) can be rewritten as:

$$F(\lambda) = \frac{\left(Q' \frac{a_D(\lambda)}{\tau_D} - Aa_A(\lambda)\right)\tau_{DA} r(\tau_{DA}) + \left(\sigma \frac{a_A(\lambda)}{\tau_A} + Aa_A(\lambda)\right)\tau_A r(\tau_A)}{\left(Q' \frac{a_D(\lambda)}{\tau_D} - Aa_A(\lambda)\right)\tau_{DA} + \left(\sigma \frac{a_A(\lambda)}{\tau_A} + Aa_A(\lambda)\right)\tau_A} \quad (9)$$

Where:

$$Q' = \frac{Q_D}{Q_A} \text{ and } A = \frac{k}{\tau_A - \tau_D + k\tau_A} \text{ and } r(\tau) = \frac{1}{1-j\omega\tau}$$

Equation 9 can be used to calculate the temporal phasors for different spectral channels of a system exhibiting FRET. Figure 1 shows a typical example of the phasor representation for a FRET experiments. In Fig.1a the FRET efficiency is equal to zero and the phasors from different spectral channels fall on a line extending from the pure donor phasor to the pure acceptor phasor. This is due to the linear superposition of donor and acceptor phasors and the varying ratio of the contributions of donor and acceptor with wavelength. Fig. 1b shows a situation where the FRET efficiency is not zero; again the phasors fall onto a line but now rotated with respect to the situation in Fig.1a and the intersection of the line with the reference circle determines the FRET efficiency. The phasor of the acceptor does not change when FRET takes place and by increasing the FRET efficiency all of the phasor points rotate along the phasor of the pure acceptor phasor, i.e. the phasor of the acceptor in the absence of FRET.

Due to the negative sign in front of A in Eq.9, the non-zero FRET efficiency phasors from the acceptor channels move outside the reference semicircle. The slope of the line is determined by the FRET efficiency, the position of phasor points on the line are correlated with the ratio of the absorption cross sections and quantum efficiencies of donor and acceptor molecules.

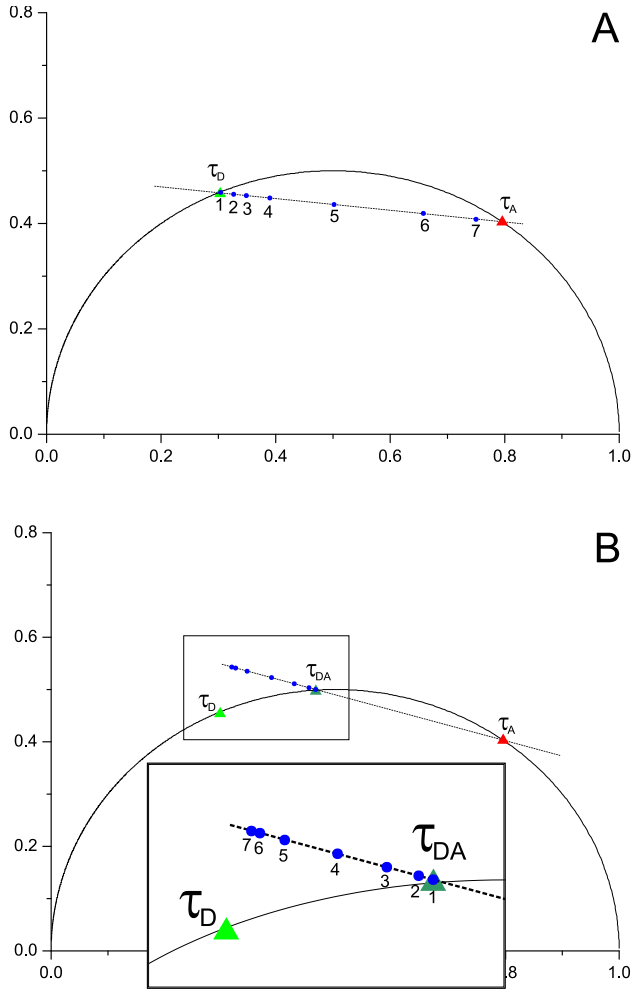

Fig 1. The spectrally resolved phasor for zero FRET efficiency (a) and non-zero FRET efficiency (b) measured with a spectrograph with 7 spectral channels. Numbers on the figure denotes the channel number.

Bi-exponential behaviour

In many cases the measured fluorescence decay curve is modeled as a mono-exponential function. Often, however, the fluorophores exhibit bi-exponential decays; therefore we consider a FRET system that exhibits bi-exponential decays for both the donor and the acceptor [14]. It is assumed that each component of the donor interacts independently with each acceptor component. In addition we assume that the donor components have the same spectral properties and we make the same assumption for the acceptor. This means that the spectral overlap and the energy transfer efficiency are constant for all possible combinations of donor and acceptor components. Then the Eq. 9 can be written as:

$$F(\lambda)=\frac{\sum_q\left(Q'\alpha_D^q\frac{a_D(\lambda)}{\tau_D^q}-A_{q,qq}a_A(\lambda)\right)\tau_{DA}^q r(\tau_{DA}^q)+\left(\sigma\alpha_A^q\frac{a_A(\lambda)}{\tau_A^q}+A_{qq,q}a_A(\lambda)\right)\tau_A^q r(\tau_A^q)}{\sum_q\left(Q'\alpha_D^q\frac{a_D(\lambda)}{\tau_D^q}-A_{q,qq}a_A(\lambda)\right)\tau_{DA}^q+\left(\sigma\alpha_A^q\frac{a_A(\lambda)}{\tau_A^q}+A_{qq,q}a_A(\lambda)\right)\tau_A^q} \quad (10)$$

Where

$$A_{q,qq}=\sum_{qq}\alpha_D^q\alpha_A^{qq}\frac{k}{\tau_A^{qq}-\tau_D^q+k\tau_A^{qq}}$$

q and *qq* run over the number of components and α_D and α_A are the fractional contributions of donor and acceptor lifetimes respectively. For a donor molecule with a single exponential decay the FRET trajectory falls on the reference semicircle but in the case of a bi-exponential decay, the FRET trajectory for the donor molecule is more complicated and expressed by:

$$r_f(E)=\alpha_D^1 r(\tau_D^1(1-E))+\alpha_D^2 r(\tau_D^2(1-E)) \quad (11)$$

where *E* is the FRET efficiency and $E=k/1+k$. A schematic view for a case when donor and acceptor show bi-exponential behaviour is shown in Fig.2.

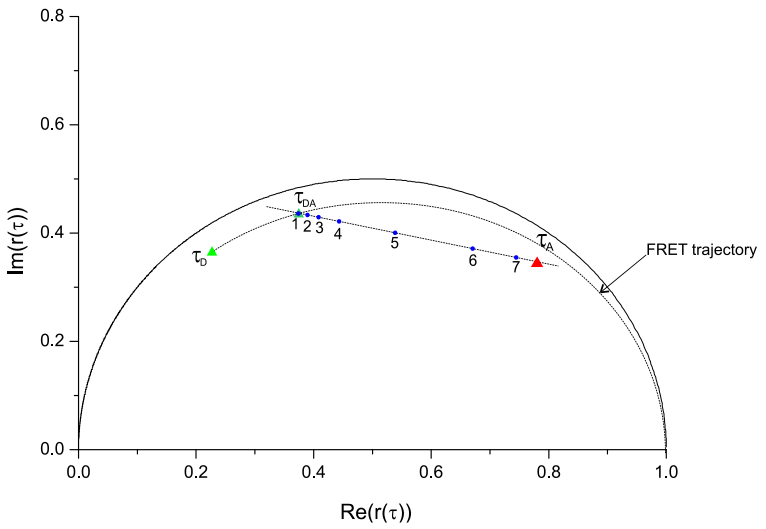

Fig 2. The spectrally resolved phasor for donor and acceptor wit bi-exponential decays. The FRET trajectory is determined by Eq.11.

Instrumental details

The FRET experiments are carried out using an inverted microscope equipped with a super continuum white light laser source operating at 80 MHz. The laser is tuned to 532 nm for exciting the Alexa 532 efficiently. The laser light is scanned in the XY direction using a galvanometer mirror scanner (040EF, LSK, Stallikon, Switzerland) and focused on the sample by a microscope objective. The fluorescence emission is collected by the same objective lens. The results reported here are acquired using an infinity-corrected water-immersion objective (CFI Fluor 60xW, NA = 1.2, Nikon, Japan). The emission passes through a dichroic mirror (532 nm long pass) and is filtered by an emission filter (532 nm long pass). Next, the fluorescence is coupled into a 900 μm multimode fiber which is connected to a prism based spectrograph equipped with a linear multichannel PMT with 32 anodes of which only 7 anodes are used. The output of the PMT is amplified with a 8 channel amplifier (Philips scientific 774-s-50). The amplified signals are connected to the multispectral lifetime detection system (Lambda –Tau) described in chapter 5. The spectral width of each channel is about 20 nm and the time bins of the Lambda-Tau detector are 200 ps wide. The 80 MHz repetition rate of the laser yields a 12.5ns total time measurement window. All experiments were carried out at room temperature and the size of the recorded images 160x160 pixels.

Sample details

The DNA samples were purchased from Invitrogen. 1 μM solution in 10X PBS buffer were prepared from donor (Alexa 532) and acceptor (Alexa 647) are labeled at the 5' end of the DNA with the complementary sequences of AAGCATGACCGCACAGAT and ATCTGTGCGGTCATGCTT respectively. The DNA oligomers were annealed slowly (5^0C/3 min) to for a well-defined double strand.

RESULTS

Fret efficiency estimation

Spectral lifetime images of fluorescently labeled DNA are recorded and analyzed. The lifetimes and fractions of acceptor and donor molecules are calculated using the Weber method [15]. This requires the recording of pure donor and acceptor decays in separate measurements. Fig.3 shows the phasors of the pure donor and acceptor molecules. As expected the phasors don't fall on the semicircle due to multi-exponential behavior of the dyes.The experimental phasors of different spectral channels of a DNA sample exhibiting FRET is shown in Fig. 3a. We note that the phasor from the 1^{st} channel is not shown here because of very low counts collected at this channel. The FRET trajectory for donor molecules is also indicated in the figure; it starts at the pure donor phasor for zero FRET efficiency and eventually ends up at the zero lifetime phasor for 100% FRET efficiency. The phasors of channels 2-4 mainly contain the signal from the donor molecules and fall on this FRET trajectory. Channels 5-6 are dominated by the acceptor signal and fall outside the reference semicircle due to the ingrowth term in the acceptor lifetime. The experimental phasor points are fitted to Eq.10 using Q, σ and k as fit parameter; the fitted points are

shown in Fig 2a. The fit yields a FRET efficiency *E* of 24.34±0.12%, ratio of quantum efficiencies Q_D/Q_A=1.13±0.055 and ratio of absorption cross sections σD/σA=57.5±5.

Fig.3b shows the phasors of a mixture containing 30% pure donor and 70% donor-acceptor DNA construct. The model was modified to take into account the presence of non-interacting (pure) donor by adding an additional term representing the phasor of pure donor with fraction of α :

$$F(\lambda)=\frac{\left(\sum_q\left(Q'\alpha_D^q\frac{a_D(\lambda)}{\tau_D^q}-A_{q,qq}a_A(\lambda)\right)\tau_{DA}^q r(\tau_{DA}^q)+\left(\sigma\alpha_A^q\frac{a_A(\lambda)}{\tau_A^q}+A_{qq,q}a_A(\lambda)\right)\tau_A^q r(\tau_A^q)\right)(1-\alpha)+\alpha\sum_q\left(Q'\alpha_D^q\frac{a_D(\lambda)}{\tau_D^q}\right)\tau_D^q r(\tau_D^q)}{\left(\sum_q\left(Q'\alpha_D^q\frac{a_D(\lambda)}{\tau_D^q}-A_{q,qq}a_A(\lambda)\right)\tau_{DA}^q+\left(\sigma\alpha_A^q\frac{a_A(\lambda)}{\tau_A^q}+A_{qq,q}a_A(\lambda)\right)\tau_A^q\right)(1-\alpha)+\alpha\sum_q\left(Q'\alpha_D^q\frac{a_D(\lambda)}{\tau_D^q}\right)\tau_D^q} \quad (12)$$

Fitting the experimental data to the modified Eq. 10 and employing the values of *Q* and σ from the previous fit yield the energy transfer efficiency k and the fraction of pure donor α. This fit yields a global FRET efficiency *E* of 25.7±0.49% and the fraction of pure donor is estimated to be 48.0±1.7% which corresponds to the fractional intensity of the pure donor molecule.

Fig. 4 shows the spectrally resolved FRET efficiency for the two samples. While the FRET efficiency stays constant over the whole spectral range for the sample with only DNA, the DNA – pure donor mixture shows a lower FRET efficiency at the first channels and then it goes up to about 23%. This behavior can be explained by the presence of the pure donor in the first channels; this reduces the average FRET efficiency by the presence of the pure donor lifetimes. As we move to the red part of spectrum, the signal from the donor molecule decreases (see Fig.5) and the FRET efficiency becomes less sensitive to the presence of the pure donor molecules and it approaches the true FRET efficiency of the DNA construct.

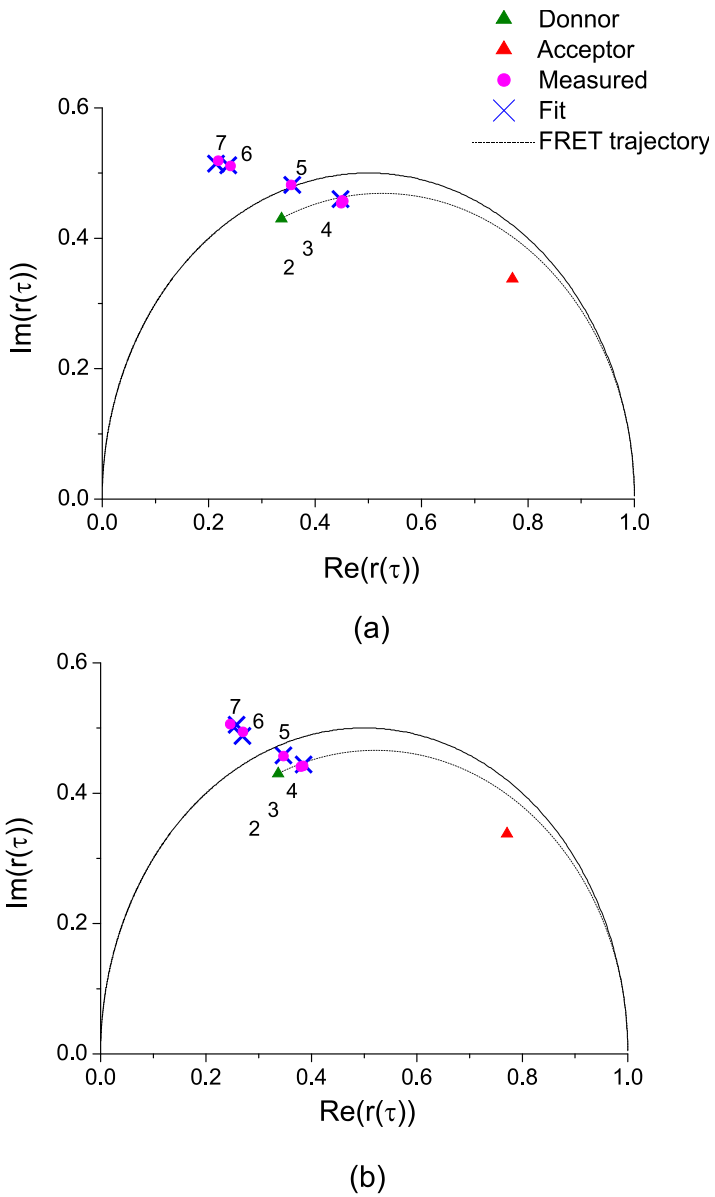

Fig 3. The spectrally resolved phasors from experiment and theory from (a) DNA sample and (b) mixture of pure donor and DNA sample.

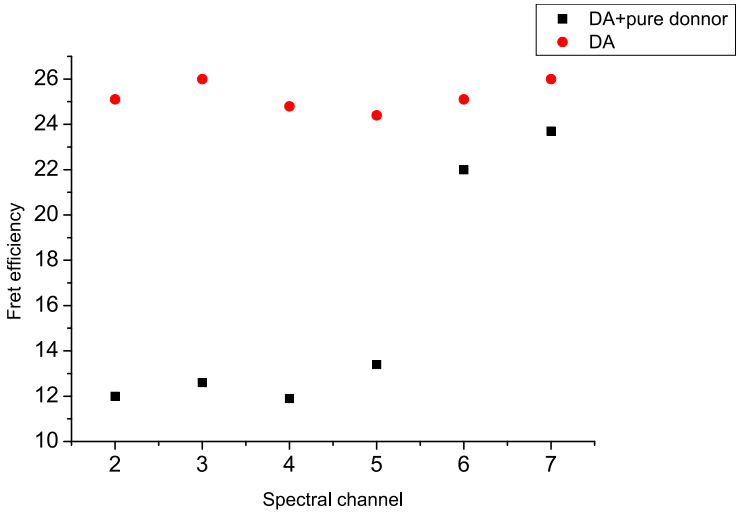

Fig 4. The spectrally resolved FRET efficiency for DNA sample and mixture of pure donor and DNA sample.

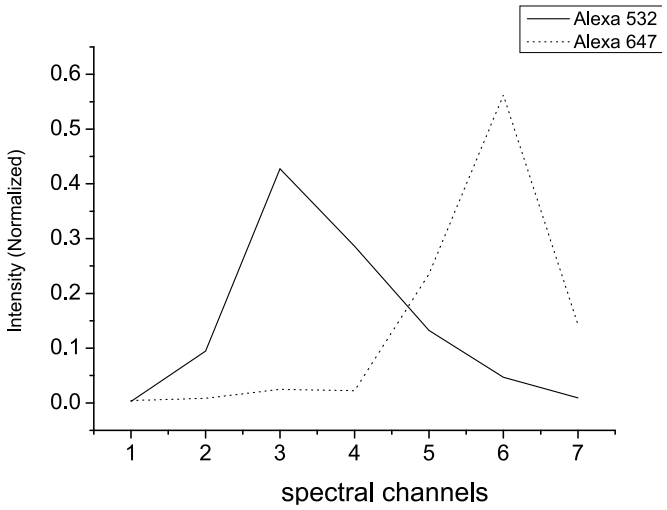

Fig. 5.The collected signal at each spectral channel from Alexa 532 and Alexa 647

CONCLUSION AND DISCUSSION

Resonance energy transfer has been extensively used as a ruler to estimate distances on a molecular scale and to study molecular interactions. So far the technique of choice to measure FRET has been fluorescence lifetime imaging. The donor fluorescence lifetime is

measured and used to obtain the FRET efficiency. This is a reliable technique but it requires comparatively high signals to realize accurate results. Current methods only use the donor channel to quantify FRET. Using the whole spectral range increases to amount of signal available for the analyses and can increase the accuracy of the FRET estimation.

We introduce a novel method for estimation of FRET efficiency using spectrally resolved fluorescence lifetime images in combination with phasor analyses. This method has the potential to considerably improve FRET measurements. It is shown that the phasors from all spectral channels fall on a line with the phasor of the pure acceptor as one of the end points. The intersection of this line with the reference phasor circle yields the FRET efficiency. The behavior of the acceptor fluorescence is complicated by the ingrowth of the fluorescence due to FRET. This is translated into a simple shift of the phasors on the line produced by the phasors from all spectral channels. The phasor analyses can take into account bi-exponential behavior of both donor and acceptor molecules. This yields modified, but well predictable, FRET trajectory. Phasor analyses of the experimental results for bi-exponentially decaying donors and acceptors are in good agreement with the predicted behavior.

The employment of spectrally resolved lifetime imaging systems can provide improved estimates of FRET efficiencies but also additional information about the specimen. The behavior of the spectrally resolved FRET efficiency provides information about the donor fraction involved in FRET. This was demonstrated using a sample consisting of a mixture of pure donor and DNA coupled donor - acceptor. The presence of low FRET efficiency in the donor channel compared to the acceptor channel is indicative of the presence of donors not involved in FRET. Using our phasor analyses the fraction of donors involved in FRET and the correct FRET efficiency are obtained.

Using our phasor approach reduces the estimation of the energy transfer efficiency to fitting the phasor points of all spectral channels to Eq. 10 with k, σ and Q as fit parameter. The fit not only provides the energy transfer efficiency, but also the ratio of the absorption cross sections and quantum efficiencies of donor and acceptor.

A small modification of Eq. 10 allows finding the fraction of donor molecules involved in FRET and further extensions are foreseen to retrieve additional information. Currently we are considering the possibility of studying systems consisting of donor molecules interacting with multiple acceptor molecules. This will show a higher FRET efficiency compared to a situation with only one donor and one acceptor and this is reflected in the relative position of the phasor point on the line. There are prospects to generalize the formalism to analyze arbitrary combinations of interacting and non-interacting donors and acceptors. However, resolving more parameters will in general reduce the accuracy of the fitted parameters. Currently we use only 7 spectral channels and more channels may be required for full analyses of arbitrary systems of donors and acceptors.

Follow up experiments are planned to further validate this novel FRET analyses method. Analyses of FRET imaging experiments on (living) cells to visualize molecular interactions are a logical next step. In addition further characterization of the analyses in terms of figures of merit as used in chapter 5 would be valuable to better understand the statistics, in particular the number of photons required for obtaining a certain accuracy in FRET efficiency.

REFERENCES

1. H. Wallrabe and A. Periasamy, "Imaging protein molecules using FRET and FLIM microscopy," Curr. Opin. Biotechnol. **16,** 19-27 (2005).

2. F. S. Wouters, "Imaging Molecular Physiology in Cells Using FRET-Based Fluorescent Nanosensors," Optical Fluorescence Microscopy 131-152 (2011).

3. H. Gerritsen, A. Agronskaia, A. Bader, and A. Esposito, "Time domain FLIM: Theory, instrumentation, and data analysis," Laboratory Techniques in Biochemistry and Molecular Biology **33,** 95-132 (2009).

4. A. Kinoshita, C. M. Whelan, C. J. Smith, I. Mikhailenko, G. W. Rebeck, D. K. Strickland, and B. T. Hyman, "Demonstration by fluorescence resonance energy transfer of two sites of interaction between the low-density lipoprotein receptor-related protein and the amyloid precursor protein: role of the intracellular adapter protein Fe65," The Journal of Neuroscience **21,** 8354-8361 (2001).

5. F. S. Wouters, P. I. H. Bastiaens, K. W. A. Wirtz, and T. M. Jovin, "FRET microscopy demonstrates molecular association of non-specific lipid transfer protein (nsL-TP) with fatty acid oxidation enzymes in peroxisomes," EMBO J. **17,** 7179-7189 (1998).

6. H. Chen, H. L. Puhl, S. V. Koushik, S. S. Vogel, and S. R. Ikeda, "Measurement of FRET efficiency and ratio of donor to acceptor concentration in living cells," Biophys. J. **91,** L39-L41 (2006).

7. C. Berney and G. Danuser, "FRET or no FRET: a quantitative comparison," Biophys. J. **84,** 3992-4010 (2003).

8. S. P. Laptenok, J. W. Borst, K. M. Mullen, I. H. M. van Stokkum, A. J. W. G. Visser, and H. van Amerongen, "Global analysis of Förster resonance energy transfer in live cells measured by fluorescence lifetime imaging microscopy exploiting the rise time of acceptor fluorescence," Physical Chemistry Chemical Physics **12,** 7593-7602 (2010).

9. C. Biskup, T. Zimmer, L. Kelbauskas, B. Hoffmann, N. Klöcker, W. Becker, A. Bergmann, and K. Benndorf, "Multi-dimensional fluorescence lifetime and FRET measurements," Microsc. Res. Tech. **70,** 442-451 (2007).

10. Y. C. CHEN and R. Clegg, "Spectral resolution in conjunction with polar plots improves the accuracy and reliability of FLIM measurements and estimates of FRET efficiency," J. Microsc. **244,** 21-37 (2011).

11. T. S. Forde and Q. S. Hanley, "Spectrally resolved frequency domain analysis of multi-fluorophore systems undergoing energy transfer," Appl. Spectrosc. **60,** 1442-1452 (2006).

12. D. Strat, F. Dolp, B. von Einem, C. Steinmetz, C. A. F. von Arnim, and A. Rueck, "Spectrally resolved fluorescence lifetime imaging microscopy: Förster resonant energy transfer global analysis with a one- and two-exponential donor model," J. Biomed. Opt. **16,** 026002-026002-19 (2011).

13. M. A. Digman, V. R. Caiolfa, M. Zamai, and E. Gratton, "The phasor approach to fluorescence lifetime imaging analysis," Biophys. J. **94,** L14-L16 (2008).

14. J. R. Lakowicz, *Principles of fluorescence spectroscopy* (Springer, 2006).

15. S. Schlachter, A. Elder, A. Esposito, G. Kaminski, J. Frank, L. Van Geest, and C. Kaminski, "mhFLIM: resolution of heterogeneous fluorescence decays in wide field lifetime microscopy," Optics express **17,** 1557-1570 (2009).

Summary

In microscopy, in addition to the intensity, other parameters such as the fluorescence emission spectrum and lifetime can be used for imaging. Importantly, the latter two techniques can also provide information about environmental parameters, help to identify biochemical compounds or visualize molecular interactions. Upon excitation of a fluorophore, the molecule stays in the excited state for a certain characteristic time, usually a few nanoseconds, and then relaxes back to the ground state. This characteristic time is called the fluorescence lifetime of the molecule.

The fluorescence decay curve and the emission spectrum of the chromophores can be spatially mapped using a standard microscope equipped with a time resolved detection system for lifetime imaging or spectrograph for spectral imaging. These techniques provide complementary and sometimes overlapping information. Simultaneous recording of spectra and lifetimes offers the prospect of obtaining more and more reliable information than with a single technique. To fully take advantage of this, novel instrumentation that is both robust and affordable is required.

In this thesis, I describe the development and application is described of a novel multi-channel detection method for spectrally resolved fluorescence lifetime imaging. This "Lambda-Tau" detector is based on an FPGA (Field-programmable gate array) equipped with 8 high speed transceivers to record complete decay curves at high count rates and high time resolution (200 ps). The multi-channel feature of the FPGA enables simultaneous recording of decay curves for each spectral channel and offers a powerful, scalable solution for spectrally resolved fluorescence lifetime imaging.

After acquiring the lambda-tau date, we also need reliable and efficient analysis algorithms to fully extract the potential of the instrument. These tools complement the hardware by converting the large amount of raw data into useful information on the state of the molecules in the sample. The analysis of lifetime data is much more complex than that of spectral domain data. This complication arises from the effect of the instrument response and differences in hardware configuration which may induce truncation and sampling artifacts in the measured decay curve. For analysis, a fast, graphical technique called the phasor approach is used, which reduces the spectra and decay curves to a complex values, or for representation into points in a 2D plot; the position of a phasor point is determined by its lifetime and spectral shape.

In chapter 2 where we introduce a generalized approach to life time measurements, which is based on the phasor method and it takes into account all effects related to time gate configurations, binning and truncation and we present an analytical expression for the phasor reference plot which is compatible with different gate configurations and widths of the measurement windows. Moreover, a global solution is provided to extract two lifetimes and fractional intensities in a binary mixture. A separability index is used to investigate the effect of gate widths on the accuracy of the estimated lifetimes and it is shown that the average number of counts required to separate two lifetimes in the phasor analysis is considerably lower than in conventional pixel by pixel analysis. The power of this method is demonstrated by examples recorded with a time gated detection system equipped with 4 time gates (LIMO).

One of the main goals of this research is to develop a complete analysis tools for Lambda-Tau imaging. Therefore, a novel technique for analysis of spectral images is developed. In Chapter 3, the spectral phasor approach (SPA) is developed to represent the hyper spectral images in a 2D phasor plot and it provides a solution for semi-blind unmixing using a fast, reliable, and simple algorithm. I developed an analytical solution for unmixing of three components. The value of this method is demonstrated by several examples including the unmixing of components in fluorescently labeled cells with three components and also the unmixing of an auto-fluorescence image of a grass blade. Although the representative images are recorded using a spectrograph equipped with 128 spectral channels, the compatibility of the method with lower number of spectral channels is also shown. The results from different hardware configurations are quantified and compared using the Manders overlap coefficient.

Practical application of this technique is demonstrated in chapter 4 with the analysis of two photon excited auto fluorescence and second harmonic generation images of in vivo human skin. Regions of interest on the phasor plot are back-projected onto the original image to highlight the regions with specific, similar spectral properties. This technique allows simple and fast segmentation. Different structures, including Stratum Corneum, epidermal cells, melanized cells, and dermis, can be discerned by applying this spectral phasor based segmentation.

Chapter 5 describes the hardware development of the Lambda-Tau system. It is equipped with 7 spectral channels and a variable number of time gates with a fixed 200 ps width. An error analysis was carried out to characterize the performance of both lifetime and spectral detection. The effect of gate width and spectral channel width on the accuracy of estimated lifetimes and spectral emission widths is described. The performance of the whole instrument is also evaluated to investigate the behavior of the system at different photon count rates. Correlation between results obtained in the time and spectral domains is demonstrated; the segmentation based on spectral and temporal phasor provides similar results.

Spectrally resolved lifetime imaging is much more than a method to simultaneously measure lifetimes and spectra. This method provides two dimensional data sets for each pixel and the capability of measuring lifetimes at different spectral channels and spectra at different time channels. Inclusion of the whole data set in the analyses can provide new and more detailed information and improve sensitivity. This is a described in chapter 6 where another novel technique is presented. Here I demonstrate the capability of combining two spectral and time domain data to unmix the principal components without any prior knowledge. The recorded spectral-lifetime images are analyzed to provide fractional intensities, spectra and decay curves of every single component. The accuracy of the method is tested by digitally adding single images to create binary and ternary images and comparing the unmixed results with original data. This method is also tested on fluorescently labeled cells with three different components.

Importantly, lifetime imaging has become the technique of choice to study molecular interactions. To this end two molecules, donor and acceptor, are fluorescently labeled with different, matched fluorophores. When the molecules are within 10 nm of each other Förster Resonance Energy Transfer (FRET) can take place which results in shortening of the donor fluorescence lifetime. This application turned lifetime imaging into a major tool for biological applications. FRET, however, also results in sensitized emission in the acceptor emission band. So, far combined analysis of the donor and acceptor has not been demonstrated in literature. Chapter 7 demonstrates the simultaneous FRET analysis of the signal from all spectral lifetime channels, covering both donor and acceptor emission. The method is tested on fluorescently labeled DNA. It was demonstrated that the FRET efficiency can be correctly extracted in the presence of a mixture of non-interacting and interacting donor molecules.

Samenvatting

In microscopie kunnen, naast intensiteit, ook het fluorescentie emissiespectrum en de fluorescentie vervaltijd gebruikt worden in afbeeldingen. De laatste twee kunnen informatie geven over omgevingsparameters, biochemische stoffen identificeren of moleculaire interacties visualiseren.

Na excitatie van een fluorescent molecuul blijft het molecuul een korte tijd in de aangeslagen toestand. De karakteristieke tijd die hiermee verbonden is, is de fluorescentie levensduur. De fluorescentielevensduur en het fluorescentie-emissie spectrum kunnen gebruikt worden in standaard microscopen die uitgerust zijn met een tijdsopgelost detectiesysteem voor “fluorescentielevensduur microscopie” of een spectrograaf voor “spectrale microscopie”. Deze technieken geven complementaire en soms overlappende informatie. Het simultaan opnemen van emissie spectra en levensduren geeft de mogelijkheid om meer en betrouwbaardere informatie te krijgen over het preparaat dan met afzonderlijke technieken. Om hier optimaal gebruik van te maken is nieuwe instrumentatie nodig die robuust, betrouwbaar en betaalbaar is.

In dit proefschrift worden de ontwikkeling en toepassing van een nieuwe meer-kanaals detectiemethode beschreven voor spectraal opgeloste fluorescentielevensduur microscopie. Deze “lambda-tau” detector is gebaseerd op een FPGA (Field Programmable Gate Array) uitgerust met 8 hoge snelheid transceivers waarmee hele vervalcurves opgenomen kunnen worden met korte acquisitietijden en hoge tijdsresolutie (200ps). Door de aanwezigheid van 8 transceivers kan voor meerdere spectrale kanalen gelijktijdig de vervalcurve opgenomen worden. Dit is een krachtige, schaalbare methode om spectraal opgeloste fluorescentielevensduur beelden op te nemen.

Om de volledige potentieel van deze methode te benutten zijn betrouwbare en efficiënte analyse algoritmen noodzakelijk. Deze algoritmen complementeren de hardware en zetten de grote hoeveelheid ruwe data om in zinnige informatie over de toestand van de fluorescente moleculen in het preparaat. De analyse van levensduur data is gecompliceerder dan die van spectrale data. Dit wordt vooral veroorzaakt door de eigenschappen van het gebruikte detectiesysteem; de reactietijd, het afkappen van de vervalcurve en de bemonstering kunnen artefacten introduceren die de analyse bemoeilijken. In dit proefschrift worden snelle grafische methoden, fasor methoden, gebruikt om de data te analyseren. Hier worden spectra en vervalcurven omgezet naar punten in een 2-D diagram. Spectra en vervalcurven met gelijke vorm zijn gegroepeerd terug te vinden in deze fasor diagrammen.

In hoofdstuk 2 wordt een algemene fasor methode voor fluorescentielevensduur microscopie geïntroduceerd. Er wordt een analytische uitdrukking voor de fasor referentie

kromme gegeven die alle effecten door configuratie van de (tijd) detectie vensters , tijds-interval en afkappen van de vervalcurve meeneemt. Verder wordt een 'globale' oplossing gepresenteerd voor het vinden van twee levensduren en hun fractionele intensiteiten in een binair mengsel van 2 fluorophoren. Een "scheidingsindex" wordt gebruikt om het effect van de breedte van de detectie vensters op de nauwkeurigheid van de levensduren te onderzoeken. Het resultaat laat zien dat er aanzienlijk minder signaal per beeldpunt nodig is dan in een klassieke pixel voor pixel benadering om een bepaalde nauwkeurigheid te realiseren. De methode wordt toegepast in een aantal voorbeelden opgenomen met een "time gated" detectiesysteem uitgevoerd met 4 tijds kanalen (LIMO).

Een belangrijk doel van dit onderzoek is om nieuwe analysemethoden te ontwikkelen voor Lambda-Tau microscopie. Dit was de motivatie om in hoofdstuk 3 een spectrale fasor methode (SPA) te ontwikkelen voor de analyse van hoge resolutie spectrale beelden (hyper spectrale beelden). Hier worden emissie spectra middels een omzetting gerepresenteerd als punten in een 2-D fasor plot. Dit is een snelle en betrouwbare methode die in staat is om, op basis van selectie van gebieden in de fasor plot, zonder extra informatie het signaal van verschillende kleurstoffen van elkaar te scheiden. De fasor methode is ook in staat om signalen volledig analytisch van elkaar te scheiden. In hoofdstuk 3 worden hier toepassingen van analyses gedemonstreerd van het scheiden van het signaal van 3 verschillende kleurstoffen in cellen en van autofluorescentie componenten in grassprieten. Hoewel deze beelden zijn opgenomen met een spectrograaf uitgerust met 128 golflengtekanalen, is de methode ook te gebruiken bij systemen met een laag aantal detectiekanalen. De resultaten opgenomen met verschillende aantallen kanalen zijn kwantitatief vergeleken met behulp van de Manders overlap coëfficiënt.

Een praktische toepassing van de spectrale fasor methode wordt beschreven in hoofdstuk 4; de analyse van twee foton excitatie autofluorescentie en tweede harmonische generatie in in-vivo humane huid. Geselecteerde gebieden in de fasor plot zijn terug geprojecteerd in de originele beelden om onderdelen met dezelfde fluorescentie eigenschappen zichtbaar te maken. Deze eenvoudige methode stelt ons in staat om snel beelden te segmenteren. Verschillende structuren zoals Stratum Corneum, epidermale cellen, melanine rijke cellen en de dermis kunnen eenvoudig onderscheiden worden door de fasor methode toe te passen.

In hoofdstuk 5 wordt de eigenlijke Lambda-Tau hardware beschreven. Het systeem is uitgerust met 7 spectrale kanalen en een variabel aantal temporele detectie kanalen met een vaste breedte van 200ps. Een fouten-analyse is uitgevoerd om zowel het spectrale als het levensduur detectie deel te karakteriseren. Met name is de invloed van het effect van de breedte van de spectrale en temporele detectie kanalen onderzocht. Ook is onderzocht hoe de detector zich gedraagt bij verschillende hoeveelheden gedetecteerde fotonen per seconde.

Spectraal opgeloste levensduur microscopie is veel meer dan een methode om simultaan levensduren en spectra te meten. De methode genereert 2 dimensionale datasets voor elk beeldpunt en de mogelijkheid om zowel levensduren bij verschillende emissiegolflengten te meten als emissiespectra in verschillende tijdskanalen. Door de gehele dataset tegelijk te analyseren kan in principe nieuwe informatie verkregen worden over het preparaat en de gevoeligheid van analyses verhoogd worden. Dit wordt in detail beschreven in hoofdstuk 6. Hier wordt de gecombineerde analyse van levensduur en spectrale informatie o.a. gebruikt om, zonder voorkennis, het signaal van 3 verschillende fluorophoren in een cel van elkaar te scheiden. Van elke fluorophore is de fractionele intensiteit, het spectrum en de verval curve bepaald op basis van Lamda-Tau dataset.

Fluorescentielevensduur microscopie wordt tegenwoordig routinematig gebruikt om moleculaire interacties af te beelden. Hier wordt gebruik gemaakt van twee typen fluorescente moleculen, donor en acceptor, met geschikte eigenschappen. Zodra deze moleculen binnen een afstand van 10nm van elkaar zitten kan Förster Resonance Energy Transfer (FRET) optreden. Dit resulteert in een verkorting van de fluorescentie levensduur van de donor die direct gerelateerd is aan de FRET efficiëntie. FRET resulteert ook in verhoogde emissie van de acceptor fluorescentie. Tot nu toe zijn er geen simultane FRET analyses gepubliceerd op basis van donor en acceptor signalen. In hoofdstuk 7 wordt een simultane FRET analyse uitgevoerd van alle spectrale levensduur kanalen met daarin de signalen van zowel de donor als de acceptor. Analyse van een goed gedefinieerd testpreparaat (gelabeld DNA) laat zien dat de juiste FRET efficiëntie bepaald kan worden in de aanwezigheid van een mengsel van geïsoleerde donor moleculen en donor-acceptor paren.

Acknowledgment

I have experienced so many exciting days between my birthday on November 26th of 2008, the day I joined the Molecular biophysics group, and the first day of the Persian calendar, the day of my thesis defense. During these years of intense work, many people around me contributed to my PhD project to get the Lambda-Tau up and running. I am concerned that I might forget someone in this acknowledgement. Therefore, I would like to express my thanks to all the people who have given their support and shared their knowledge.

Above all, my deep gratitude goes to Professor Hans Gerritsen, who expertly guided me through my research and shared excitement of four years of discovery. He showed me the road and he was very patient with my super ambitious ideas. Moreover, he helped me to draw a prospect of a multi-dimensional imaging world. He was more than a supervisor to me during these years and helped me in many though situations.

I would also like to thank Dr. Gerhard Blab for his invaluable support, reading the manuscripts and his thoughtful comments and advices. I appreciate his great help with making DNA samples, a process that was all Greek to me.

I am greatly indebted to Dave van den Heuvel; he was always there to listen to my problems and explained, in simple language, solutions to problems by employing my imagination. That's the way I always do it and for that reason I enjoyed being on the same wavelength with him.

I would also like to acknowledge Keimpe Reitsma, his support was invaluable for the lambda Tau part of my project. He was always available to help me immediately when I had problems with the complicated and delicate electronics hardware.

I want to also thank Dr. Kees van der Oord who helped me with the initial programming of the Lambda-Tau software.

I also thank Dr. Arjen Bader for helping me to bring the wild idea of spectral phasors into reality and introduce me to yet another dimension in microscopy, fluorescence anisotropy.

I would like to thank Dr. Alessandro Esposito; he initiated me into the basics of phasor analysis which appears in all chapters of my thesis. He helped me a lot with my first paper and I appreciate his constructive and stimulating comments.

I take this opportunity to thank Dr. Sasha Agronskaia for helping me to implement the Lambda-Tau detector into the Multi-photon setup; which became my favorite setup for the final experiments.

I am grateful to Dr. Jarno Voortman and Dr. Erik Hoffman for supplying me with the specimens used for my first paper.

I would like to thank my parents for their unconditional support, love and blessings. They were there when I needed them most.

Last but not least, I want to thank Atieh, she was always there to listen to my success and failure stories. Her understandings and encouragements have been a powerful source of inspiration and energy during the past few years.

CV

I was born on the 26th of November of 1979 in Urmia Iran. After finishing my High school I obtained my BSc degree in Physics at the Faculty of Natural Sciences, University of Urmia, in 2001. Next, I Joined the Laser and Plasma research Institute of Shahid Beheshti University and started a master in Photonics. My master project concerned the development of a diode pumped solid state Nd:YAG laser. After my graduation in 2004, with a final mark of 19.5/20 for my thesis defense, I moved into the imaging field and worked on 3D scanners using triangulation and structured illumination techniques. On November 2008 I started my PhD under supervision of Prof. Gerritsen in the Molecular Biophysics of Utrecht University. I worked on the development of novel detection hardware and analysis algorithms for spectrally resolved lifetime imaging in scanning microscopy.